**PERIODIC METHODS FOR CONTROLLING
A SATELLITE IN FORMATION**

THESIS

Erin Y. Carraher, Captain, USAF

AFIT/GA/ENY/02-1

**DEPARTMENT OF THE AIR FORCE
AIR UNIVERSITY**

AIR FORCE INSTITUTE OF TECHNOLOGY

Wright-Patterson Air Force Base, Ohio

Report Documentation Page

Report Date 26 Mar 02	Report Type Final	Dates Covered (from... to) Aug 2000 - Mar 2002

Title and Subtitle Periodic Methods for Controlling a Satellite in Formation	**Contract Number**
	Grant Number
	Program Element Number
Author(s) Capt Erin Y. Carraher, USAF	**Project Number**
	Task Number
	Work Unit Number
Performing Organization Name(s) and Address(es) Air Force Institute of Technology Graduate School of Engineering and Management (AFIT/EN) 2950 P Street, Bldg 640 WPAFB OH 45433-7765	**Performing Organization Report Number** AFIT/GA/ENY/02-1
Sponsoring/Monitoring Agency Name(s) and Address(es) Dr Andrew Sparks AFRL/VACA 2130 8th Street WPAFB OH 45433	**Sponsor/Monitor's Acronym(s)**
	Sponsor/Monitor's Report Number(s)

Distribution/Availability Statement
Approved for public release, distribution unlimited

Supplementary Notes
The original document contains color images.

Abstract
Precise position determination and control is necessary to accomplish proposed satellite formation flying missions of ground movement target indication and synthetic aperture radar. This thesis combines the estimation and control techniques of past AFIT theses with various time-varying and time-invariant LQG control methods. Linear time-invariant control is ideal for on-board satellite estimation and control applications, freeing-up the satellites limited computational capacity. Using a dynamics frame transformation from the nodal frame to an orbital frame, a higher fidelity, time-periodic model produced nearly identical results for either time-varying or time-invariant control for many scenarios. Scenarios included initial perturbations in the radial, in-track, and cross-track directions as well as increased magnitude perturbations; step size increase from 0.2 seconds to 2 seconds; and increased and reduced measurement noise level scenarios versus the standard absolute GPS receiver noise level. Results obtained indicate the ability to control within the error range of the measurements (centimeter-level and better) using realistic noise and dynamics perturbations

Subject Terms	
Subject Terms Satellite Clusters, Estimation, LQR, Time Periodic, LTI, Satellite Formation Flying	
Report Classification unclassified	**Classification of this page** unclassified
Classification of Abstract unclassified	**Limitation of Abstract** UU
Number of Pages 133	

AFIT/GA/ENY/02-1

PERIODIC METHODS FOR CONTROLLING A SATELLITE IN FORMATION

THESIS

Presented to the Faculty

Department of Aeronautics and Astronautics

Graduate School of Engineering and Management

Air Force Institute of Technology

Air University

Air Education and Training Command

In Partial Fulfillment of the Requirements for the

Degree of Master of Science in Astronautical Engineering

Erin Y. Carraher, B.A.E.

Captain, USAF

March 2002

AFIT/GA/ENY/02-1

PERIODIC METHODS FOR CONTROLLING A SATELLITE IN FORMATION

Erin Y. Carraher, B.A.E.
Captain, USAF

Approved:

_____// signed //_____   _____
David R. Jacques (Chairman)   date

_____// signed //_____   _____
William E. Wiesel (Member)   date

_____// signed //_____   _____
Richard G. Cobb (Member)   date

Acknowledgments

> When my spirit was overwhelmed within me,
> Then You knew my path.
> In the way in which I walk ...
> Psalms 142:3 (NKJV)

Overall, I must thank the Lord for keeping me on the path during this trying and difficult ordeal. Only He would help me through the darkest parts of this thesis process.

My never-ending love and thanks go to my wife. I knew this would be a stormy long-fought journey, but she was my rock of support and made all the sacrifices bearable.

I would like to express appreciation to my advisor and reader for the help and advice they gave me. Lt. Col. Jacques loaned me so many resources: class notes, textbooks, and a top-of-the-line PC. It was only a matter of time that I could eventually get everything figured out, so I could actually start my work.

I would also like to thank all the space folks: Ayhan, Borg, Dave, Fatih, Hakan, Mike, and Tom. We suffered through a lot together. It wasn't easy, but now it is done.

Erin Y. Carraher

Table of Contents

List of Figures

List of Tables

AFIT/GA/ENY/02-1

Abstract

Precise position determination and control is necessary to accomplish proposed satellite formation flying missions of ground movement target indication and synthetic aperture radar. This thesis combines the estimation and control techniques of past AFIT theses with various time-varying and time-invariant LQG control methods. Linear time-invariant control is ideal for on-board satellite estimation and control applications, freeing-up the satellite's limited computational capacity. Using a dynamics frame transformation from the nodal frame to an orbital frame, a higher fidelity, time-periodic model produced nearly identical results for either time-varying or time-invariant control for many scenarios. Scenarios included initial perturbations in the radial, in-track, and cross-track directions as well as increased magnitude perturbations; step size increase from 0.2 seconds to 2 seconds; and increased and reduced measurement noise level scenarios versus the standard absolute GPS receiver noise level. Results obtained indicate the ability to control within the error range of the measurements (centimeter-level and better) using realistic noise and dynamics perturbations.

PERIODIC METHODS FOR CONTROLLING A SATELLITE IN FORMATION

I. Introduction

1.1 Background

In tackling this subject, two questions come to the forefront. Why focus on time periodic methods and why satellite formations?

Periodic characteristics are observed both naturally and artificially in many mechanisms, most notably in satellite orbits and orbit perturbations. Since orbital control usage is a big driver in the lifetime of all satellites, only using control when necessary should be the goal of the control system. If perturbations are periodic and small enough that they can be ignored, there is no reason to spend fuel to control them. The periodic nature of the perturbation will correct itself. The detail of how small the perturbation can be before it warrants correction must be defined and justified via simulations before it can be used for actual flight tests.

The importance of modeling the periodic characteristics is multiplied as future space missions will use several small satellites flying in formation to serve many of the same purposes as a single large satellite.
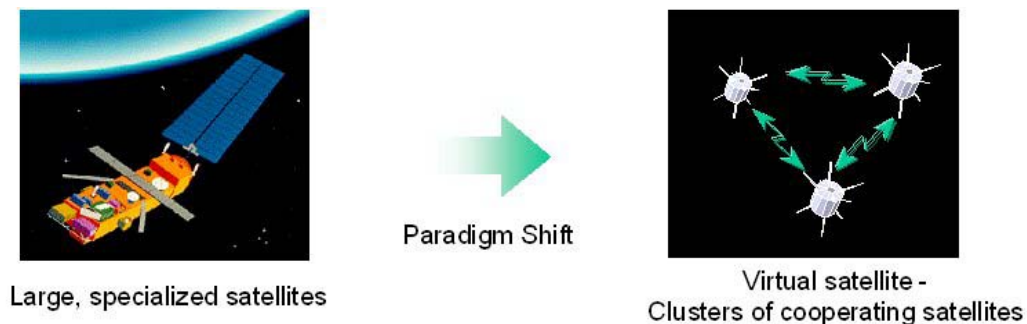
Figure 1. Paradigm Shift [1]

This paradigm shift will produce many rewards: lower overall mission cost, increased system reliability, improved science return, extended mission life, and expandability. Satellite formation has been a widely studied area for nearly a decade, with a patent for the concept granted in 1983 [24]. Many space agencies currently have actual or proposed satellite formations on their drawing boards or operating in space.

The European Space Agency's Cluster II project, launched in 2000, uses four satellites in tetrahedral formation to study electrical and magnetic phenomena inside the magnetosphere and in the solar wind upstream of the Earth.

ESA's Cluster II Satellites [10]	NASA's StarLight Satellites [20]
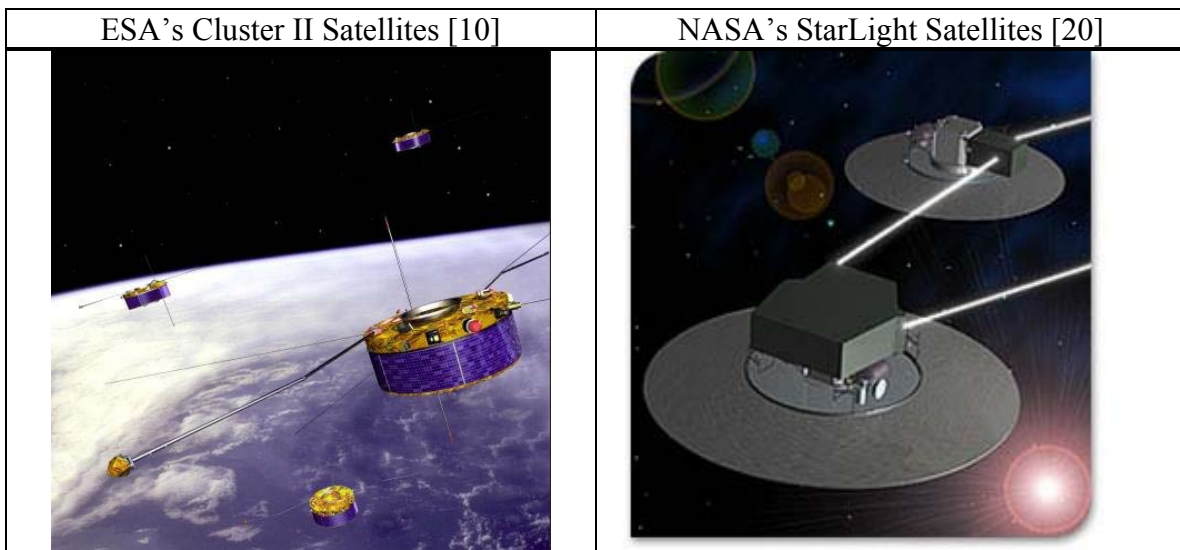
Figure 2. ESA's Cluster II and NASA's StarLight Satellites

NASA's StarLight mission, consisting of two satellites in formation to be launched in 2005, will be the first spaceborne stellar interferometer. By flying in formation, Starlight's two small telescopes will achieve the angular resolution (in one direction) of a regular telescope mirror 125 meters in diameter.

The United States Air Force (USAF) has focused its efforts on the Technology Satellite of the 21st Century (TechSat 21). The Air Force Research Laboratory (AFRL) leads the project.

Subsystem	Mass, kg
Radar Payload	24.0
ADACS	3.8
Propulsion	7.8
TT&C	4.0
C&DH	2.4
Structure	10.7
Power	25.0
Thermal	2.5
Propellant	2.5
Mass w/o contingency	82.7
Contingency	16.1
Total	98.8
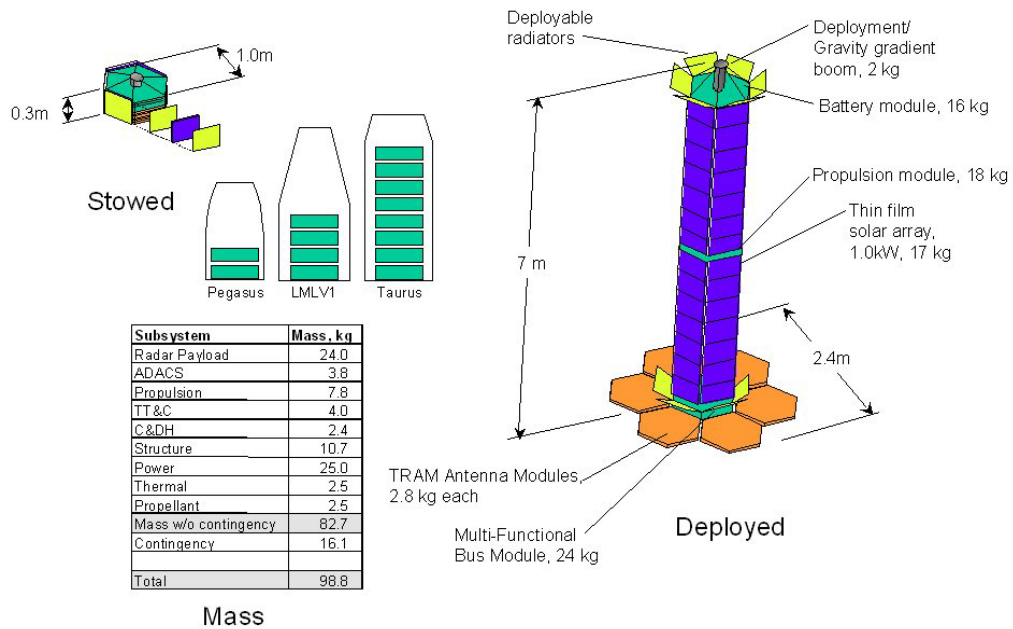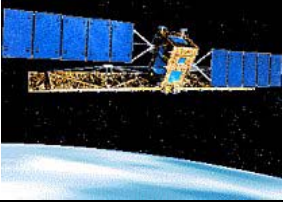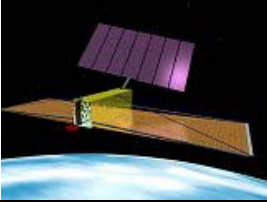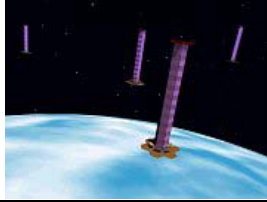
Figure 3. AFRL's TechSat 21 Satellite [1]

As AFRL's website explains, the initial focus of TechSat 21 is a space-based radar mission for Ground Moving Target Indication (GMTI) employing a formation of eight micro-satellites [1]. This program hopes to achieve three times the capability of current assets at one-third their cost.

Table 1. AFRL's TechSat 21 Cost Savings [1]

	Conventional	Evolutionary	Revolutionary
	Rigid Panel Deployable	Integrated Antenna	Distributed Spacecraft
Satellite Mass	12,000 kg	4,400 kg	Eight 100 kg satellites per cluster
Age of Technology	1996 Technology	2003 Technology	2005 Technology
Number of Satellites Required	40 satellites	40 satellites	40 satellite clusters
Launch Vehicle	Titan IV	Atlas II	Taurus/Athena II
Launch Cost	$300M	$90M	$25M
Total System Cost (10 year life cycle, normalized)	1.0	0.6	0.3

The reduced life cycle cost will be achieved by reduced launch costs and overall manufacturing cost through mass-produced identical micro-satellites. The TechSat 21 program manager even speculates the possibility that TechSat 21 satellites could be launched from operational military jets such as the F-15 [23].

The GMTI mission of detecting ground targets in a military theater for the USAF is currently being accomplished by Joint Surveillance and Targeting Attack Radar System (JSTARS) aircraft. The proposed Techsat 21 system could move this GMTI mission from an airborne platform to space. Better performance will come from extremely large effective aperture sizes and multi-mission capability. For radars, large apertures improve performance with better slow target detection and better resolution. In fact if the range to the target, R, and the radar's wavelength, λ, are assumed constant, the resolution of an object on the ground, r, is inversely proportional to S, the synthetic aperture size [16].

$$r = \frac{R \cdot \lambda}{2 \cdot S} \qquad (1)$$

4

The key to the concept is the close formation of microsatellites, each with a receiver that detects both the return from its own transmitter and the bistatic responses from the orthogonal transmit signals of the other satellites in its cluster. Pulses are separated, and range, angle of arrival, and Doppler processing is computed. The collaborating small apertures of TechSat 21 can act as one large array which can be reconfigured to satisfy and optimize requirements for a variety of missions.
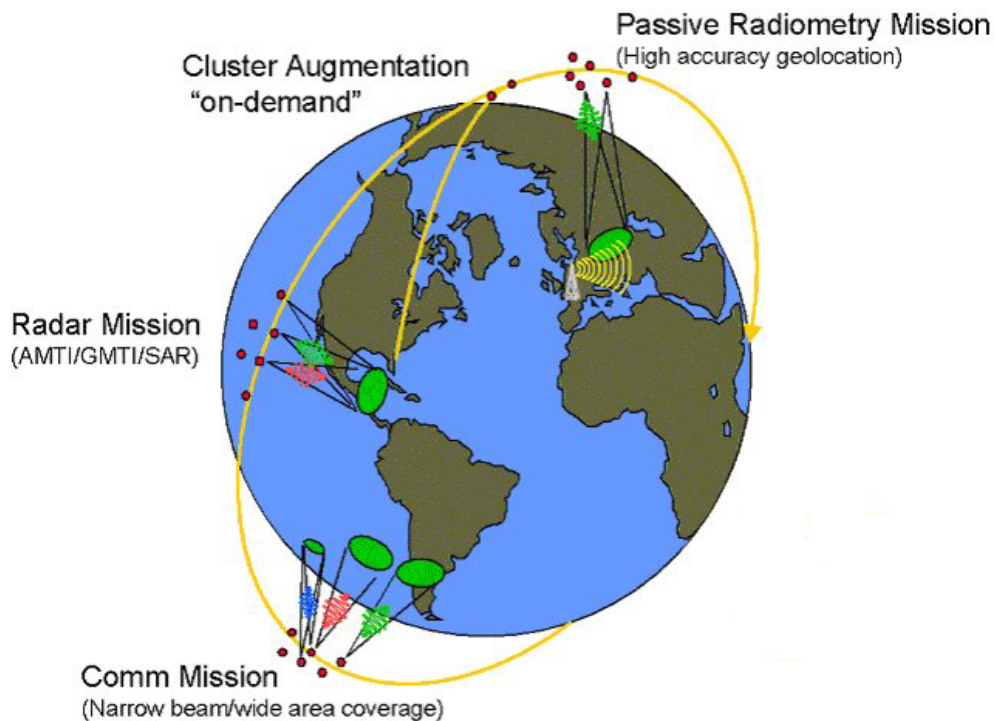
Figure 4. AFRL's TechSat 21 Missions [1]

Possible autonomous capability would allow the satellite cluster, working in conjunction with the Global Positioning System, to automatically reshape its formation to optimize its geometry based on the mission assigned to the cluster by the ground commander. For example, a "geo-location" mission such as finding a downed pilot would require that one satellite in the cluster move out from the group to a distance of

approximately eight kilometers. Or for spotting moving ground targets, closer intervals on the order of several hundred meters would be required [23].

Improved reliability will be achieved with graceful degradation of capability and reconfigurability to minimize the effects of a single failure. The satellite clusters also allow an inherent adaptability easing performance upgrades by allowing an upgraded satellite to join a cluster vice replacing another satellite. Much like a network of desktop computers linked together, they can be expanded as needed without throwing out the entire system.

"The availability of such low cost, highly capable microsatellites will lead to new ways of doing business in space, and this 'personal satellite' paradigm can revolutionize the space industry in much the same way as the personal computer has done to the computer industry," said Dr. Alok Das, chief technologist for AFRL's Space Vehicles Directorate [12].

1.2 Past Research - Standing on the Shoulders of Giants

1.2.1 Satellite Cluster Research at AFIT from 1988 - 1991. A number of AFIT theses in the past have utilized Kalman filter techniques to study relative position errors within a satellite cluster [19, 24]. The dynamics were based on Clohessy-Wiltshire equations with near circular orbits. Ward used a point mass orbit in his truth model, but Middendorf included a more realistic truth model. He included perturbations in the J2 term of the Earth's geopotential. For relative positioning they both used a U-D covariance factorization version of the Kalman filter comparing range data between satellites synchronized with clock pulses. They achieved a relative position error of 3 cm. This relative centimeter-level accuracy was achieved without the use of Global Positioning System (GPS) satellite positioning data.

1.2.2 Satellite Cluster Research at AFIT from 2000 - 2001. More recent AFIT theses incorporated GPS positioning data into a Bayes filter. Davis attempted to extend from relative position determination of the past to include absolute position determination, but he encountered numerical difficulties due to the extreme accuracy requirements of his filter [9]. The double precision computational capability was not able to accurately generate covariance inversions for his filter. Bordner revisited the previous theses and focused mainly on relative positioning [4]. Following a new approach by Wiesel [28], Bordner updated the dynamics model by solving the time periodic, linearized system using Floquet Theory. More accurate than the Clohessy-Wiltshire solutions used in previous theses, this dynamics model included all zonal harmonics of the Earth to include sectoral, tesseral, and air drag perturbations. Bordner's dynamics truth model was also used in this current thesis as discussed in Chapter III. Bordner additionally expanded on the method of relative data collection from previous theses. He compared results using the relative range information from satellite timing signals, as was the basis for the AFIT theses from a decade ago, with both absolute GPS data and Carrier Phase Differential GPS data. Using Differential GPS data, Bordner achieved a relative position error of 2 cm.

Another AFIT thesis authored by Irvin studied several linear and nonlinear feedback control methods for satellite formation reconfigurations [9]. One of his more successful methods, the state dependent Riccati equation, was used as a starting point for the regulator in the second phase of this thesis. This current thesis diverged from Irvin's work by using the assumed superior dynamics model as used by Bordner in place of Irvin's Clohessy-Wiltshire method. The combined filter and regulator for this thesis should provide a good combination building on Bordner's estimation work and Irvin's control method.

1.3 Objectives

In order for the TechSat 21 project to work and be cost effective, AFRL lists a number of fundamental questions that must be answered [1]. The focus of this thesis is to answer "what orbits or orbital control techniques are possible to maintain the desired configuration?"

This thesis will look at two different periodic frames of reference for the dynamics of the system, the nodal frame and the orbital frame. In each of these frames, time-varying and time-invariant control techniques will be compared. Variations on the system model will include scenarios with: initial deflections in each direction, increased magnitude of initial deflection, reduced step size, decreased measurement noise, and increased measurement noise. Some of these scenarios may improve performance of the system, but taken as a whole, all scenarios will test the fidelity of each model for many environments.

The ideal result of this thesis would be to create a robust output feedback compensator that handles a wide variety of realistic perturbation scenarios minimizing both fuel usage and Root Mean Squared (RMS) error. The stringent space-based radar application would require position accuracy to one tenth of the radar's wavelength [8], thus requiring millimeter-level accuracy. While past theses have shown that positions can be estimated to the centimeter level, we would also like to be able to control our satellite to the centimeter level or better. This may not be an easy task given the preliminary assumed conditions of estimation using absolute GPS position data constrained with over one meter uncertainty.

II. Dynamics Theory and Methodology

2.1 Satellite Relative Motion

As mentioned in the previous chapter, this current thesis used the same method as Bordner for calculating the dynamics for the truth model [4]. Relative satellite motion has often been studied and applied using satellite rendezvous dynamics models based on Clohessy-Wiltshire (CW) equations with near circular orbits. Clohessy and Wiltshire followed on from the work of Hill from the 1800's. They reduced the dynamics of satellite relative motion into a two-body problem. They assumed a circular orbit, linearized the system of equations, and produced a solution. Although this solution was originally intended to describe the relative motion of a closing satellite docking with a target satellite or space station, CW equations are usually chosen as the place to start for satellite formation analysis.

2.1.1 Clohessy-Wiltshire.

While the CW method was not used for this thesis, it was useful to look at its setup and compare it with the method employed by Bordner in his thesis [4]. The CW equations in their simplest form did not model any perturbations in their solution to the linearized circular orbit. For our earth-orbiting satellites, the CW equations are expressed in differential form

$$\ddot{x} - 2 \cdot n \cdot \dot{y} - 3 \cdot n^2 \cdot x = 0$$

$$\ddot{y} + 2 \cdot n \cdot \dot{x} = 0 \tag{2}$$

$$z + n^2 \cdot z = 0$$

where n is the mean motion

$$n = \sqrt{\frac{\mu_e}{R_{sat}^3}} \qquad\qquad (3)$$

where μ_e=3.986E14 m^3/s^2 is the earth gravitation parameter and R_{sat} is the radius from the center of the earth to the satellite in orbit. The standard Clohessy-Wiltshire reference frame employs x, y, and z corresponding to radial, in track, and orbit normal. For the "free motion" CW model, Equations 2 were all set equal to zero. More advanced CW models would include perturbations added on the right hand sides of these equations.
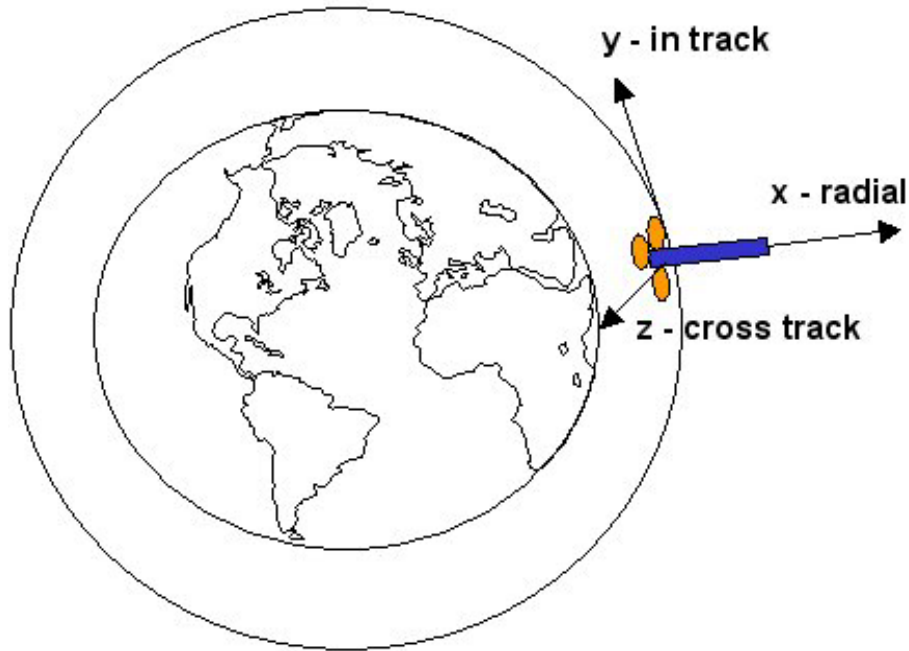
Figure 5. Clohessy-Wiltshire Reference Frame

Following a free motion CW model, satellites would be constrained to an ellipse of 2 to 1 dimensionality along the trajectory of the orbit of the satellite and in the vertical plane of motion [21]. The actual dynamics of the system would be periodic, and even though the relative distances between satellites would remain variable, the overall size of the cluster would be bounded. Sedwick further described the destruction of the free motion CW model due to the overwhelming nature of the real world secular and periodic

perturbations. The goal for satellite formation modeling would be to include all forces that cause the orbital position to diverge. Benign perturbing forces driving satellites to move periodically or in unison could remain un-modeled.

But even adding significant perturbation estimates to the CW equations would not be expected to supply the best estimates for satellite formation navigation [4]. Hill's equations were based on a time-invariant system, which limits the credibility of the dynamics for its application for periodic systems such as satellite formations. The CW equations were designed for satellite rendezvous, not satellite formations. A new relative satellite dynamics model was needed to adequately cover the nature of the satellite formations.

2.1.2 Wiesel. As mentioned above, this current thesis used the same method as Bordner for calculating the dynamics for the truth model [4]. This method was a result of work accomplished by Dr. William Wiesel in the area of relative satellite motion developed to meet the severe relative positioning accuracy requirements inherent in space-based radar applications [27, 28]. His method, similar to the classic Clohessy-Wiltshire solution for relative satellite motion, took a new approach by linearizing about a nearly circular periodic orbit as a reference solution. The reason for integrating a periodic orbit versus some other particular orbit was that the orbital behavior was better understood as time drove towards infinity [26]. This was because in the inertial frame the orbit behavior, given the same initial conditions and perturbations, would repeat every period plus an orbital regression along the equator. To work with an orbit that closed on itself exactly, the nodal frame was introduced. This allowed a resulting linear, time periodic system instead of a linear, time invariant system.

Wiesel's process followed a Hamiltonian method [4, 28]. A Hamiltonian function was used to describe the orbital motion of a small body traveling around the earth. With

dimensionless units, setting the radius of earth $R_e = 1$, gravitational constant $G = 1$, and the mass of earth $M_e = 1$, the inertial frame Hamiltonian function became

$$H = \frac{1}{2} \cdot \left(P_x^2 + P_y^2 + P_z^2 \right) - \frac{1}{r} + \frac{J_2}{2 \cdot r^3} \cdot \left(\frac{3 \cdot Z^2}{r^2} - 1 \right) + \frac{J_3}{2 \cdot r^4} \cdot \left(\frac{5 \cdot Z^3}{r^3} - \frac{3 \cdot Z}{r} \right) + \cdots \quad (4)$$

The inertial state vector was defined as $I_T = (X,Y,Z,P_x,P_y,P_z)$, and the radius r was defined as $r = \sqrt{X^2 + Y^2 + Z^2}$. The P_i momenta states were defined as inertial velocity components because the Hamiltonian is in terms of mass per unit satellite. An advantage of using the Hamiltonian method was the convenience of adding perturbations. Additional conservative perturbations could be modeled by including the potential function of the perturbing force. Non-potential forces such as air drag were expanded about the periodic orbit, and then added to the Hamiltonian equations of motion for the momenta states.

In the inertial frame, the actual orbit would regress along the equator and not return to the same position after one period [28]. Because of this regression, the system was transformed to a nodal frame where the orbit would actually close on itself thus becoming periodic. The resulting Hamiltonian became

$$H' = \frac{1}{2} \cdot \left(P_x'^2 + P_y'^2 + P_z'^2 \right) + \dot{\Omega} \cdot \left(P_x' \cdot Y' - P_y' \cdot X' \right) + V\left(Z', r \right) \quad (5)$$

where the prime superscript symbol ` denoted the state vector components transformed into the nodal frame, N. The component $V\left(Z', r \right)$ included the conservative zonal harmonics terms transformed into the nodal frame. The nodal frame state vector was defined $N^T = (X', Y', Z', P_x', P_y', P_z')$. The beauty of this approach was that the nodal frame was not the only frame in which the system was periodic. The nodal system could be moved back to the classic CW frame (Figure 5) and still keep its periodic quality. To accomplish this, the periodic orbit was initially transformed to the origin of the current

coordinates. The periodic orbit was subtracted off from the nodal state vector, giving new coordinates

$$x = X' - X'_o$$

$$y = Y' - Y'_o$$

$$z = Z' - Z'_o$$

$$(6)$$

$$p_x = P'_{xo}(t)$$

$$p_y = P'_{yo}(t)$$

$$p_z = P'_{zo}(t)$$

where the subscript "o" denoted the periodic orbit. This transformation produced the Hamiltonian with its second order and above terms evaluated on the periodic orbit. Using the new coordinate vector $L^T = (x,y,z,p_x,p_y,p_z)$ defined by Equation 6, the Hamiltonian now became

$$H'' = \frac{1}{2!} \cdot \left(H''_{\alpha\beta} \cdot L_\alpha \cdot L_\beta \right) + \frac{1}{3!} \cdot \left(H''_{\alpha\beta\gamma} \cdot L_\alpha \cdot L_\beta \cdot L_\gamma \right) + \cdots \qquad (7)$$

The $H''_{\alpha\beta}$ and $H''_{\alpha\beta\gamma}$ components were fully symmetric partial derivative tensors computed for the periodic orbit defined as

$$H''_{\alpha\beta} = \left. \frac{\partial^2 H'}{\partial N_\alpha \partial N_\beta} \right|_o$$

$$(8)$$

$$H''_{\alpha\beta\gamma} = \left. \frac{\partial^3 H'}{\partial N_\alpha \partial N_\beta \partial N_\gamma} \right|_o$$

where repeated Greek indices were a summation from one to six.

A final transformation rotated the solution into the classic CW frame (radial, in-track, and cross-track). To generate a linear system, the Hamiltonian K was truncated to include only terms following the second order

$$K_2 = \frac{1}{2} \cdot \left(H''_{\alpha\beta} \cdot R^{(2)}_{\alpha\beta} \cdot R^{(2)}_{\beta\gamma} \right) + p \cdot \left(\dot{R} \cdot R^T \right) \cdot q \qquad (9)$$

where $H''_{\alpha\beta}$ was defined above in Equation 8, $R^{(2)}_{\alpha\beta}$ and $R^{(2)}_{\beta\gamma}$ were 6 by 6 dimensioned block diagonal matrices with two copies of the nodal to orbital frame rotation matrix R on the diagonal, the Z components were the canonical state vectors in the orbital frame, and the p and q components were 3 by 1 vectors holding the momenta and coordinates from the local frame state vector L [28]. The canonical equations of motion would then be calculated by using Hamilton's Equations

$$\dot{q}_i = \frac{\partial K_2}{\partial p_i}$$

$$\dot{p}_i = \frac{\partial K_2}{\partial q_i} \qquad (10)$$

to evaluate the Hamiltonian function in Equation 4.

2.1.3 Floquet Theory. The equations of motion calculated in the previous section can be integrated for one period to obtain the desired periodic orbit [4, 28]. Linearized equations are created by expanding about this periodic orbit. The periodic nature of these equations made the approach to solve them a bit more complicated than the simple CW solution. The solution was based on Floquet theory that linearizing about a periodic orbit resulted in a periodic coefficient linear system. The time periodic linear differential equations were of the form

$$\partial \dot{x} = A(t) \cdot \partial x \qquad (11)$$

Floquet found that the solution to Equation 11 was the state transition matrix

$$\Phi(t,0) = F(t) \cdot e^{Jt} \cdot F^{-1}(0) \tag{12}$$

where F(t) is a periodic matrix, and J is a matrix of system frequencies in the Jordon normal form. The J matrix is typically diagonal with Poincaré exponents as elements of the diagonal. This Floquet state transition matrix from Equation 12 is similar to the constant coefficient form, but it is unique in its periodic nature. To find the solution for $\Phi(t,0)$, both J and the periodic matrix F(t) needed to be calculated. Equation 11 was integrated for one period to calculate the mondromy matrix. For a periodic F(t), $F(t + \tau) = F(t)$. So plugging in $t = \tau$, Equation 12 became

$$\Phi(\tau,0) = F(\tau) \cdot e^{J\tau} \cdot F^{-1}(0) \tag{13}$$

after rearranging terms, F(0) was recognized as the eigenvector matrix for $\Phi(\tau,0)$

$$F(0) \cdot \Phi(\tau,0) \cdot F^{-1}(0) = e^{J\tau} \tag{14}$$

The eigenvalues of $\Phi(\tau,0)$, were calculated at F(0) using the relation

$$\lambda_i = e^{\omega_i} \cdot \tau \tag{15}$$

where ω_i were the Poincare exponents of the J matrix. Rearranging this equation to solve for ω_i would eventually lead to the solution for J.

$$\omega_i = \frac{1}{\tau} \ln \lambda_i \tag{16}$$

Substituting Equation 12 into Equation 11

$$\dot{F} = A(t) \cdot F(t) - F(t) \cdot J \tag{17}$$

Integration of Equation 17 for one period provided a solution for $\Phi(t,0)$. The end result was an inertial position vector for the satellite

$$I(t) = R_Z^{(2)} \cdot \left(N_o(t) + (R^{(2)})^T \cdot F(t) \cdot e^{Jt} \cdot F^{-1}(t_o) \cdot Z(t_o) \right) \tag{18}$$

and the satellite's position relative to the periodic orbit in the orbital frame was

$$Z(t) = F(t) \cdot e^{Jt} \cdot F^{-1}(t_o) \cdot Z(t_o) \tag{19}$$

15

2.1.4 Wiesel vs. Clohessy-Wiltshire. Wiesel's dynamics model approach attempted to better predict satellite behavior and minimize the fuel required to control the satellite by modeling all major perturbations. As Bordner showed in his thesis, this method improved on the Clohessy-Wiltshire approach in three areas [4]. First, Wiesel's method inherently retained more satellite behavior information over time, thus it introduced less error into the dynamics model. Second, two secular modes (rather than the usual one secular mode) were modeled by the dynamics. These secular modes would be better compensated for without using extraneous fuel to try to negate them. Third, Wiesel included a better representation of the earth's zonal harmonics (zonal effects were modeled to the 14th order in this thesis), air drag, and gravitational harmonics. Better modeling of perturbations produced a more realistic model to build upon. This solution improved on the Clohessy-Wiltshire solution by three orders of magnitude [28].

2.2 Actual Thesis Dynamics Setup

The first step in setting up the estimator/controller was to define where you are. As mentioned earlier in this chapter, the standard Clohessy-Wiltshire reference frame was used with x, y, and z corresponding to radial, in track, and orbit normal as is shown in Figure 5. This earth-centered inertial reference frame was defined in terms of distance units (DU), with one DU approximately equal to the equatorial radius of the earth, 6378.145 km, and time units (TU), with one TU approximately equal to 13.447 minutes [2]. Based roughly on Techsat 21 planned characteristics, the orbit height was set at 0.1 DU (637.8 km) with a 7.244 TU (97 minute) period for a near circular orbit. An existing program was used to generate the initial velocities corresponding to the chosen orbit. The initial state was defined as a vector of positions and velocities:

$$\dot{X} = \begin{bmatrix} x \\ y \\ z \\ \dot{x} \\ \dot{y} \\ \dot{z} \end{bmatrix} = \begin{bmatrix} 1.1(DU) \\ 0.0(DU) \\ 0.0(DU) \\ -0.0012936533(DU/TU) \\ 0.5153407938(DU/TU) \\ 0.8025957331(DU/TU) \end{bmatrix} \qquad (20)$$

2.2.1 Orbit Propagation. Following the method Bordner used for his thesis, the state was propagated from initial conditions through one orbit using a program written in the fortran computer language. The source code is primarily written by Dr Weisel with some additions to meet the specific requirements of this thesis. The main program, Po.f90, uses two main subroutines, haming and rhs. Subroutine haming is an ordinary differential equations integrator using a fourth order predictor-corrector algorithm. Haming collects the last four values for the state vector and extrapolates them to predict the next value. It then corrects the extrapolated prediction to find a new value for the state vector. Subroutine rhs calculates the equations of motion calling on the EGM96 earth gravity model and geopoten subroutines to add to the system a more accurate model for the zonal harmonics as well as air drag and gravitational harmonics.

It is worth noting that an intrinsic part of this thesis is the periodic nature of the orbit. Once the state vector is propagated over one orbit, the state vector (and its associated A matrix) will repeat exactly over following orbits. The word "exactly" is used in a perfect-world sense. The perturbing effects that cause the dynamics not to repeat "exactly" will be modeled as either dynamics noise (w) or measurement noise (v) to the system. For this thesis, the orbit closed on itself (initial state equals final state)

17

with errors on the order of 1E-11 DU and DU/TU. This error was comparable to about

1E-5 meters and 1E-8 meters/second.

2.3 Frame Variations for the A matrix

Along with the state vector propagated over the orbit, the fortran program also

propagated the A matrix associated with the state vector. This A matrix was derived as

the time periodic solution to the uncontrolled dynamics problem

$$\dot{X}(t) = A(t) \cdot X(t) \tag{21}$$

The original method of computing the A matrix was in the nodal frame as

described in a previous section. Within an orbital period, elements of this A matrix

would vary up to an order of magnitude 1E1. Using a transformation supplied by Dr.

Wiesle, the A matrix was rotated from the nodal frame (nearly an inertial frame) into the

orbital frame (similar to the CW frame). The benefit of this transformation was that

many of the elements of the A matrix were reduced in magnitude resulting in a maximum

order of magnitude variation of 1E-3 over the period. This smaller variation arose

speculation that the time varying A matrix could be treated as a constant A matrix.

2.3.1 Nodal Frame A Matrix. The original dynamics method in the nodal frame

produced an A matrix with element variations on the order of 1E1 within an orbital

period. Explicit element variations can be seen in Figure 6 below.
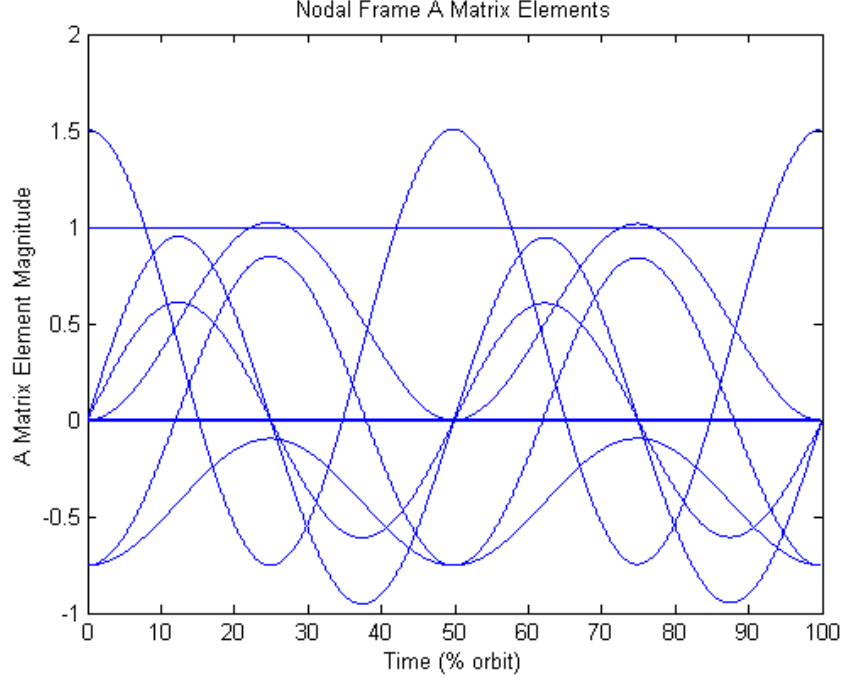
Figure 6. Variations of Each A Matrix Element Over One Orbit

Most notable from Figure 6 is that, while a majority of the elements are explicitly equal to zero, many of the non-zero elements vary periodically with different amplitudes and frequency of oscillation. For the most extreme case, the maximum amplitude difference exceeded one. While it is obvious that this A matrix would not be a good candidate for a linear time invariant (LTI) system, this assumption was used for the nodal frame, time-invariant (AnTI) model. The time-invariant A matrix used for this model was taken as a snap shot early on in the orbit before many of the varying elements had the opportunity to change

$$
A = \begin{pmatrix}
0 & -6.29E-4 & 0 & 1 & 0 & 0 \\
6.29E-4 & 0 & 0 & 0 & 1 & 0 \\
0 & 0 & 0 & 0 & 0 & 1 \\
1.506682 & 9.213E-4 & 1.446E-3 & 0 & -6.29E-4 & 0 \\
9.213E-4 & -0.75233 & 5.897E-7 & 6.29E-4 & 0 & 0 \\
1.446E-3 & 5.897E-7 & -0.75233 & 0 & 0 & 0
\end{pmatrix}
\tag{22}
$$

19

2.3.2 Orbital Frame A Matrix. In an effort to achieve linear time invariance, the original dynamics method was transformed to the orbital frame. This transformation provided by Dr. Wiesel produced an A matrix with element variations on the order of 1E-3 within an orbital period. Explicit element variations can be seen in Figure 7 below.
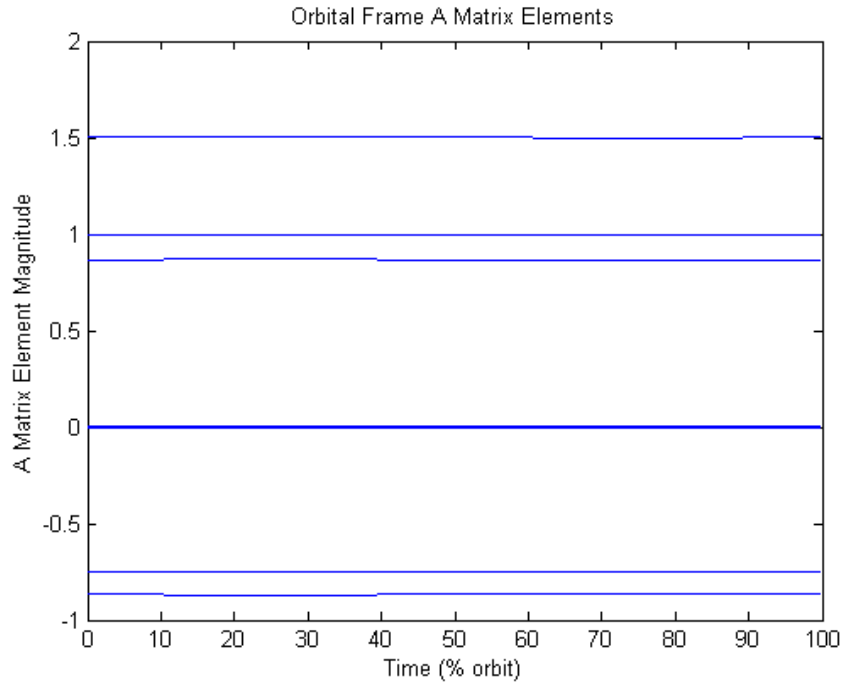
Figure 7. Variations of Each A Matrix Element Over One Orbit

In comparison with Figure 6, it is clear that this method, while still producing some periodically-varying non-zero elements with different amplitudes and frequency of oscillation, the amplitudes are much, much smaller than for the nodal frame. For the most extreme case, the maximum amplitude difference exceeded 1E-3 (see Figure 9 below). This A matrix appears be a good candidate for a LTI system, so this assumption was used for the orbital frame A matrix time-invariant (AoTI) model. The time-invariant

A matrix used for this model was also taken as a snap shot early on in the orbit before the varying elements had the opportunity to change

$$A = \begin{pmatrix} 0 & 0.867 & 0 & 1 & 0 & 0 \\ -0.867 & -1.4E-7 & -1.94E-6 & 0 & 1 & 0 \\ 0 & 1.94E-6 & -1.42E-7 & 0 & 0 & 1 \\ 1.5067 & 9.87E-6 & 6.34E-6 & 0 & 0.867 & 0 \\ 9.87E-6 & -0.7538 & -9.22E-4 & -0.867 & -1.42E-7 & -1.94E-6 \\ 6.33E-6 & -9.2E-4 & -0.7529 & 0 & 1.94E-6 & -1.42E-7 \end{pmatrix} \quad (23)$$

As will be shown in the results chapters, the assumption of LTI for this model worked very well over many scenarios.

2.3.3 Nodal and Orbital Frame Comparisons. It is also useful to look at comparisons of different elements of each A matrix.
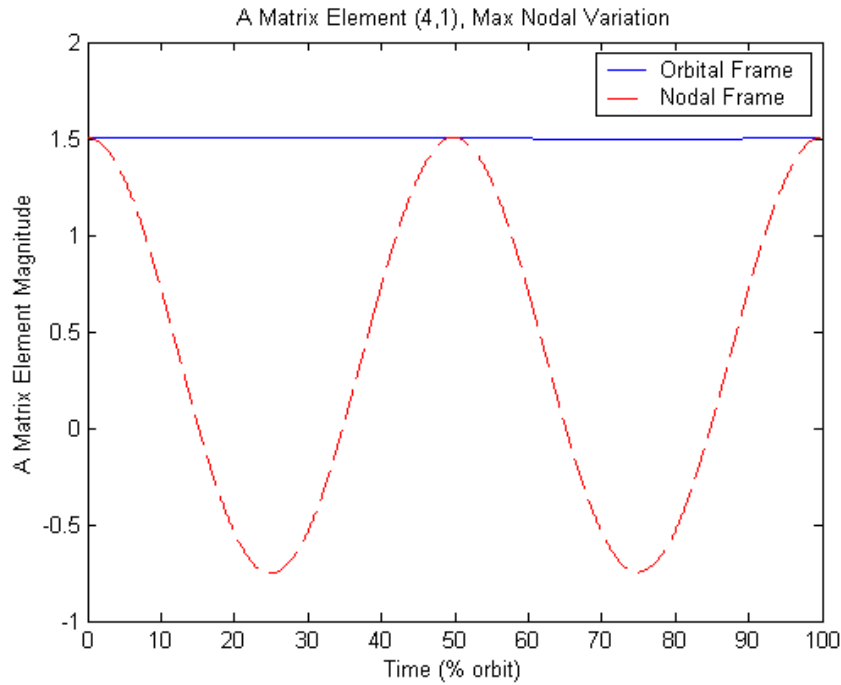
Figure 8. A Matrix Element (4,1) Comparisons, Max Nodal Variation
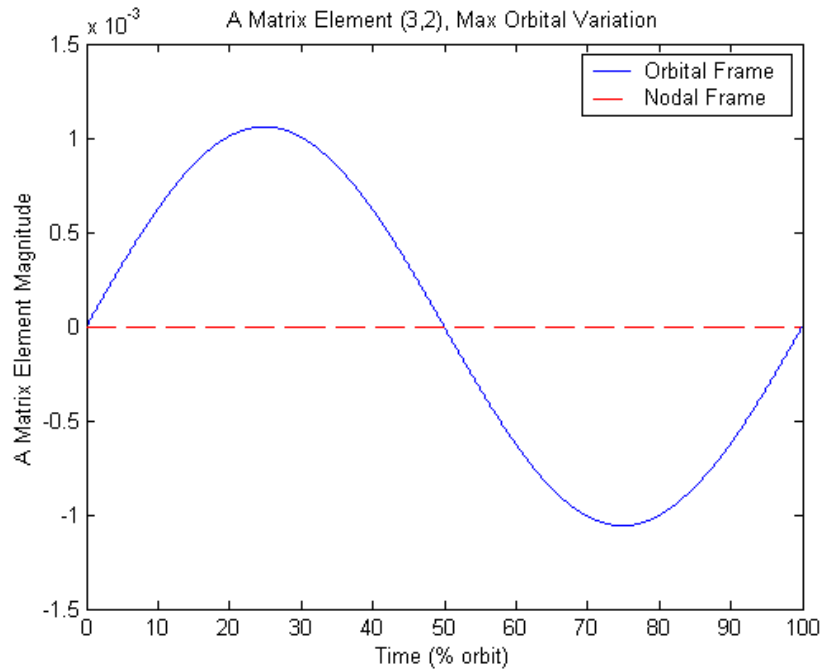
Figure 9. A Matrix Element (3,2) Comparisons, Max Orbital Variation
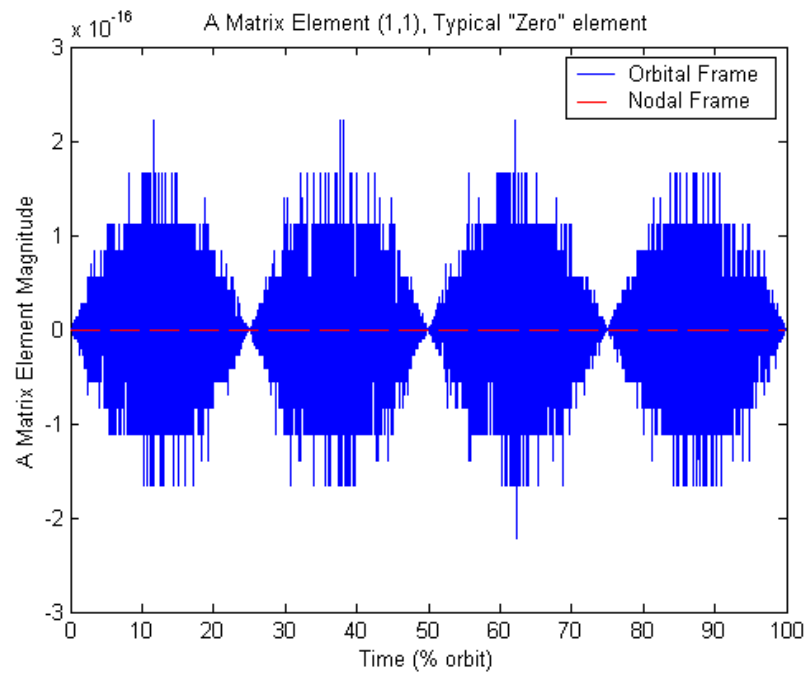
Figure 10. A Matrix Element (1,1) Comparisons, Typical "Zero" Element

Many of the zeros for the orbital frame actually varied periodically but were tiny.

III. Estimation and Control Methodology

The overriding tasks in estimation and control are obtaining a good estimate for the dynamic states and balancing the desire for state error cancellation (based on the state estimates) with the desire to keep fuel expenditure very low. We will use optimal control methods, specifically Kalman filter and linear quadratic regulator theory, to strike this balance. In order to complete this optimization task, we must first set up the conditions for our estimator and controller. These assumptions and rules will govern the building blocks of how our system will be implemented.

3.1 Finite Time, Non-linear Time-varying Problem

Following controller design theory from Bryson [7], we start with the more general problem where the state, X is described by

$$\dot{X} = f(X(t), U(t), t) \tag{24}$$

This handles a general class of non-linear, time-varying systems. A well known cost function for these problems is the quadratic performance index

$$J = \frac{1}{2} \cdot X_f^T \cdot Q_f \cdot X_f + \frac{1}{2} \cdot \int_{t_o}^{t_f} (X^T \cdot Q \cdot X + U^T \cdot R \cdot U) dt \tag{25}$$

The states for this problem are typically formulated as error states that we would like to regulate as close to zero as possible for a given amount of control usage. The general form of the problem results in a two-point boundary value problem which cannot readily be solved online. To make our lives easier, we would like to make some

assumptions to give us a solution that could be evaluated online. The ideal would be a solution that could be evaluated on-board a satellite's navigation computer.

3.2 Finite Time, Linear Time-invariant Problem

The assumption of a linear time-invariant system allows the state to be described by the state-space equation:

$$\dot{X} = A \cdot X + B \cdot U \tag{26}$$

where A and B are constant matrices. Using a quadratic performance mentioned in the previous section, the optimal control solution of this problem is given by

$$U = -K \cdot X \tag{27}$$

where the controller gain K is given by

$$K = R^{-1} \cdot B^{T} \cdot P(t) \tag{28}$$

where P(t) is the solution of a Riccati differential equation

$$-\dot{P} = A^{T} \cdot P(t) + P(t) \cdot A - P(t) \cdot B \cdot R^{-1} \cdot B^{T} \cdot P(t) + Q \tag{29}$$

While this Riccati differential equation is solvable, the process would not be described as easy or useful for near real-time on-board calculations. Note that the LTI system has an optimal control law with time-varying gains [13].

3.3 Infinite Horizon, Linear Time-invariant Problem

If we allow our final time to approach infinity, we can assume for a stable system that the regulated system will approach steady state. As t_f approaches infinity, the

performance index is dominated by the steady state nature, so P(t) approaches P_{ss}. As

P(t) approaches a constant value, $\dot{P}$ approaches zero. Under these conditions, the Riccati

differential equation from the previous section becomes an algebraic Riccati equation

$$0 = A^T \cdot P_{ss} + P_{ss} \cdot A - P_{ss} \cdot B \cdot R^{-1} \cdot B^T \cdot P_{ss} + Q \tag{30}$$

This algebraic Riccati equation is readily solvable, and this relation will be utilized

in Section 3.5. However,we have made many assumptions to make it to this point, and,

while time-invariance would be nice to have, the states for our orbiting satellites are not

time-invariant. Due to the repetitive nature of orbiting satellites and their perturbations, a

time-varying time periodic description would hold more true (see Section 2.1.2). This

time periodic assumption will be used in the next section.

3.4 Linear Time Periodic Method (LTP)

The importance of the Riccati equation for controls, signals, and systems has

sparked much research on the time-varying periodic Riccati equation. Following a

method proposed by Bittanti, et al [3], the following state-space equations were used to

describe our orbital system:

$$\dot{X}(t) = A(t) \cdot X(t) + B \cdot U(t) + w(t)$$
$$Y(t) = C \cdot X(t) + v(t) \tag{31}$$

Where U(t) was the control input, X(t) was the state, and Y(t) was the output.

A(t) was a periodic matrix of period T such that:

$$A(t + T) = A(t) \tag{32}$$

With the understanding that there is no such thing as a completely deterministic

process, dynamics noise w and measurement noise v were used to describe model

uncertainties, non-linearities, perturbations, or any other constraint on the actual system that was not easily described mathematically. As will be tested and shown later, the measurement noise was one of the big drivers constraining the performance of the systems. Variables w and v were defined as uncorrelated zero-mean white Gaussian noises with covariance

$$E\{w \cdot w^T\} = V1 \text{ and } E\{v \cdot v^T\} = V2 \tag{33}$$

For this thesis, only the A matrix was variable. Both the B and C matrices were set as constant matrices.

$$B = \begin{pmatrix} 0 & 0 & 0 \\ 0 & 0 & 0 \\ 0 & 0 & 0 \\ 1 & 0 & 0 \\ 0 & 1 & 0 \\ 0 & 0 & 1 \end{pmatrix} \tag{34}$$

The physical meaning of this B matrix was that for all time, the control system had perfect firing of its thrusters in each direction exclusively. This would mean that when the thruster was fired in the y-direction, all the thrust was concentrated solely in the y-direction. Further, each thruster was identical in performance capability. This was an ideal situation, and any deviations from this perfection were modeled as a portion of the dynamics noise w in the system. The standard deviation for truth model dynamics noise used was consistent with findings from a paper by Bordner and Wiesel that a comparable uncontrolled satellite would drift approximately 2 m/day in each direction [5].

$$C = \begin{pmatrix} 1 & 0 & 0 & 0 & 0 & 0 \\ 0 & 1 & 0 & 0 & 0 & 0 \\ 0 & 0 & 1 & 0 & 0 & 0 \end{pmatrix} \tag{35}$$

26

The physical meaning of this C matrix was that, in the absence of measurement noise v, the control system would receive perfect absolute GPS position readings in the x, y, and z directions. Again, this was an ideal situation, and deviations from this perfection were modeled as the measurement noise v in the system. Since the absolute GPS position error doubles in the vertical direction, the standard deviations for measurement noise v were modeled as 4 m in the radial x direction and 2 m in both the in track y direction and cross track z directions [4].

The periodic Riccati equation which solves the state-space system of equations is

$$-\dot{P}(t) = A(t) \cdot P(t) + P(t) \cdot A(t)^T - P(t) \cdot C(t)^T \cdot V2^{-1} \cdot C(t) \cdot P(t) + B(t) \cdot V1 \cdot B(t)^T \quad (36)$$

The Hamiltonian matrix corresponding to the periodic Riccati equation is

$$H(t) = \begin{bmatrix} A(t)^T & -B(t) \cdot V1 \cdot B(t)^T \\ -C(t)^T \cdot V2^{-1} \cdot C(t) & -A(t) \end{bmatrix} \quad (37)$$

This Hamiltonian matrix has symplectic characteristics, following the relationship

$$H(t)^T \cdot J + J \cdot H(t) = 0 \quad (38)$$

where J is the symplectic matrix consisting of zeros and identity matrices

$$J = \begin{bmatrix} 0 & I \\ -I & 0 \end{bmatrix} \quad (39)$$

The Hamiltonian transition matrix $\Phi_H(t,t_o)$ also has symplectic characteristics following the relationship,

$$\Phi_H(t,t_o)^T \cdot J \cdot \Phi_H(t,t_o) = J \quad (40)$$

The Hamiltonian transition matrix can be partitioned into four n x n blocks,

$$\Phi_H(t,to) = \begin{bmatrix} \Phi_{11}(t,to) & \Phi_{12}(t,to) \\ \Phi_{21}(t,to) & \Phi_{22}(t,to) \end{bmatrix} \quad (41)$$

The solution to the periodic Riccati equation with initial condition Po at time to is

$$P(t) = (\Phi_{21}(t,t_o) + \Phi_{22}(t,t_o) \cdot Po) \cdot (\Phi_{11}(t,t_o) + \Phi_{12}(t,t_o) \cdot P_o)^{-1} \quad (42)$$

Once this solution was computed over one orbit, it could be used to compute the optimal control gain and would be repeated exactly for all the following orbits. Similar to the use of the term "exactly" in earlier sections, deviations to this mode were modeled as dynamics noise w and measurement noise v. In order to verify that this solution was accurate, checks of the symplectic characteristics of each of the building blocks were made. For details on these checks, their anomalous results, and the many attempts to modify the system to get positive results, see Appendix A.

It is important to note that between this section and the next, there is an important shift in both the underlying method and the tool used. As this section attempted to solve the periodic Riccati equation using code written in the fortran computer language, the next section will instead solve the algebraic Riccati equation using the standardized controls routines of Matlab. A comparison of fortran code's solution of the algebraic Riccati equation to Matlab's solution of the corresponding algebraic Riccati equation yielded errors on the order of 1E-29, so either tool could handle this simpler problem. Similar to Irvin's State Dependent Riccati Equation (SDRE) method, the solution to the algebraic Riccati equation was assumed valid for this application because, in effect, we made a linear solution fit a curve by re-linearizing for each of the 25,000 time steps over the orbit [11].

3.5 Periodic Riccati Equation - Linear Quadratic Gaussian (LQG) Method

Optimal control theory provided a tunable solution to our periodic problem with the linear quadratic Gaussian (LQG) method combining a linear quadratic regulator with a Kalman filter. Following Maciejowski, the state-space form of our problem was the same as in the previous section [17].

$$\dot{X}(t) = A(t) \cdot X(t) + B(t) \cdot U(t) + w(t)$$

$$Y(t) = C(t) \cdot X(t) + v(t)$$

(43)

The separation principle was used to solve this LQG problem for the optimal solution. Basically, the linear quadratic regulator operates on $\hat{X}$, the optimal estimate of state X from the Kalman filter much as it would if the full state were available as a measurement for feedback. By combining the regulator and filter, LQG theory guarantees at least stability for a nominal system, but not necessarily robustness.

3.5.1 Kalman Filter. Kalman filter theory provided the means for estimating the state X. The Kalman filter, as seen below in Figure 11, would take inputs of the plant input U and plant output Y. The Kalman filter would produce an output of the state estimate vector $\hat{X}$.
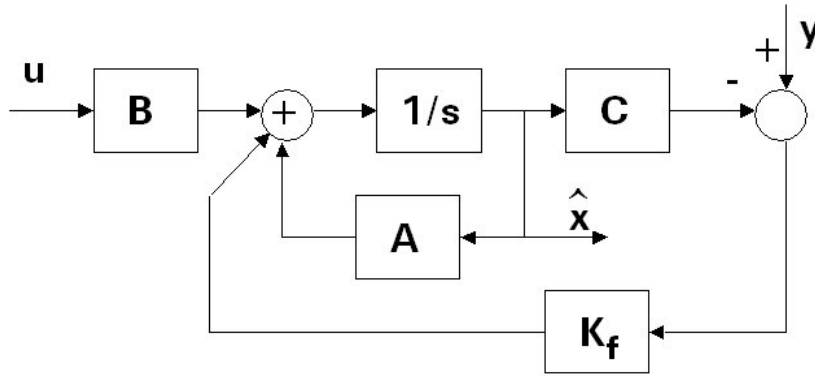
Figure 11. The Kalman Filter [17]

The object of the Kalman filter problem is to minimize the cost

$$J = E\{[(X(t) - \hat{X}(t)] \cdot W(t) \cdot [(X(t) - \hat{X}(t)]^T\}$$

(44)

The Kalman filter gain matrix K_f was calculated as

$$K_f = P_f \cdot C^T \cdot N2^{-1}$$

(45)

where Pf was the solution to the algebraic Riccatti equation

$$P_f \cdot A^T + A \cdot P_f - P_f \cdot C^T N2^{-1} \cdot C \cdot P_f + N1 = 0 \qquad (46)$$

The filter dynamics noise N1 and measurement noise N2 tuning parameters would be varied to optimize the Kalman filter's estimate of the state $\hat{X}$. The starting point was to set the N1 value to the expected standard deviation squared for the truth model's dynamics noise V1 (standard deviation of 2 meters per day), and the N2 value was varied as orders of magnitude of the expected standard deviation squared for the truth model's measurement noise V2 (standard deviation 4 meters in the radial direction and 2 meters in the in-track and cross-track directions) [4, 5]. Now that the Kalman filter is set to the "truth" noises, we tune the filter gain by varying the magnitude of N2 to get the response we want. When you increase the magnitude of N2, you are telling the filter not to believe the measurements as much. When you decrease the magnitude of N2, you are telling the filter that the measurements it receives are really accurate, and it should believe them more. Usually, it is better to tune the filter first for one noise (N2), and then the other (N1). Measurement noise N2 was chosen as the first tuner because, as mentioned earlier in this chapter, measurement noise has a much bigger effect on system performance for our system. As noted later in the thesis, the effects of changing N1 are very slight.

3.5.2 Full State Feedback Regulator. The object of the regulator problem was to come up with the control signal to minimize the cost

$$J = \int_0^T ((Xdes - X)^T \cdot Q \cdot (Xdes - X) + U^T \cdot R \cdot U)dt \qquad (47)$$

from the initial state-space description in Equation 43. The solution was to keep control signal U as a linear function of the state, or in this case of the state error $(X_{des} - X)$

$$U = - K_c \cdot (X_{des} - X) \qquad (48)$$

The optimal state-feedback matrix K_c was calculated as

$$K_c = R^{-1} \cdot B^T \cdot P_c \qquad (49)$$

where P_c was the solution to the algebraic Riccati equation

$$A^T \cdot P_c + P_c \cdot A - P_c \cdot B \cdot R^{-1} \cdot B^T \cdot P_c + Q = 0 \qquad (50)$$
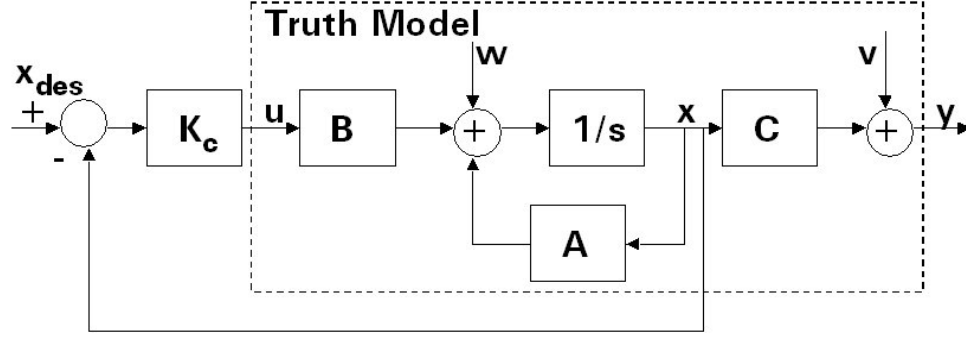
Figure 12. Optimal Full State Feedback Regulator

Attached to the truth model, the optimal full state feedback regulator would try to drive the state error (X_{des} - X) to zero. The Q and R values were tuned to produce the optimal response via gain K_c. Following a method proposed by Irvin, the Q value was initially set to identity, and then the R values were varied by orders of magnitude [9]. Once the acceptable R value, in terms of control usage and RMS error, was found, Q values were tweaked to see if improvements could be made. The process is explained more in the following chapters, but eventually controller tuning values of R = 1E-4 and Q = 1E0 were found to be the best compromise for comparisons of the different models.

The truth model was used to output not only the measurements of the true state as calculated by the fortran routines from Section 2.2.1, but it also added the perturbing noises w and v (of variance V1 and V2) to account for un-modeled disturbances. Note that the truth model was not changed during the tuning. In essence, we cannot change truth, but by changing the gain of the regulator, we controlled how the regulator interpreted what it saw (X_{des} - X), and, thus, how it reacted (U).

3.5.3 Output Feedback Compensator. The Kalman filter and controller were married together in series to form a new optimal output feedback compensator as seen in Figure 13. Similar to the regulator tuning, variations on Q and R were used to optimize the controller gain K_c. To provide even better results, the filter N1 and N2 tuning values were tweaked as in Section 3.5.1 to optimize the Kalman filter gain K_f. Additional details on the actual tuning appears in Appendix B.

Once the model was tuned, additional scenarios involving the different A matrices from Section 2.2.2 were executed to compare the degradation when switching from time varying control to time invariant control. Note that when we switch from time-varying to time-invariant control, the truth model must remain the same.
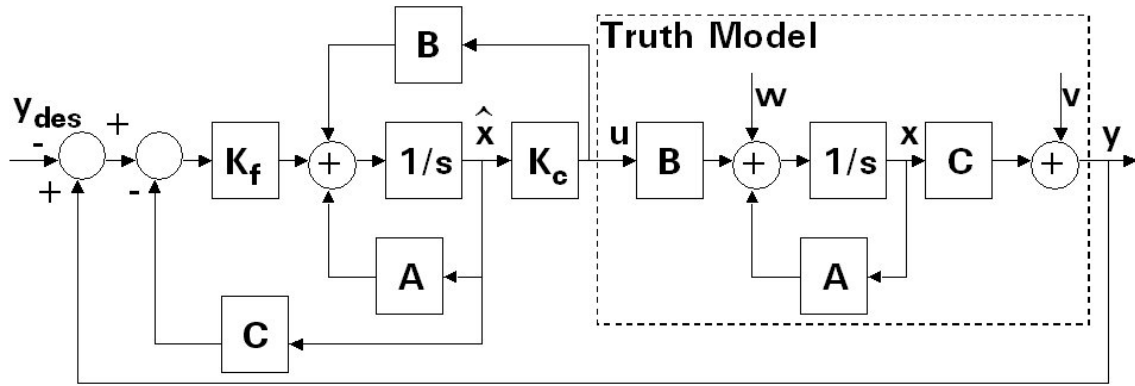
Figure 13. Output Feedback Compensator [17]

IV. Full State Feedback Regulator Results

In order for the regulator and compensator to be tuned and checked for validity, Monte Carlo data runs were executed. For response to initial conditions, only one Monte Carlo run was accomplished; multiple runs would be needed for statistical measurements. For both the regulator and compensator, the scenarios were originally run with an initial perturbation of 10 meters in the radial direction. Some later runs used initial perturbations of greater magnitudes or in other directions, but for comparative purposes, the 10 meter initial radial perturbation was used as the standard. This perturbation would be consistent with the perturbation caused by increased solar activity such as the increased air drag due to a small solar flare. This chapter will present the results with figures and tables focused on the control and RMS error. The RMS error was calculated as steady state RMS error by averaging the RMS error over one orbit with no initial perturbation. Settling times were figured using a 5% of steady state threshold.

4.1 Full State Feedback Regulator, Initial Perturbation Dx = 10 meters

The first step of the tuning process for the output feedback compensator was to set up and tune the full state feedback regulator. As mentioned in the previous chapter, the full state feedback regulator is more of an idealized system where your controller can see all of the states without any measurement noise v distorting the measured feedback. As can be seen in Figure 14 below, although the system does not receive measurement noise v in the feedback, the dynamics noise w of the truth model does factor into the system. But as noted in the last chapter, the magnitudes of the dynamics noise (standard deviation of 2 m/day) were small enough for the system to handle them without much problem.

Although ideal, the results of the regulator tuning process proved to be useful in the later tuning of the more realistic compensator. Results of control versus settling time and control versus RMS error were compared to find the optimum values for the R tuning parameter. Although data will be presented for all the tuning values, comments will focus on results for the tuning value R=1E-4.

4.1.1 Time-invariant Anodal Model (AnTI). The first model tested was the case of the time-invariant A matrix in the nodal frame. The physical meaning of this model is that the controller receives full state information and controls the system based on a time-invariant model (single representative snapshot) of the dynamics of the system.
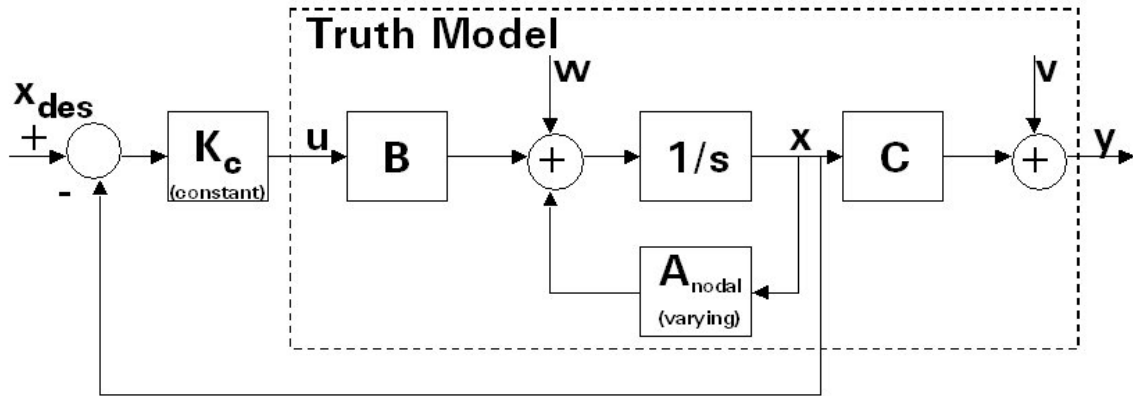
Figure 14. Full State Feedback Regulator, AnTI

Due to the variances in the components of the nodal frame A matrix as detailed in Section 2.3, this method is not expected to perform as well as the other methods. Surprisingly, the idealistic nature of the regulator provides adequate control for this scenario.
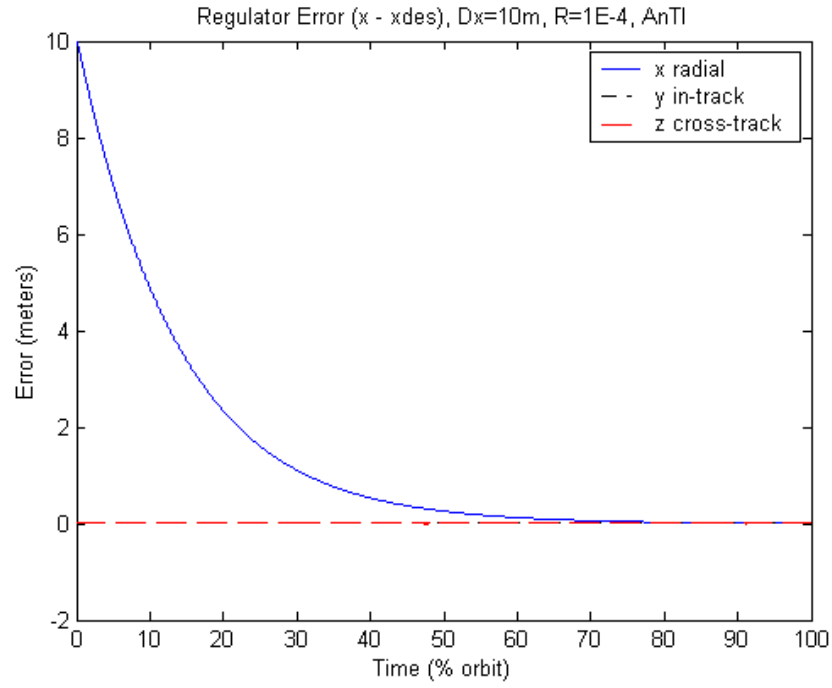
Figure 15. Full State Feedback Regulator Error for R=1E-4, AnTI
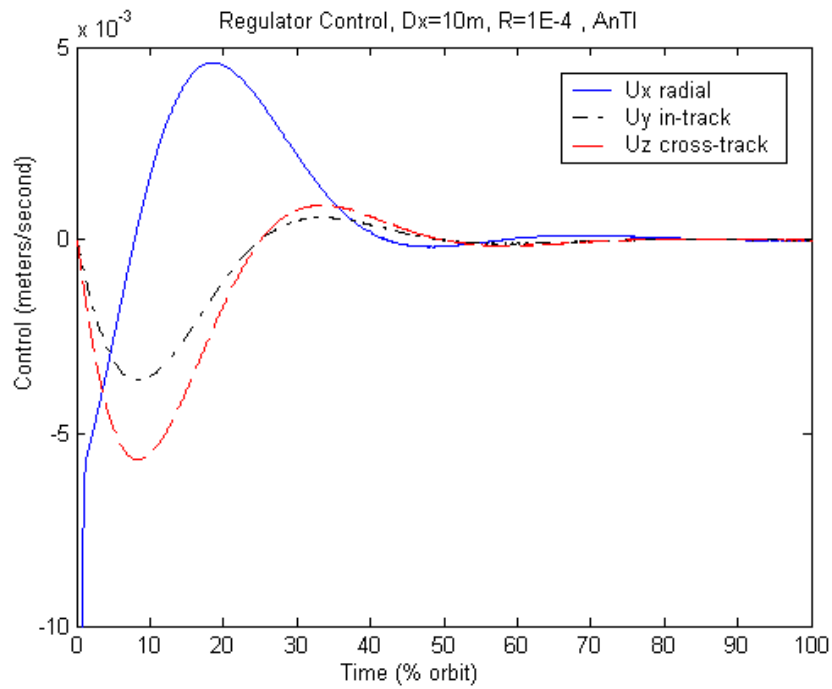
Figure 16. Full State Feedback Regulator Control for R=1E-4, AnTI

4.1.2 Time-varying Anodal Model (AnTV). The time-varying A matrix in the nodal frame was the next regulator model tested. For this model the controller receives the full state information and controls the system knowing the time periodic dynamics of the system at each step of the orbit.
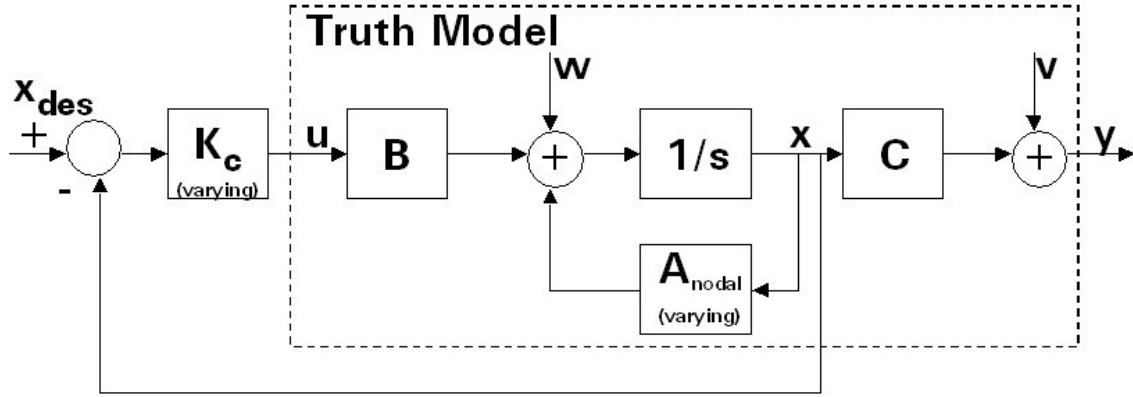
Figure 17. Full State Feedback Regulator, AnTV

The representative plots for error and control over one orbit show acceptable response to the 10 meter initial perturbation for the selected tuning value R=1E-4.

In comparison of Figure 16 and Figure 19, the control responses for the time-varying and time-invariant control are very similar. This shows that for this ideal set-up where the controller was able to see the exact states without measurement noise, even the models that are not well described by LTI, can produce acceptable responses.

Figure 18. Full State Feedback Regulator Error for R=1E-4, AnTV
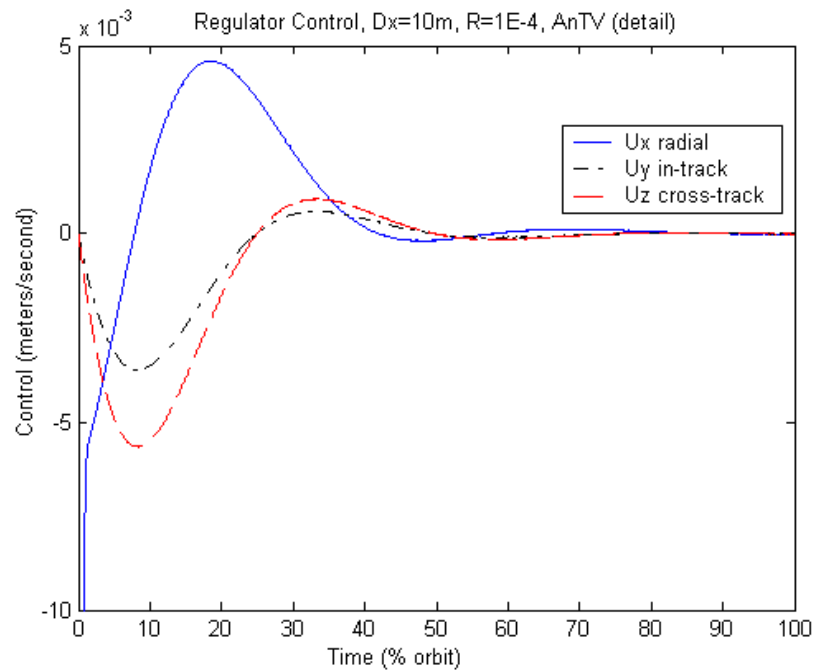
Figure 19. Full State Feedback Regulator Control for R=1E-4, AnTV

4.1.3 Time-varying Aorbital Model (AoTV). The third model tested was the case of the time-varying A matrix in the orbital frame. Similar to AnTV, the physical meaning of this model is that the controller receives the full state information and controls the system knowing the dynamics of the system at each step of the orbit. This time the dynamics of the system are in the orbital frame. Because of the new orbital frame of reference and the inherent adaptability of the time-varying model, this method is expected to provide the best performance.
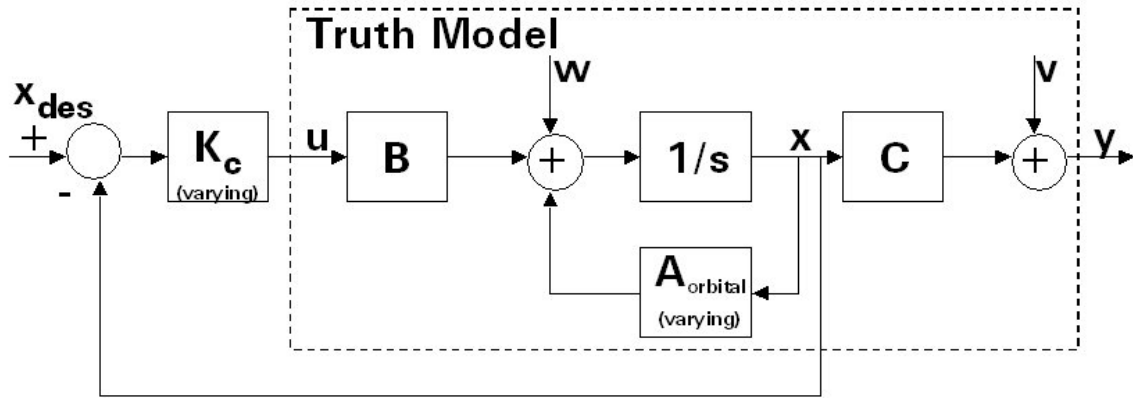
Figure 20. Full State Feedback Regulator, AoTV

The error plot in Figure 21 shows how, due to orbital dynamics, a perturbation in the radial direction will cause the satellite to slow down, and thus degrade the y in-track direction. This type of cross-correlation would need further study, and adjustments to the controller gain would be an area for improvement for the future.
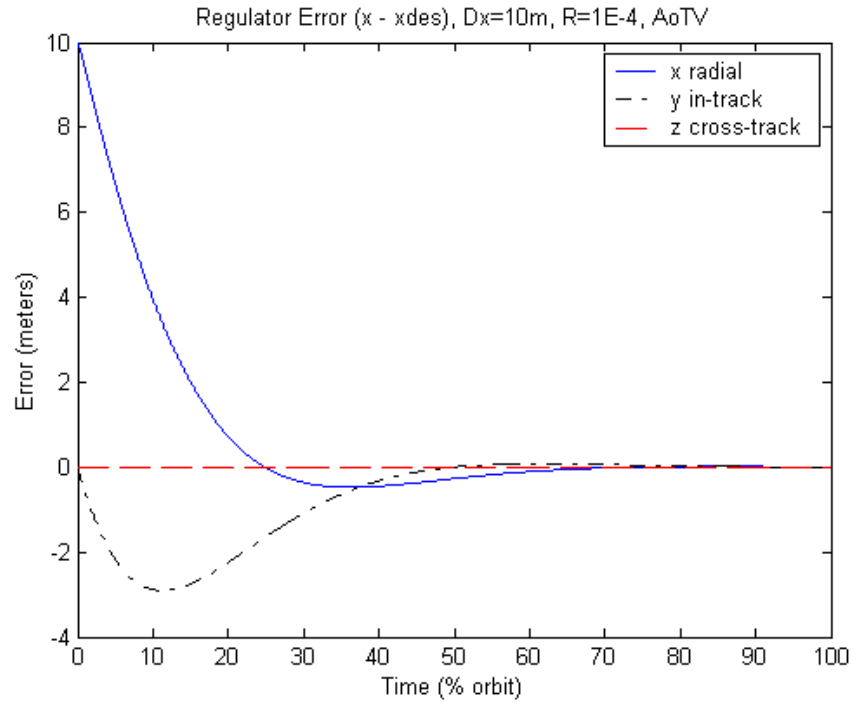
Figure 21. Full State Feedback Regulator Error for R=1E-4, AoTV
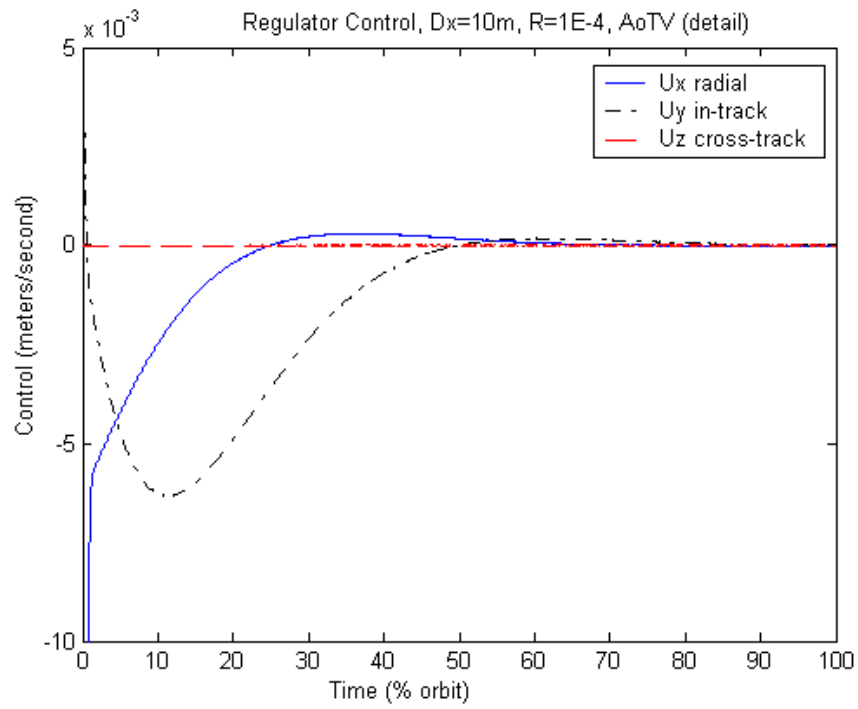
Figure 22. Full State Feedback Regulator Control for R=1E-4, AoTV

4.1.4 Time-invariant Aorbital Model (AoTI). The time-invariant A matrix in the orbital frame was the last regulator model tested. For this model, the controller receives the full state information and controls the system knowing only a single time-invariant snapshot of the dynamics of the system at each step of the orbit. This time the dynamics of the system are in the orbital frame.
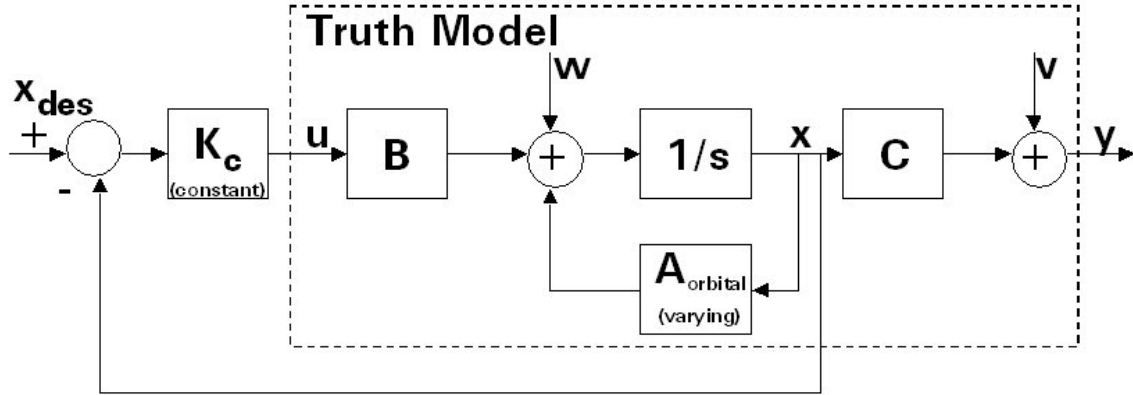
Figure 23. Full State Feedback Regulator, AoTI
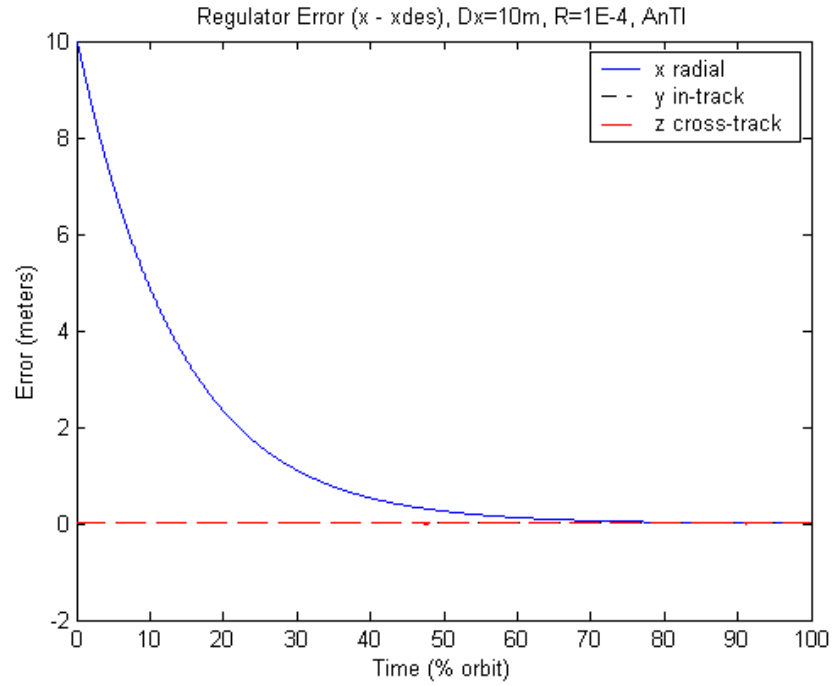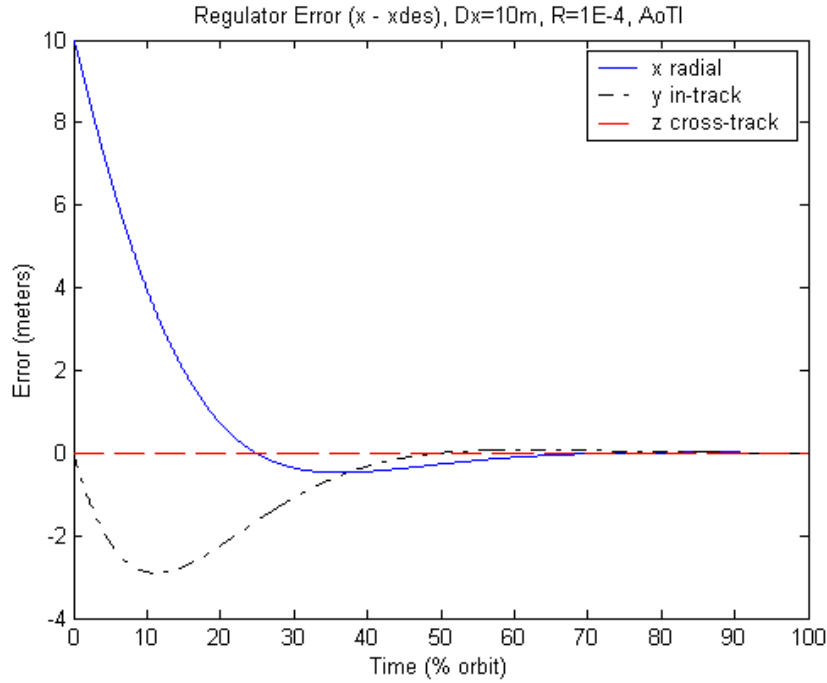

Figure 24. Full State Feedback Regulator Error for R=1E-4, AoTI
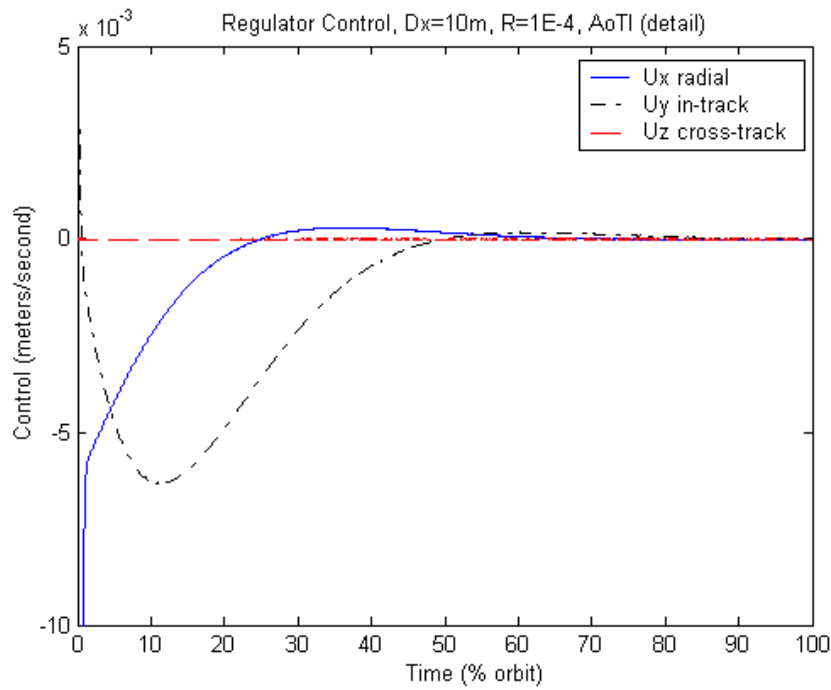
Figure 25. Full State Feedback Regulator Control for R=1E-4, AoTI

4.1.5 Regulator Model Comparisons. The results for the four models were compared for control, RMS error, and settling time over an order of magnitude range of controller tuning values from R=1E-6 to R=1E0. Each data point on the figures below represents the value for one particular tuning value for R. For completeness, R values above and below this range were tested to ensure the trends of the data did not change for the extremes.
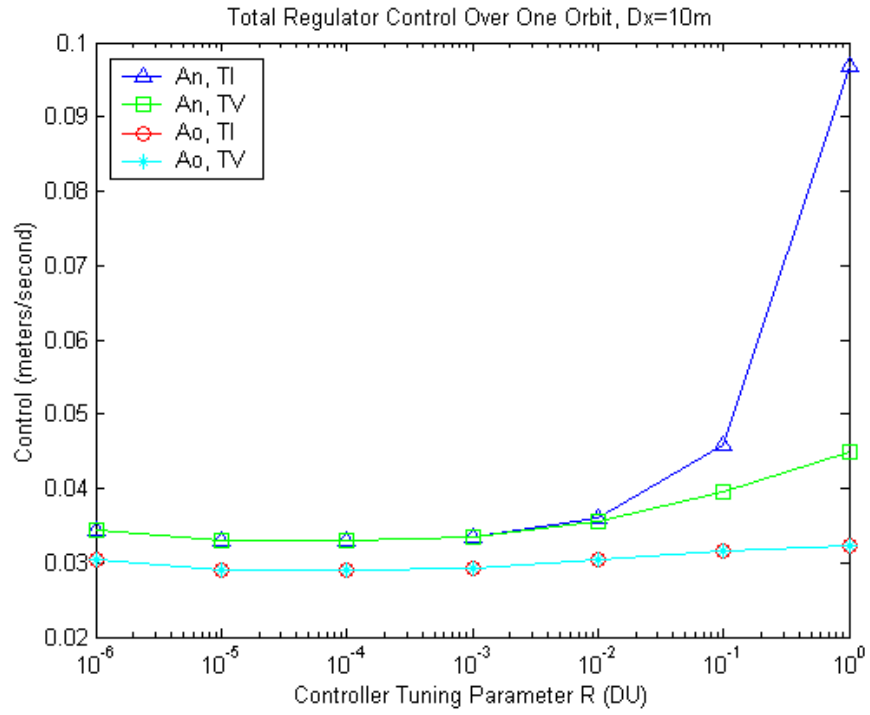
Figure 26. Full State Feedback Regulator Control, Tuning R's
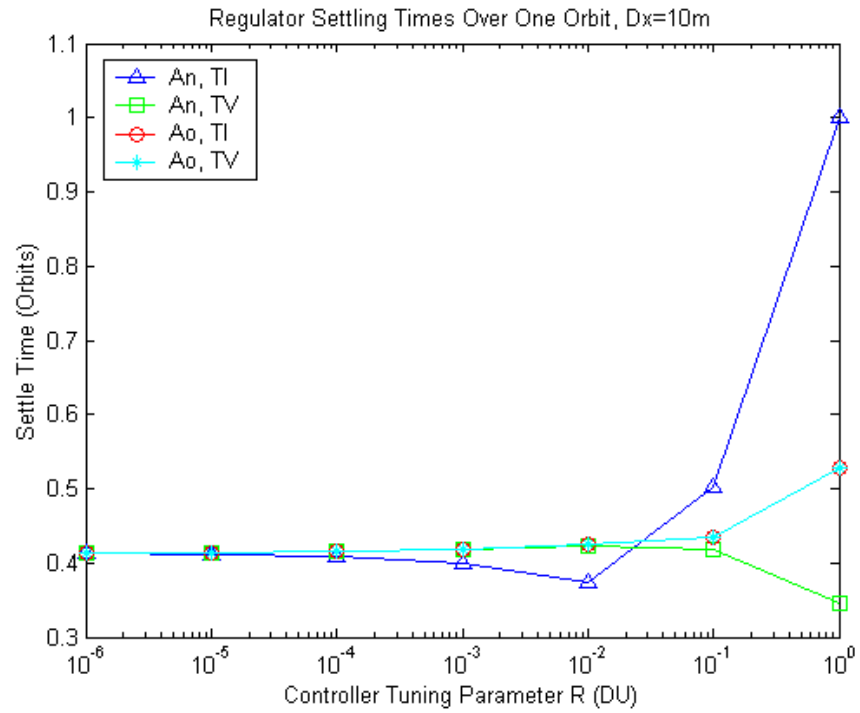
Figure 27. Full State Feedback Regulator Settling Times, Tuning R's

For three out of four models, the results of the control versus settling time plot clearly favored a tuning value of R=1E-4. The one undecided model, AnTI, was not sure if it liked R=1E-4 (which gave it lower control) or R=1E-3 or R=1E-2 (which gave it lower settling time). Physically, the R=1E-4 value translates to telling the controller that the errors it should correct are reliable but not to be trusted fully. The goal of the tuning process is to minimize both control and settling time, which corresponds to the lower left corner of Figure 28 below. Note that the lower magnitudes of tuning value R correspond to the leftmost data points on the figure below.
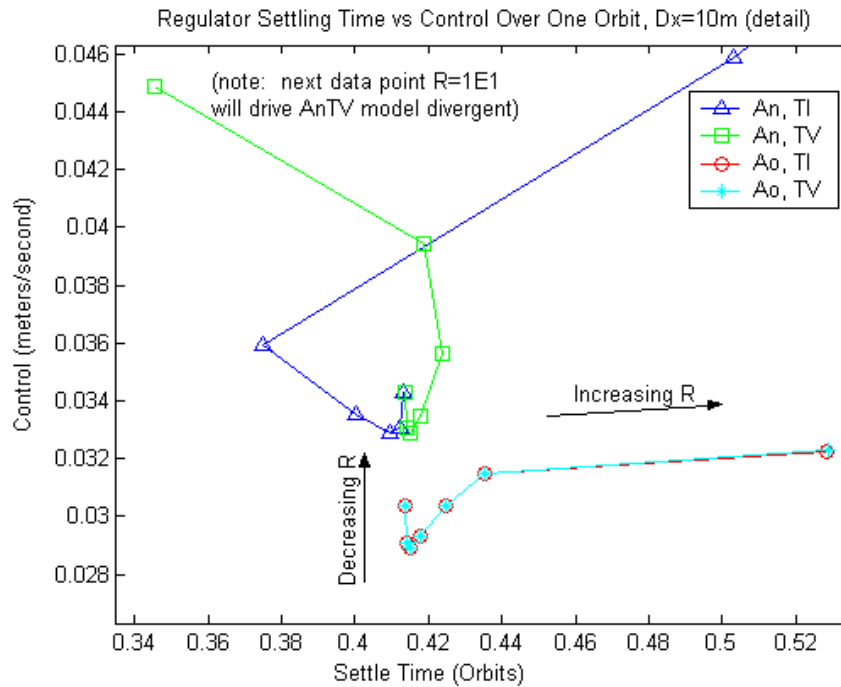
Figure 28. Regulator Settling Time vs. Control, Tuning R's

An important result to note is the consistency of the time-varying and time-invariant results for the orbital A matrix. As can be seen in the figure above as well as Tables 2 - 4, control, RMS errors, and settling times were nearly identical for AoTI and AoTV for all values for R. Referring back to Section 2.3.2, where the A matrix

43

components in the orbital frame are compared over one orbit, it becomes clear why AoTI

and AoTV should produce very similar results. That was the reason for this frame

change: to get an A matrix that looks very close to being constant over the whole orbit.

The variability of the nodal frame components (see Section 2.3.1) could be a reason as to

why the orbital frame models consistently required 14% less fuel. The complexity of the

model trying to manipulate all the widely varying periodic changes of the dynamics could

cause the system to overwork itself, spending more fuel. The nodal controller might

overcompensate and under-compensate more compared to the orbital frame models,

where the system knows pretty well what its baseline is. Notice the big overshoots for

the control plots for the nodal frame models versus the small overshoots for the orbital

frame models. Although the time-invariant Anodal scenario varied a little from the rest,

for the target tuning values of 1E-6, 1E-5, and 1E-4, time-varying and time-invariant

methods produced control, RMS errors, and settling times nearly the same for AnTV and

AnTI.

Table 2. Regulator Total Control Over One Orbit, Dx = 10 m

Control (m/sec)	R=1E-6	R=1E-5	R=1E-4	R=1E-3	R=1E-2	R=1E-1	R=1E0
AnTI	0.0343	0.0331	0.0329	0.0335	0.0359	0.0459	0.0969
AnTV	0.0343	0.0330	0.0329	0.0335	0.0356	0.0394	0.0449
AoTI	0.0304	0.0291	0.0289	0.0293	0.0304	0.0315	0.0323
AoTV	0.0304	0.0291	0.0289	0.0293	0.0304	0.0315	0.0323

Table 3. Regulator Settling Times, Dx = 10 m

(% orbit)	R=1E-6	R=1E-5	R=1E-4	R=1E-3	R=1E-2	R=1E-1	R=1E0
AnTI	41.31	41.22	40.94	40.04	37.48	50.31	>100
AnTV	41.36	41.39	41.48	41.75	42.39	41.86	34.56
AoTI	41.37	41.40	41.49	41.77	42.48	43.52	52.86
AoTV	41.37	41.40	41.50	41.77	42.48	43.53	52.86

Table 4. Regulator Average RMS Error Over One Orbit, Dx = 0 m

Error (meters)	R=1E-6	R=1E-5	R=1E-4	R=1E-3	R=1E-2	R=1E-1	R=1E0
AnTI	0.79E-4	0.54E-4	0.57E-4	0.78E-4	0.52E-4	0.65E-4	0.62E-4
AnTV	0.49E-4	0.67E-4	0.75E-4	0.48E-4	0.86E-4	0.93E-4	0.61E-4
AoTI	0.59E-4	0.60E-4	0.96E-4	0.51E-4	0.60E-4	0.77E-4	0.51E-4
AoTV	0.77E-4	0.68E-4	0.70E-4	0.56E-4	0.45E-4	0.87E-4	0.87E-4

V. Output Feedback Compensator Results

After tuning the full state feedback regulator, the next step was to tune the output feedback compensator. As mentioned in previous chapters, the output feedback compensator is a more realistic system where the compensator can only see the noisy measurement of the position states. Comparing the compensator control plots to the corresponding regulator ones, it is easily seen how the noise degrades the system. But the results of the more realistic compensator proved similar to those of the idealized regulator. The AnTI model was the exception. It diverged for all scenarios, and thus, it will be shown in Section 5.1, but will not be presented in the later comparison scenarios. As mentioned in the previous chapter, RMS error was taken as a steady state value. RMS error tested each specific noise level or step size condition to the same truth model with no initial perturbations. Results of control versus settling time and RMS error were compared to find the optimum values for the controller Q and R tuning parameters as well as the filter N1 and N2 tuning parameters.

5.1 Output Feedback Compensator, Initial Perturbation Dx = 10 meters

As mentioned in the previous section, this scenario, with an initial perturbation of 10 meters in the radial direction, was the standard that will be used to compare to for all the scenarios in following sections.

5.1.1 Time-invariant Anodal Model (AnTI). The first model tested was the case of the time-invariant A matrix in the nodal frame. This is similar to the AnTI

regulator model. But this time the controller receives the noisy output information and controls the system with only a time-invariant snapshot of the dynamics of the system.

Figure 29. Output Feedback Compensator, AnTI

Figure 30. Output Feedback Compensator Error for R=1E-4, AnTI
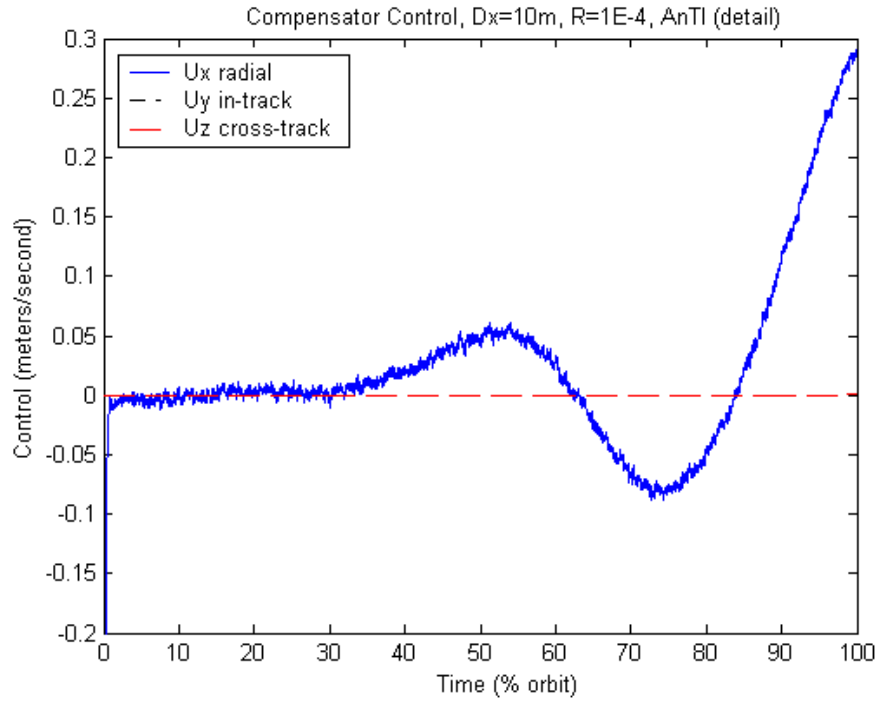
Figure 31. Output Feedback Compensator Control for R=1E-4, AnTI

The AnTI position errors for all tuning values for R would be classified as slowly diverging over the single orbit. Continuing past the one first orbit (see Figure 32 below), the AnTI model continues to diverge with no hope of recovery for any tuning value for R. This trend held true for all of the compensator scenarios tested.
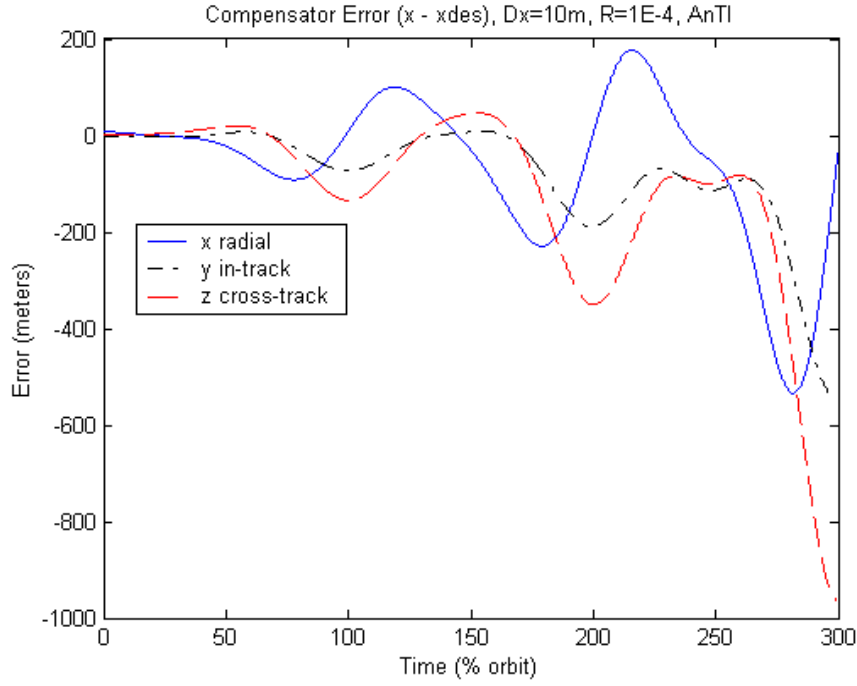
Figure 32. Compensator Error Over Three Orbits, Dx=10m, AnTI

5.1.2 Time-varying Anodal Model (AnTV). The next compensator model tested was the case using the time-varying A matrix in the nodal frame. The physical meaning of this model is that the controller receives the noisy output information and controls the system knowing the dynamics of the system at each step of the orbit.
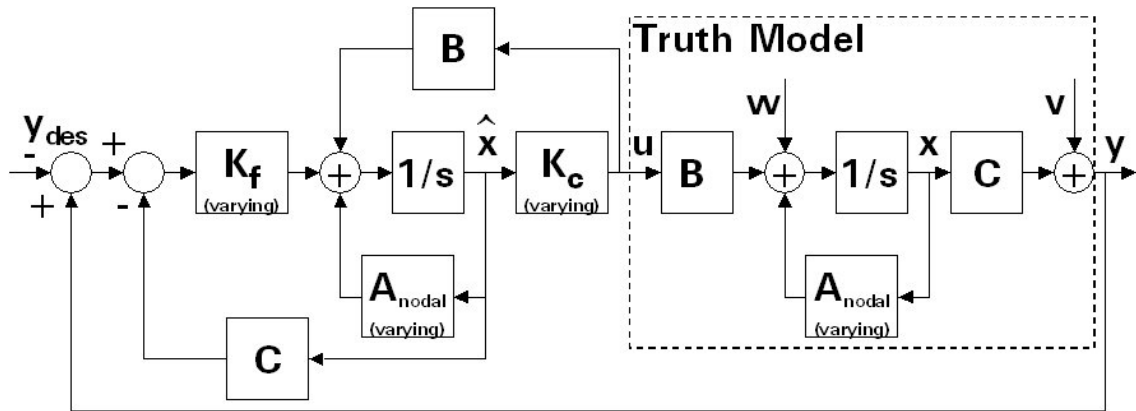
Figure 33. Output Feedback Compensator, AnTV
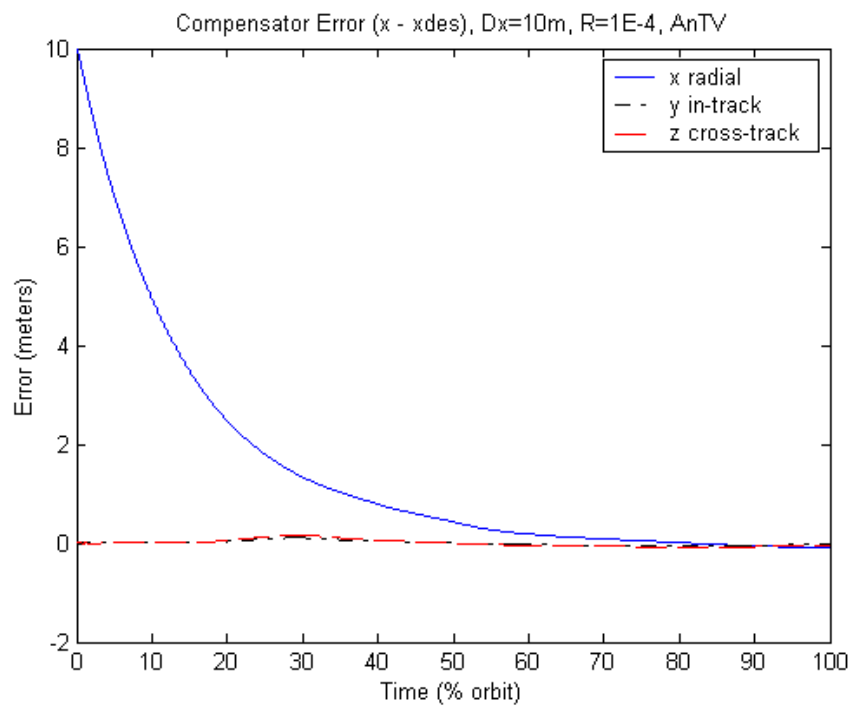
Figure 34. Output Feedback Compensator Error for R=1E-4, AnTV
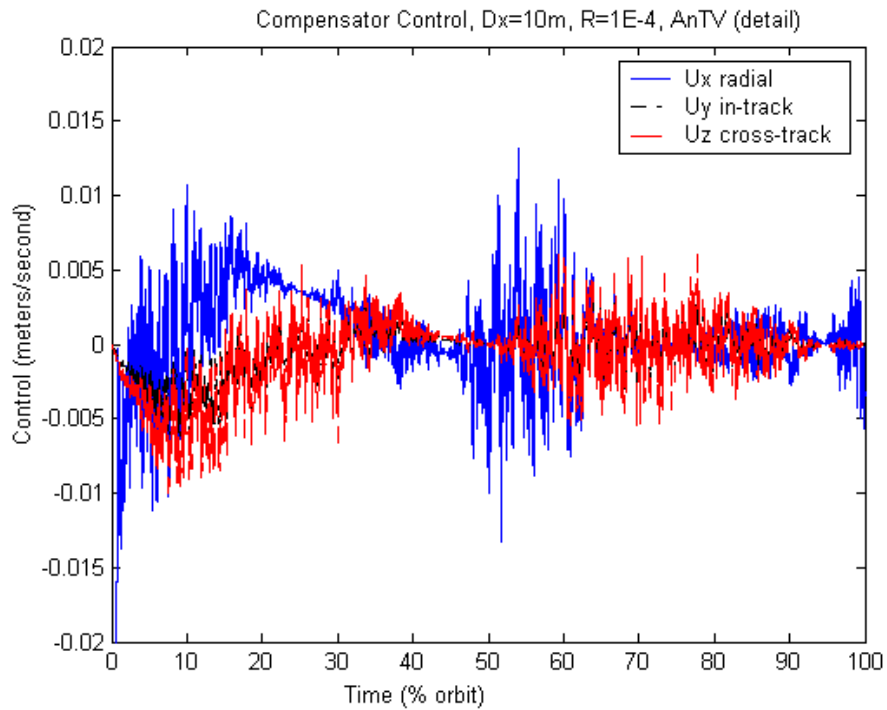
Figure 35. Output Feedback Compensator Control for R=1E-4, AnTV

50

5.1.3 Time-varying Aorbital Model (AoTV). The time-varying A matrix in the orbital frame was the third model tested. For this model, the controller receives the noisy output information and controls the system knowing the dynamics of the system at each step of the orbit. This time the dynamics of the system are in the orbital frame.
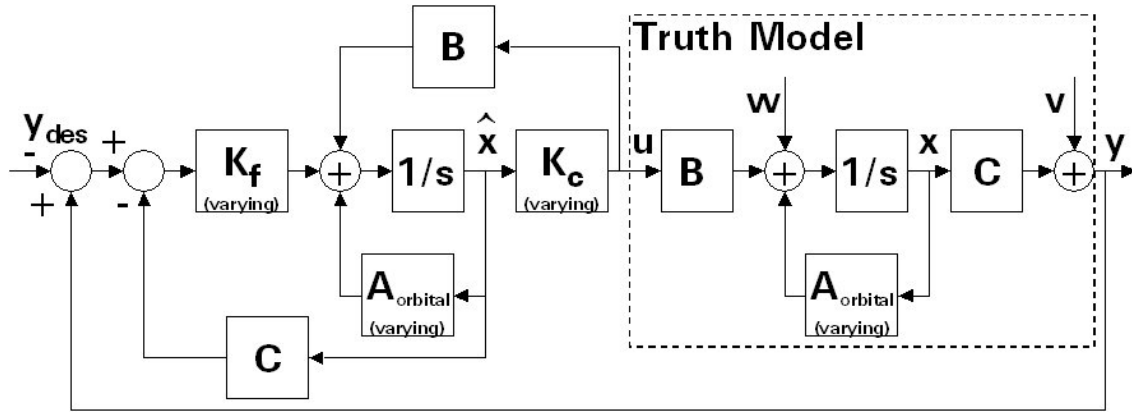
Figure 36. Output Feedback Compensator, AoTV
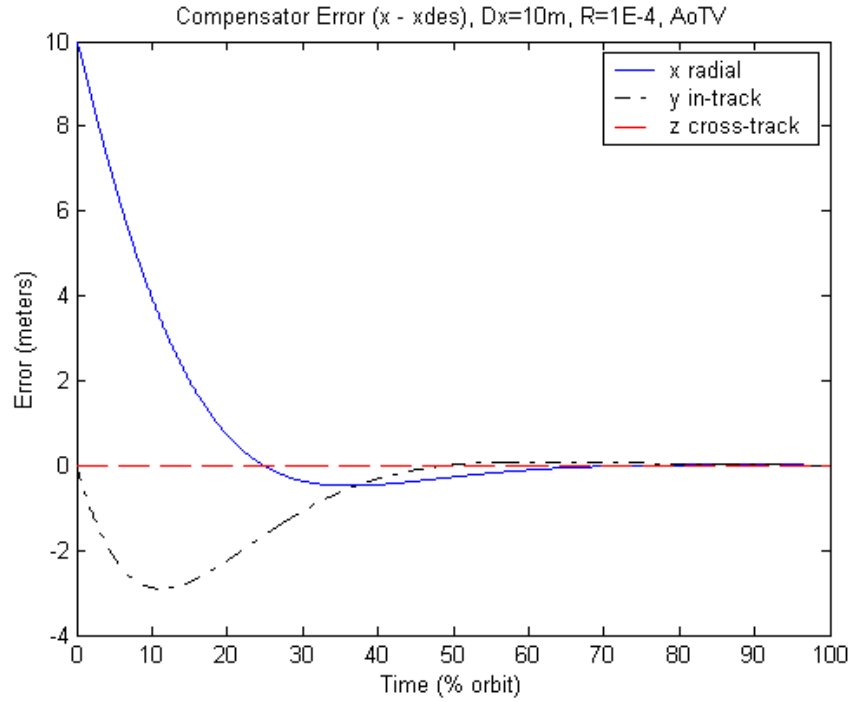
Figure 37. Output Feedback Compensator Error for R=1E-4, AoTV
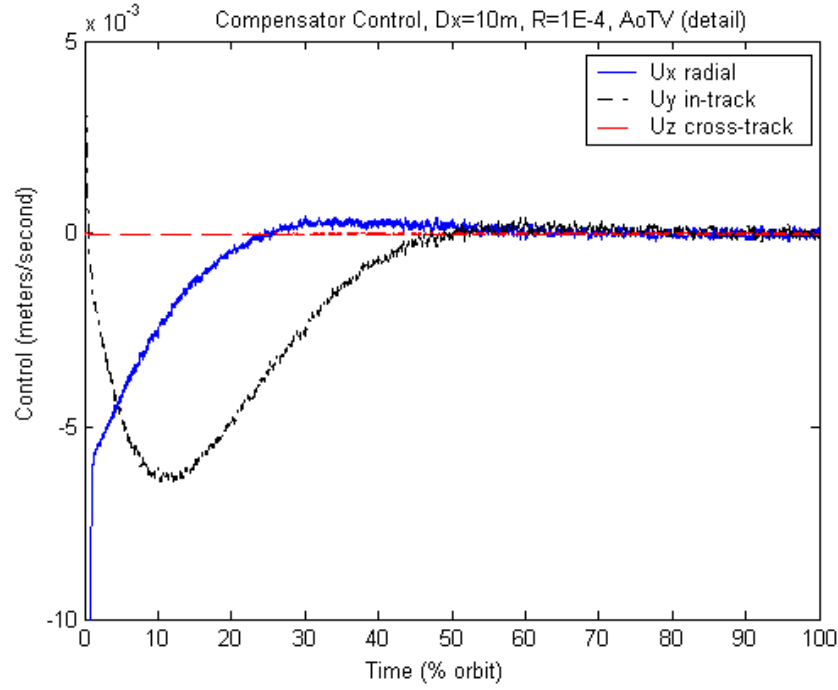
Figure 38. Output Feedback Compensator Control for R=1E-4, AoTV

5.1.4 Time-invariant Aorbital Model (AoTI). The final compensator model tested was the time-invariant orbital frame A matrix. Similar to AnTI, the physical meaning of this model is that the filter and the controller both receive the noisy output information and control the system with only a single representative snapshot of the dynamics of the system. This time the dynamics of the system are in the orbital frame.
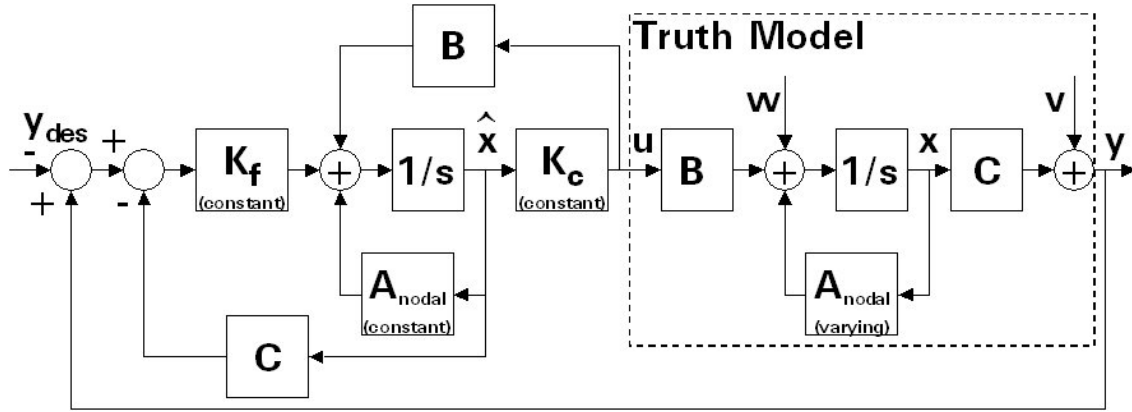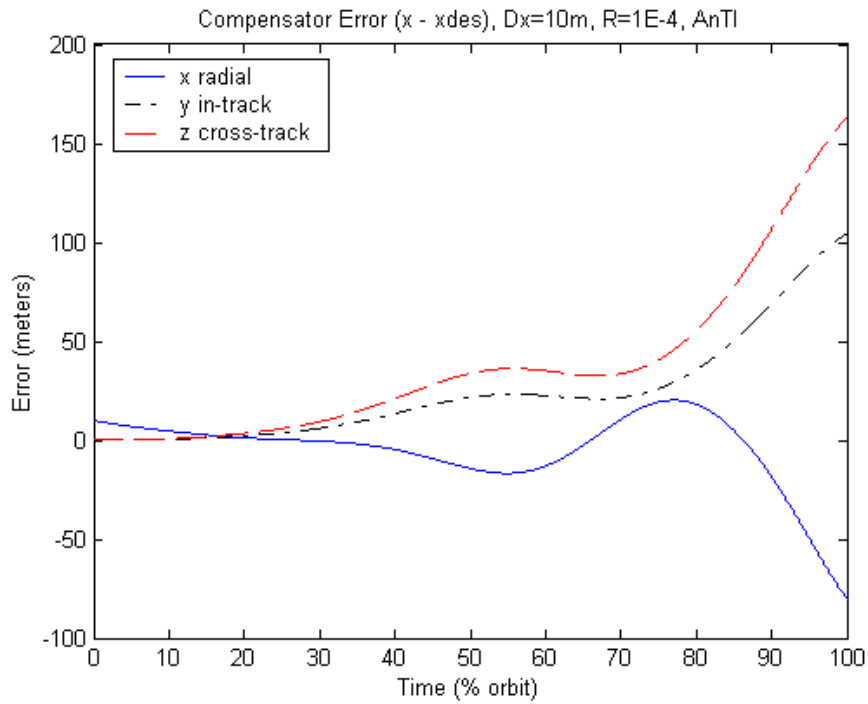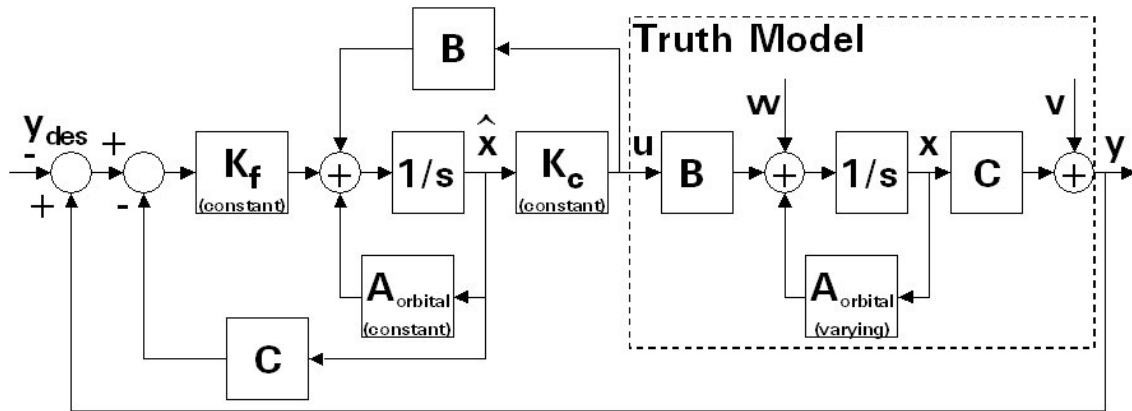

Figure 39. Output Feedback Compensator, AoTI
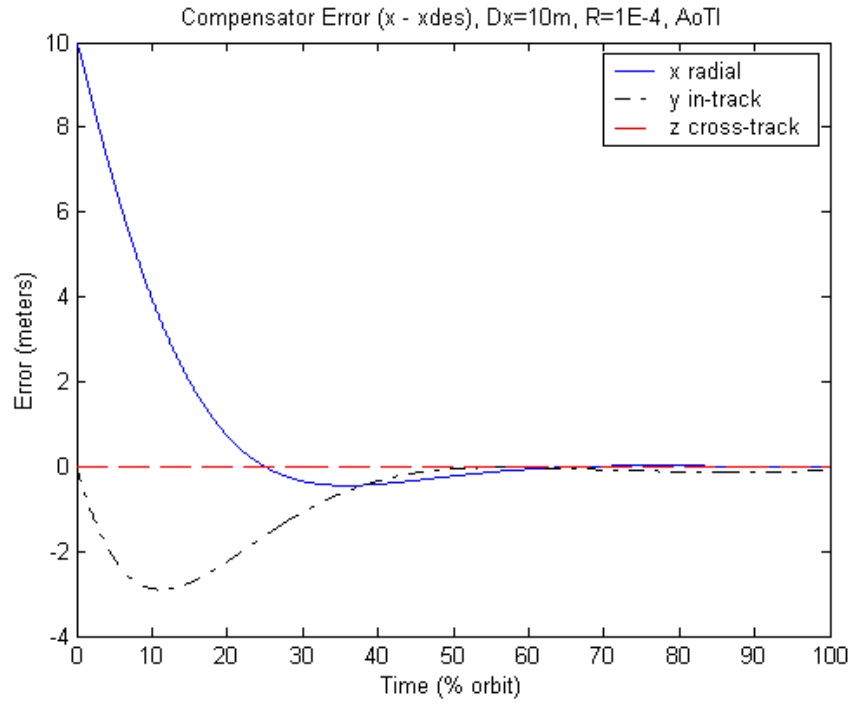
Figure 40. Output Feedback Compensator Error for R=1E-4, AoTI
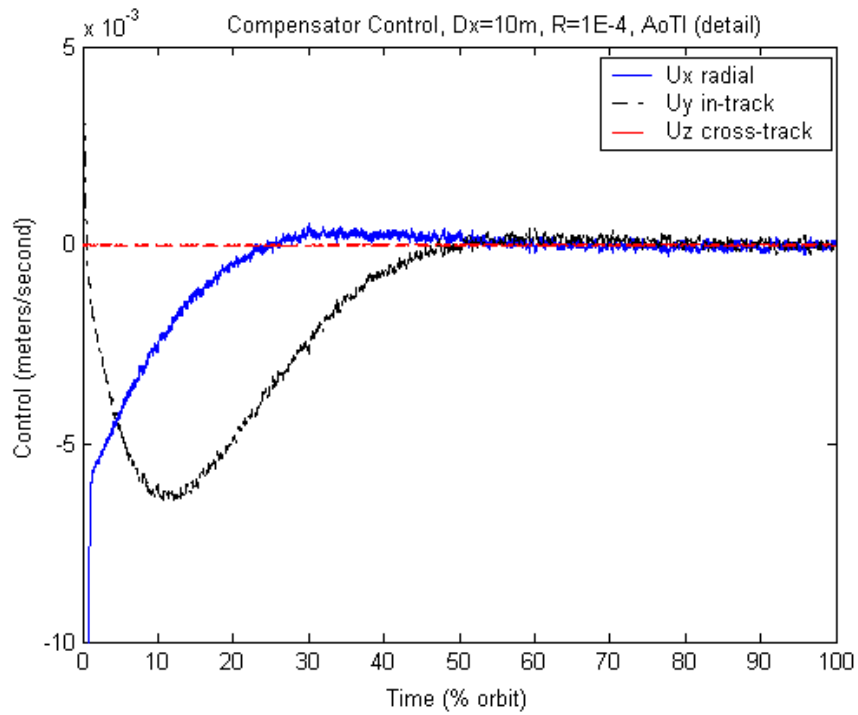
Figure 41. Output Feedback Compensator Control for R=1E-4, AoTI

5.1.5 Compensator Model Comparisons. The results for the three models were compared for control, RMS error, and settling time over an order of magnitude range of controller tuning values from R=1E-6 to R=1E0. This range of magnitudes was validated through the full-state feedback regulator tuning. To ensure completeness, tuning R values above and below this range were also tested, but not shown, to ensure the trends of the data did not change for the extremes of the output feedback compensator as well. Figures for the converging models AnTV, AoTI, and AoTV are presented first with comparative plots for the diverging model AnTI following after.

Note that in the previous chapter for the regulator control plots, we saw the nodal frame models with bigger overshoots than the orbital frame models. Now that measurement noise is added, we see the same basic control plots (a little noisier) for the compensator orbital frame models, but now for the compensator the nodal frame models really start to show how the noise corrupts their attempts to control the system. Compare Figure 6 from Section 2.3.1 with Figure 35 from Section 5.1.2. It becomes noticeable that, as the components of the A matrix begin to periodically propagate from their initial values, the noise drives the control to become more variable. It is important to note here what the A components actually represent are changes to the dynamics state over each step. This A matrix is not diagonal, so the component magnitudes represent correlations between positions and velocities that increase and decrease throughout the orbit. From Equation 43, the total change in the states includes the dynamics state terms plus control plus dynamics noise. Since the expected value of the noise at different points of the orbit stays the same, the noise will play a bigger role when the A matrix components are smaller such as at the initial time. But as time approaches 20-40% of the orbit, control quiets down because the A matrix components periodically increase their magnitudes as they propagate through their orbits. The A matrix dynamics start to dominate over the noise, thus you see less variation in the control plots. But once again, as the A matrix

components start to decrease towards their initial values, the noise again starts to dominate and drives the control to be more variable. Looking at the A matrix elements, most of them propagate to zero at the 1/2 orbit point of time. It is not as noticeable in these plots, but due to its periodic nature, the orbital frame models should also follow this trend to a much lesser degree.
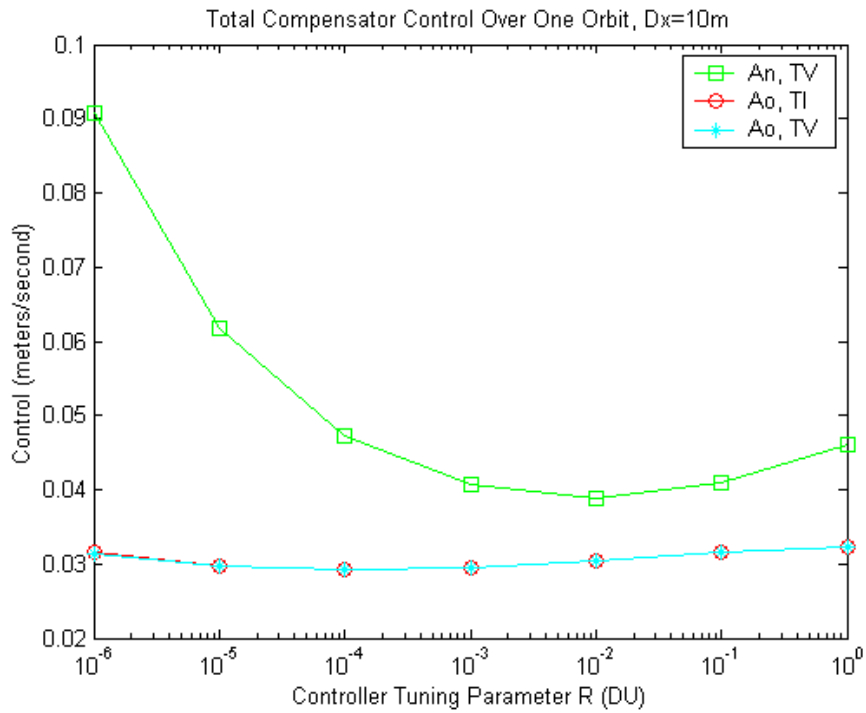
Figure 42. Compensator Control, Dx=10m, Tuning R's
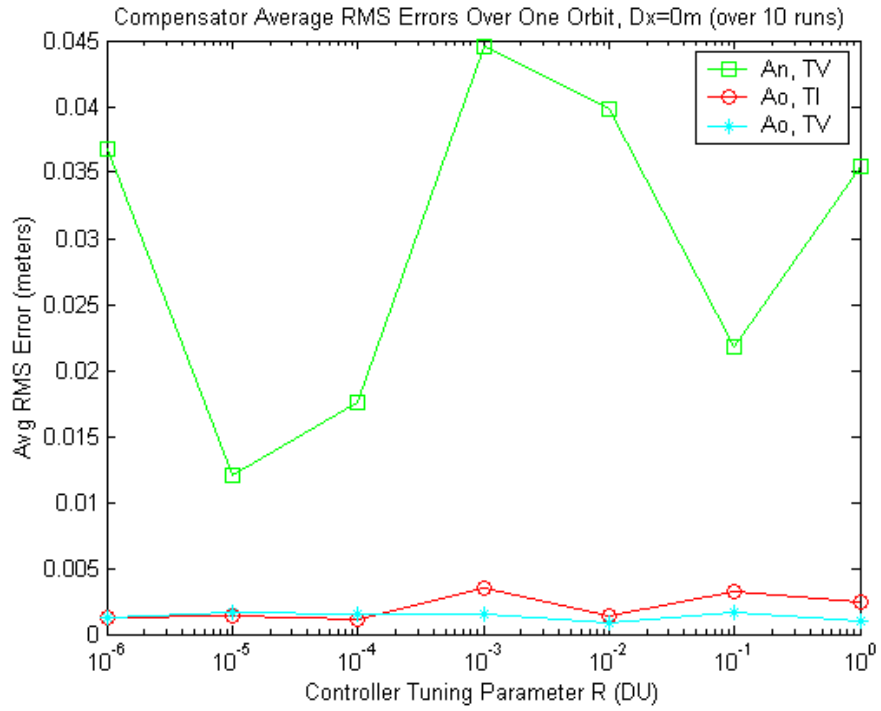
Figure 43. Compensator RMS Error, Dx=10m, Tuning R's
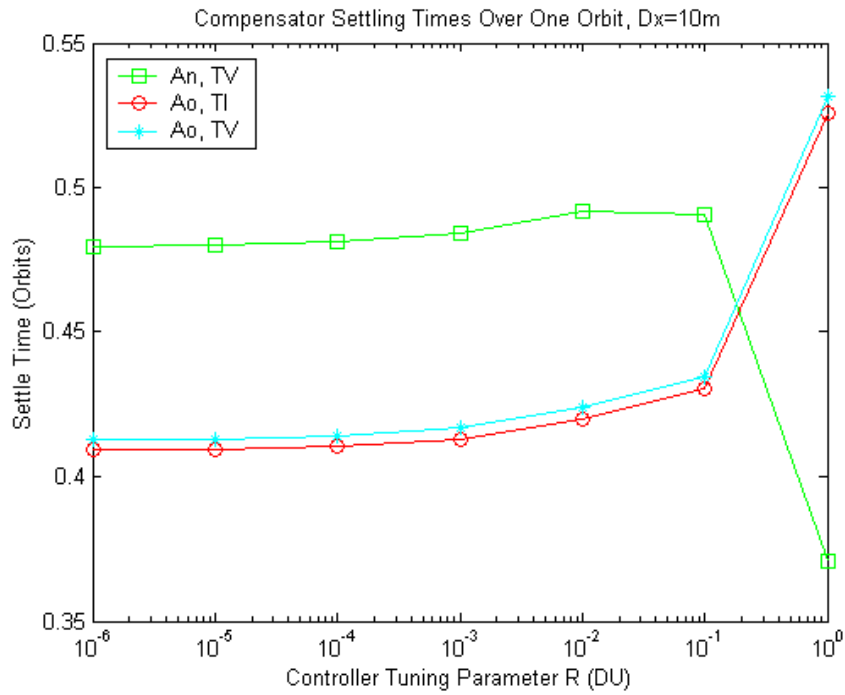
Figure 44. Compensator Settling Times, Dx=10m, Tuning R's

Similar to the regulator results, the above RMS error data (Figure 43) is not very helpful for using trends to tune specific R values, but it does show a trend between the orbital frame models and the nodal frame model. The nodal frame model consistently exceeds an order of magnitude over the orbital frame models. This trend ties into the dynamics and noise correlation discussed earlier in this section.

For settling times, Figure 44, the AnTV value drops dramatically for the R=1E0 tuning value. This trend is the same as was seen with the regulator in Figure 27. Both of the nodal frame regulator models had a minimum settling time value one or two tuning R magnitudes below the tuning value for which they would diverge. For the regulator, AnTI minimized settling time at R=1E-2, while AnTV was minimized at R=1E0 similar to the compensator. For the AnTV compensator model, the next tuning R value of R=1E1 drove the model to diverge. This was a feature of the nodal frame models, and not for the orbital frame models. The orbital frame models were tested over many intermediate R values, but they produced no minimizing settling time dip before they reached the R value where the model diverged. The reason behind the minimum settling time is tied to overshoot. The AnTV model in Figure 34 is over-damped with no overshoot, so it takes it a while to reach the 5% steady state value that settling time requires. The minimized settling times occur when the system is under-damped when the system quickly overshoots and then settles into the 5% steady state value threshold. The next magnitude for tuning R usually provides a diverging system because the overshoot becomes too large for the system to recover from. The orbital frame models did not produce similar trends because, for all presented R values, the error was slightly under-damped. For larger R values, the orbital frame models gracefully became more under-damped. In most cases, an R value of 1E1 drove most systems to divergence. Since this feature only minimized settling time for nodal frame models and did not reduce RMS error or control, it was noted, but not investigated further.
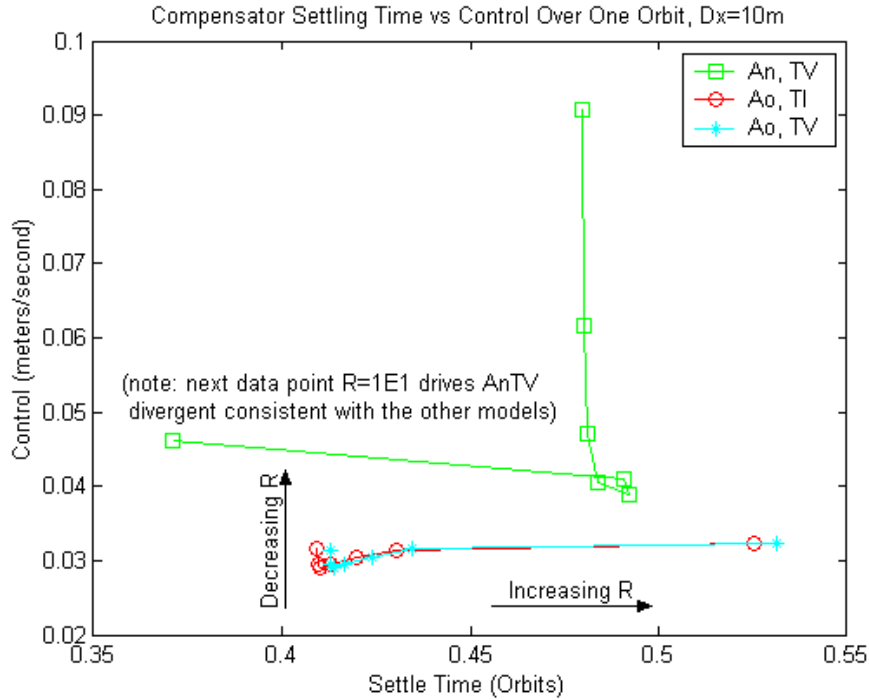
Figure 45. Compensator Settling Time vs. Control, Dx=10m

As before with the regulator, the best balance between control and settling time for the compensator was R=1E-4. For both orbital frame models, the tuning R value for best control was R=1E-4, but AnTV minimized control for R=1E-2. While all the models reduced settling time for smaller R values, for comparative purposes a single value R=1E-4 provided an acceptable compromise between minimal control and minimal settling time. Although the consistency of the time-varying and time-invariant results for the orbital frame A matrix are not the same as with the regulator, they are still pretty close. It is also a pleasant surprise to see that the compensator's control and settling time results for AoTI and AoTV deviated only slightly over the regulator results. Comparing regulator to compensator results for both AoTI and AoTV (see Table 5 below), control degraded less than one percent. Even with the handicap of noisy position data, the compensator, with its combined filter and controller, was able to control the system almost as well as an idealistic full state feedback regulator, but the RMS error suffered.

Table 5. Compensator/Regulator Comparisons for Dx=10m, R=1E-4

	Total Control (1 orbit)		Settling Time		RMS error (Dx=0m)	
	(m/sec)	% over Reg	(% orbit)	% over Reg	(meters)	% over Reg
AnTI	0.3431 *	90.4 % *	> 100 *	59.1 %	0.1770	100.0 %
AnTV	0.0471	30.3 %	48.1	-13.8	0.0175	99.6 %
AoTI	0.0291	0.7 %	41.0	1.1 %	0.0012	91.9 %
AoTV	0.0291	0.8 %	41.4	0.2 %	0.0015	95.3 %

* Diverging System
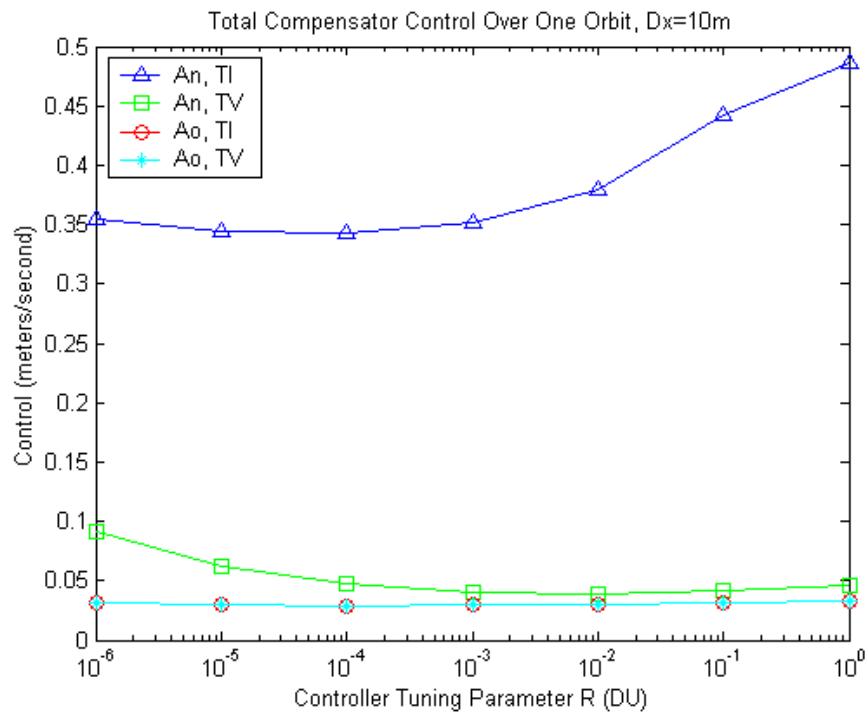
Figure 46. Compensator Control, Dx=10m, Tuning R's

The AnTI model followed the same trend as the others over the range of R values, but even the best tuning for control, R=1E-4, yielded control results which were an order of magnitude greater than those for the other scenarios. The order of magnitude difference is not surprising considering the diverging nature of the results. The trend is

important, because it shows that the model is trying to control the system, but the time-invariant model we gave it was inadequate. Since this model diverged for all tuning R values and for all compensator scenarios, its results are not included in the later sections.

Table 6. Compensator Total Control Over One Orbit, Dx = 10 m, Tuning R's

Control (m/sec)	R=1E-6	R=1E-5	R=1E-4	R=1E-3	R=1E-2	R=1E-1	R=1E0
AnTI	0.354 *	0.344 *	0.343 *	0.351 *	0.380 *	0.442 *	0.486 *
AnTV	0.0907	0.0617	0.0471	0.0406	0.0388	0.0410	0.0461
AoTI	0.0315	0.0296	0.0291	0.0294	0.0304	0.0315	0.0323
AoTV	0.0314	0.0296	0.0291	0.0295	0.0304	0.0315	0.0323

* Diverging system

Table 7. Regulator Settling Times, Dx = 10 m, Tuning R's

(% orbit)	R=1E-6	R=1E-5	R=1E-4	R=1E-3	R=1E-2	R=1E-1	R=1E0
AnTI	> 100 *	> 100 *	> 100 *	> 100 *	> 100 *	> 100 *	>100 *
AnTV	47.98	48.01	48.11	48.41	49.20	49.08	37.08
AoTI	40.92	40.95	41.03	41.29	41.98	43.06	52.56
AoTV	41.28	41.31	41.40	41.68	42.40	43.47	53.16

* Diverging system

Table 8. Compensator Average RMS Error Over One Orbit, Dx = 0 m, Tuning R's

Error (meters)	R=1E-6	R=1E-5	R=1E-4	R=1E-3	R=1E-2	R=1E-1	R=1E0
AnTI	0.179	0.179	0.177	0.171	0.148	0.071	0.098
AnTV	0.0367	0.0120	0.0175	0.0445	0.0398	0.0218	0.0354
AoTI	0.0012	0.0014	0.0012	0.0035	0.0014	0.0033	0.0024
AoTV	0.0013	0.0016	0.0015	0.0016	0.0009	0.0017	0.0010

5.1.6 Filter Tuning N1 and N2. With the controller properly tuned at R=1E-4, the next step was to tweak the filter tuning values N1 and N2. Following a similar method as with the Q and R, the N1 value was set to the expected standard deviation squared for the truth model's dynamics noise (standard deviation of 2 meters per day), and the N2 value was varied as orders of magnitude of the expected standard deviation squared for the truth model's measurement noise (standard deviation of 4 meters in the radial direction and 2 meters in the in-track and cross-track directions). Again, there was a trade-off between total control used and average steady state RMS error. Tables and figures of comparative results for various filter N2 tuning values for the favored controller tuning value R=1E-4 are listed in Appendix B. The most notable result of this tuning process was that either the control or RMS error could be improved over the nominal N2=1E0, but not both. Steady state RMS error is reduced by increasing N2, in effect, telling the filter to believe its dynamics model better than the noisy measurements. Once you have a perturbation to deal with, the control and settling time favor the smaller N2 values, placing more emphasis on the noisy measurements over the dynamics model. Each model preferred a different magnitude of N2. Although a slight amount of benefit could be gained by more rigorously tuning each filter, for comparative purposes, the filter tuning value was set to the truth model variances without increasing or decreasing the tuning value.

5.2 Initial Perturbation Dy = 10 meters

The previous section's initial perturbation of 10 meters was in the radial direction, which should be the worst direction for the models since the accuracy of GPS readings is typically halved in that direction.   If the initial perturbation was instead set in the y in-track direction, the compensators would be expected to estimate and control them better.

Figure 47. Compensator Control, Dy=10m, Tuning R's

Figure 48. Compensator Settling Times, Dy=10m, Tuning R's
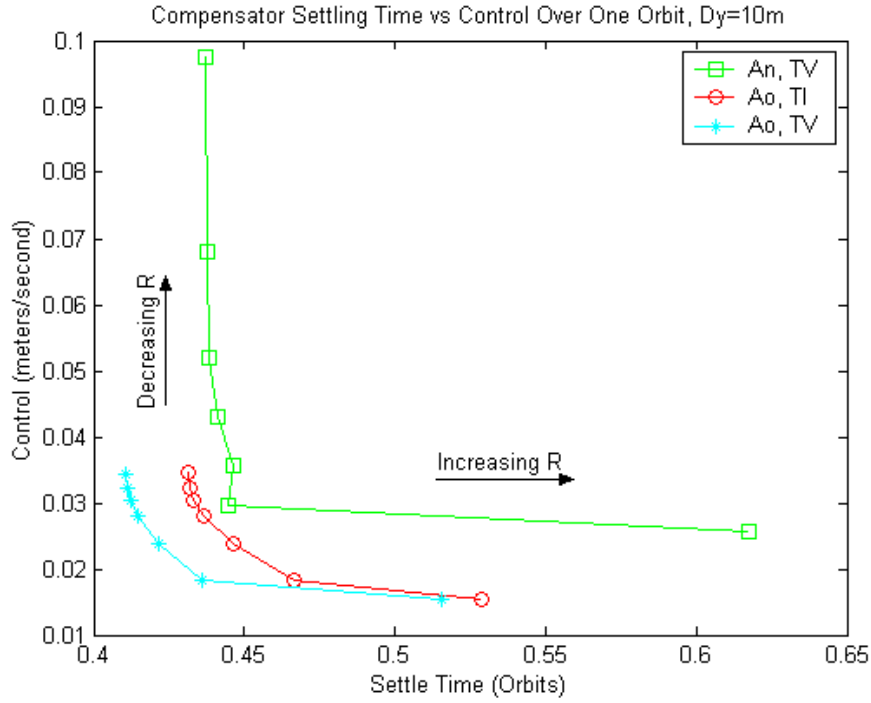
Figure 49. Compensator Settling Time vs. Control, Dy=10m, Tuning R's

The AoTI model used practically the same control as AoTV, but it allowed longer settling times for the scenario. Both of the time-varying models decreased their settling times for this model. Table 9 below compares the control results between an initial perturbation in the x radial direction versus the same initial perturbation in the y in-track direction. The unexpected increase in control for this scenario is explained as a result of cross-correlations between the various states as mentioned in the previous chapter. For realistic applications, these differences would be statistically studied and optimized in diagonal and off-diagonal weightings of filter and controller tuning matrices.

Note that RMS error were not included in this section because the steady state RMS error was defined earlier as a zero perturbation calculation. So the steady state RMS error will be the same as what was presented in Figure 43 of Section 5.1.5. The same will hold true for next two scenarios, Dz=10m and Dx=100m.

Table 9. Dy = 10 Scenario Comparisons for R=1E-4

	Total Control Over One Orbit (R=1E-4)		Settling Time (R=1E-4)	
	Control (m/sec)	% over Dx10 Scenario	(% orbit)	% over Dx10
AnTV	0.0520	10.3 %	43.85	-8.8 %
AoTI	0.0304	4.4 %	43.31	5.5 %
AoTV	0.0304	4.3 %	41.21	-0.5 %

5.3 Initial Perturbation Dz = 10 meters

For this scenario, the initial perturbation of 10 meters was set in the cross-track direction. Again, the compensators would be expected to estimate and control them better than the original initial radial 10 meter perturbation.
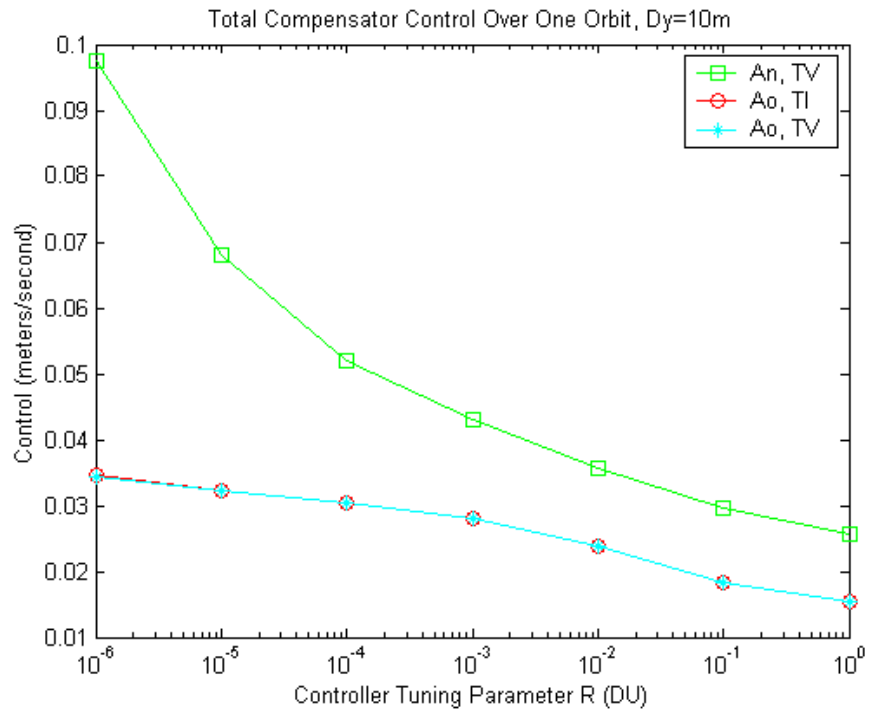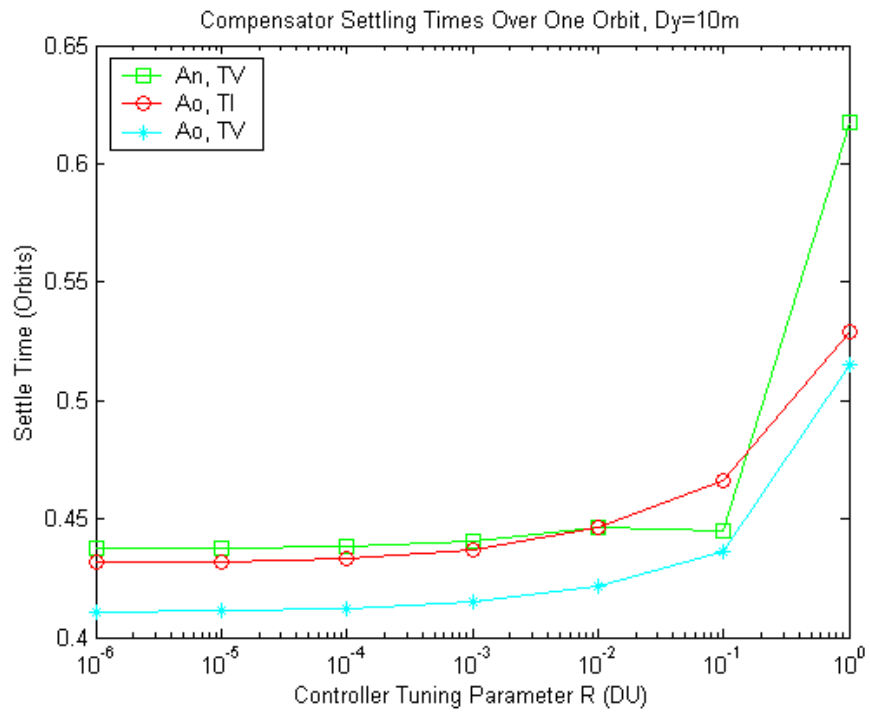

Figure 50. Compensator Control, Dz=10m, Tuning R's
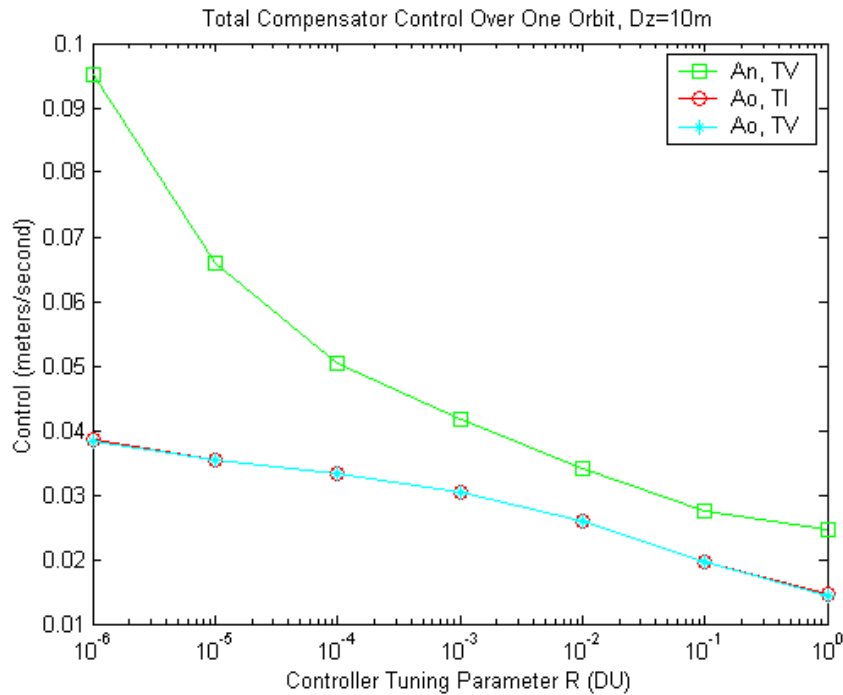
Figure 51. Compensator Settling Times, Dz=10m, Tuning R's
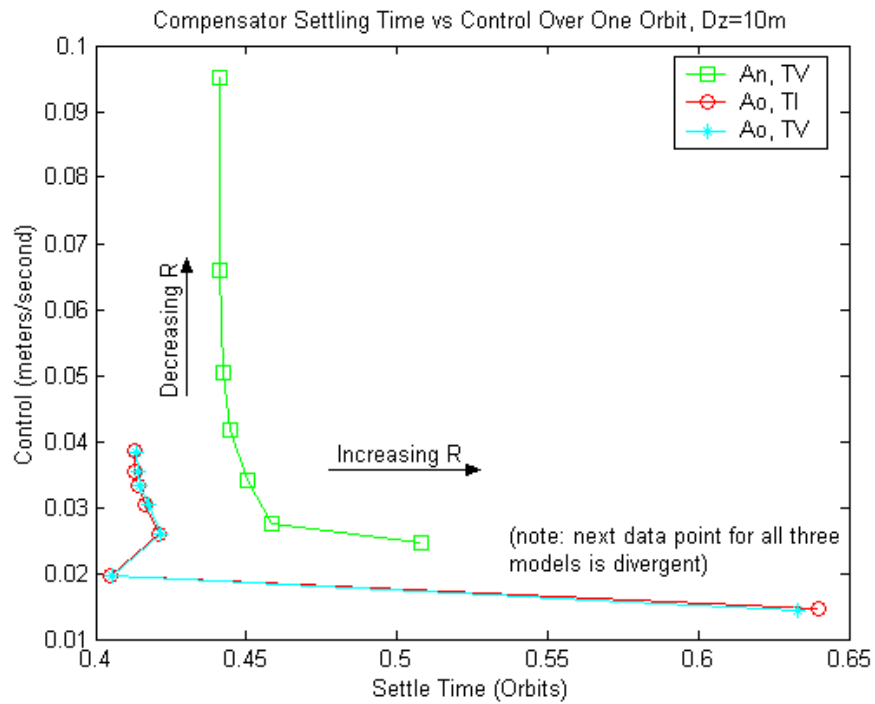
Figure 52. Compensator Settling Time vs. Control, Dz=10m, Tuning R's

Similar to the previous scenario but this time more obvious, the AoTI and AoTV had practically the same control and settling time. The nodal frame time-varying model actually improved settling time over the standard Dx = 10 m scenario. As mentioned for the previous scenario, cross-correlations between states are the culprits responsible for these results. Statistical studies of these behaviors would need to be accomplished and diagonal and off-diagonal elements of the tuning matrices would be altered.

Table 10. Dz = 10 Scenario Comparisons for R=1E-4

	Total Control Over One Orbit (R=1E-4)		Settling Time (R=1E-4)	
	Control (m/sec)	% over Dx10 Scenario	% orbit	% over Dx10
AnTV	0.0504	6.9 %	44.22	-8.1 %
AoTI	0.0333	14.4 %	41.41	0.9 %
AoTV	0.0332	14.0 %	41.48	0.2 %

5.4 Initial Perturbation Dx = 100 meters

Although the initial radial perturbation of 10 meters would be a realistic scenario for perturbations that could occur in low earth orbit, the event of increased solar activity could produce even larger perturbations. Increasing the initial radial perturbation by an order of magnitude to 100 meters would not produce results that should necessarily be designed to for stable orbit operations, but the goal for the compensators should be that such an increased perturbation does not cause them to diverge. Orbital reconfigurations as mentioned in Chapter I would require the controller to handle perturbations of this magnitude. We would expect for linear systems that a scaling of the initial perturbation should produce a comparable scaling for the control. This scenario will test the robustness of the models.
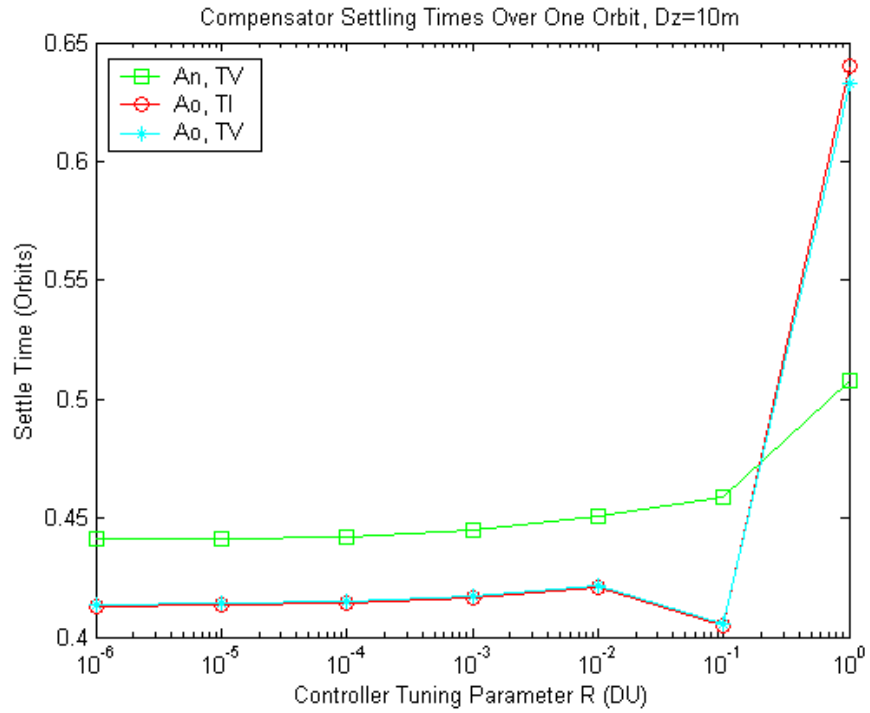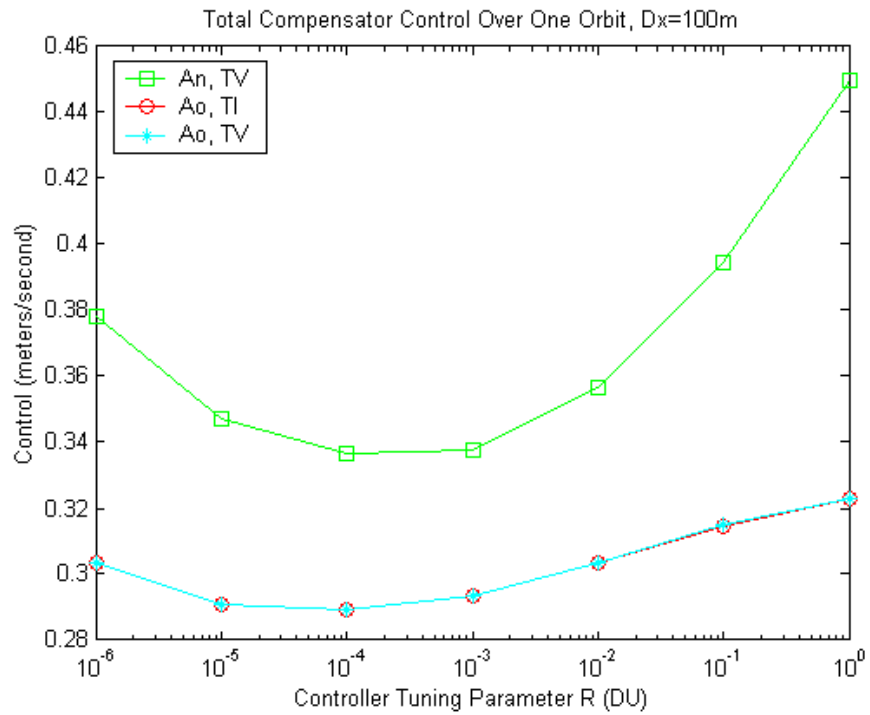
Figure 53. Compensator Control, Dx=100m, Tuning R's
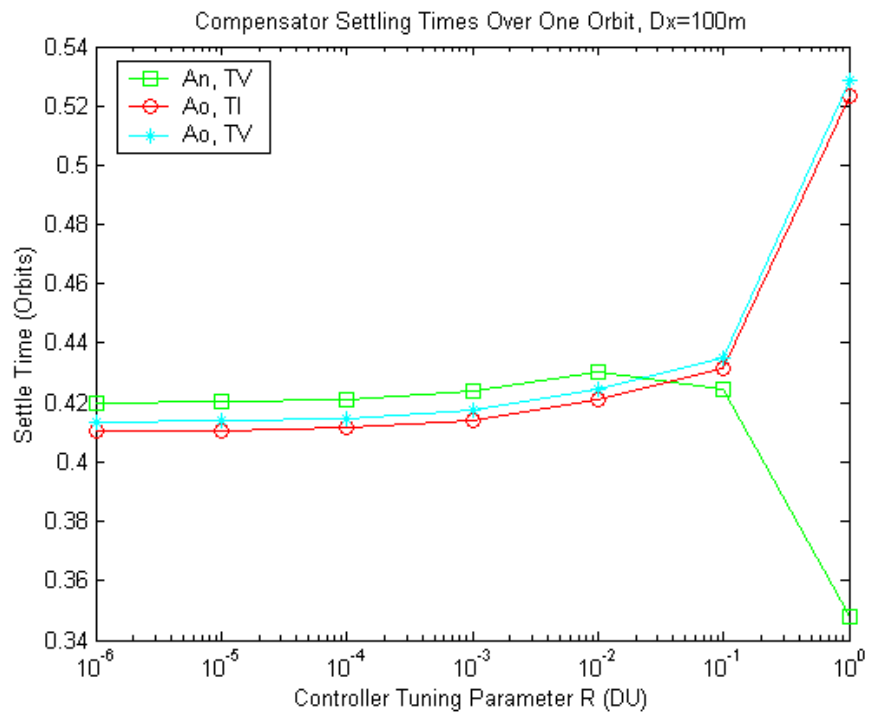
Figure 54. Compensator Settling Times, Dx=100m, Tuning R's
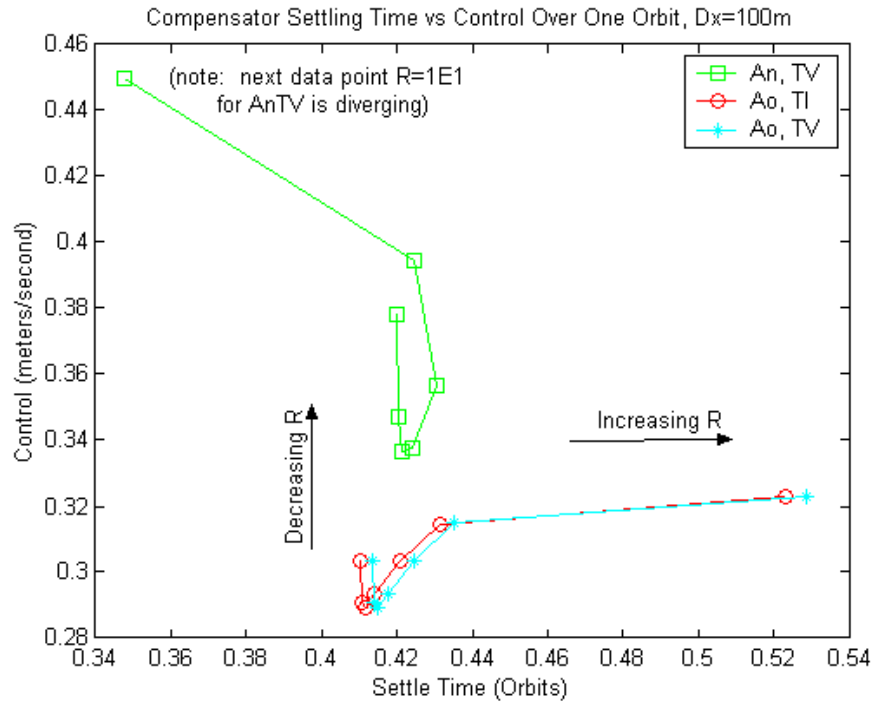
Figure 55. Compensator Settling Time vs. Control, Dx=100m, Tuning R's

While the magnitudes for control jumped an order of magnitude, the general trends seen in previous scenarios remained the same. As mentioned at the beginning of this section, for linear systems, an order of magnitude increase of initial perturbation should produce a comparable order of magnitude increase in control. Comparing this scenario's results with the standard Dx10 scenario (see Table 11 below), the increase in control for the orbital frame models over the standard is pretty close to a one-for-one, linear increase. A 10 times increase of initial perturbation yielded an 8.9 times increase in control. But the nodal frame model was not really as close. For AnTV a 10 times increase of initial perturbation yielded a 6 times increase in control. While still not besting the orbital frame models in control usage, AnTV showed that the varying time-periodic nature for its dynamics caused less deterioration than the orbital frame models for the bigger perturbation.

The Aorbital time-invariant model was the best for control, and it also provided the best settling time. Since the AoTI and AoTV models used nearly the same control, the 1% better settling time for AoTI would make it a better option.

Table 11. Dx = 100 Comparisons for R=1E-4

| | Total Control Over One Orbit (R=1E-4) | | Settling Time (R=1E-4) | |
	Control (m/sec)	% over Dx10 Scenario	(% orbit)	% over Dx10 Scenario
AnTV	0.3363	613.5 %	42.12	76.5 %
AoTI	0.2890	892.1 %	41.15	969.8 %
AoTV	0.2892	892.1 %	41.48	629.1 %

5.5 Initial Perturbation Dx = 10 meters, Increased Step Size

For the purposes of this thesis, the step size of 0.2338 seconds (same step size used in Bordner's dynamics model [4]) has been ideal for ground testing applications, but actual space computational hardware may not allow or want this measurement frequency for control burns. An order of magnitude increased step size to 2.338 seconds was tested. While sampling theory recommends a minimum sample time 2 to 3 times the frequency of data to avoid degradation of the model, this scenario tested an even larger increase. Again, this scenario was meant not to produce results that should be designed to, but more as a test to see if the higher fidelity models would diverge.

69
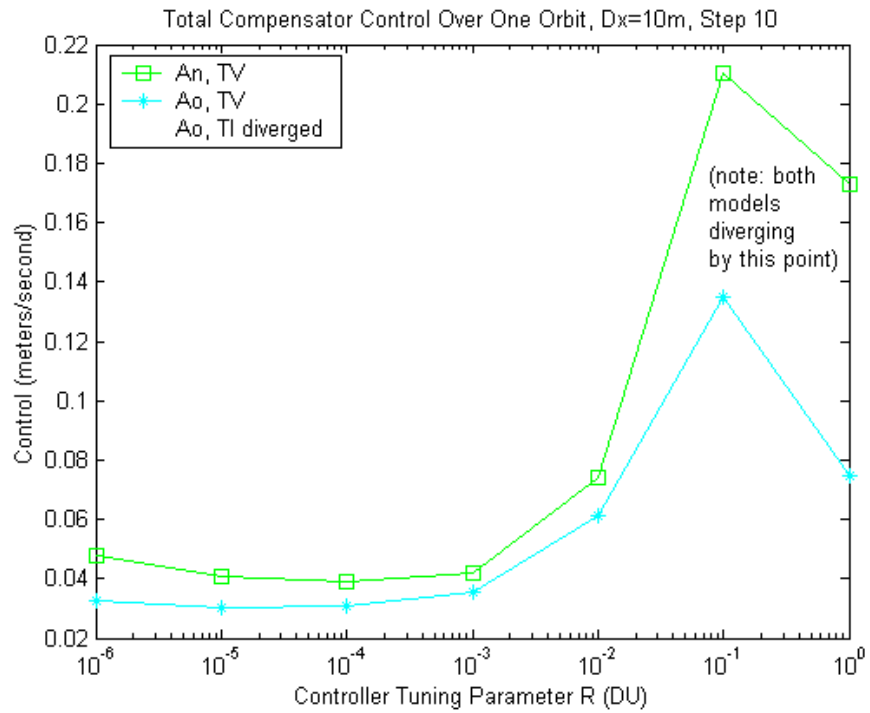
Figure 56. Compensator Control, Dx=10m, Step 10, Tuning R's
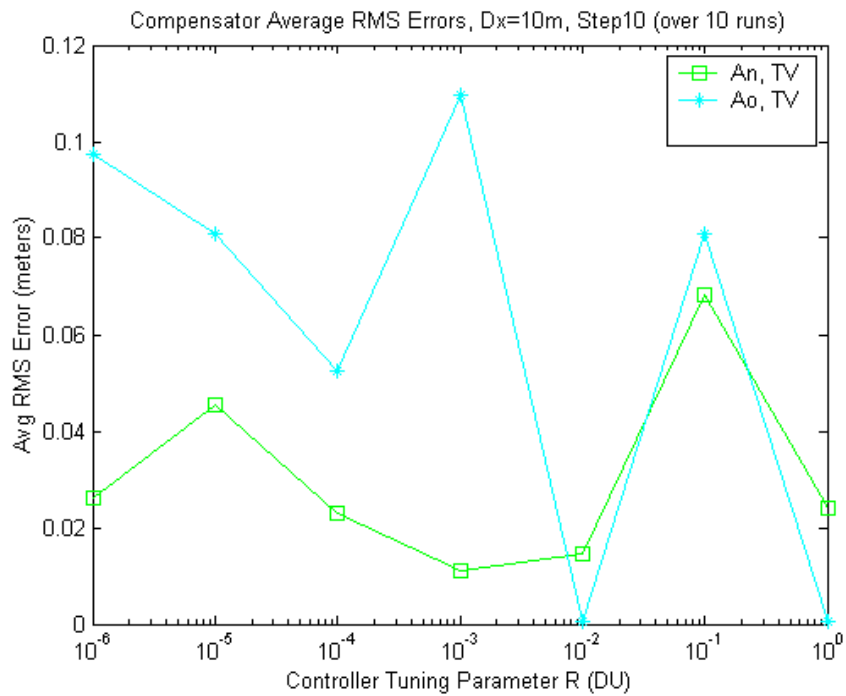
Figure 57. Compensator RMS Error, Dx=0m, Step 10 Tuning R's
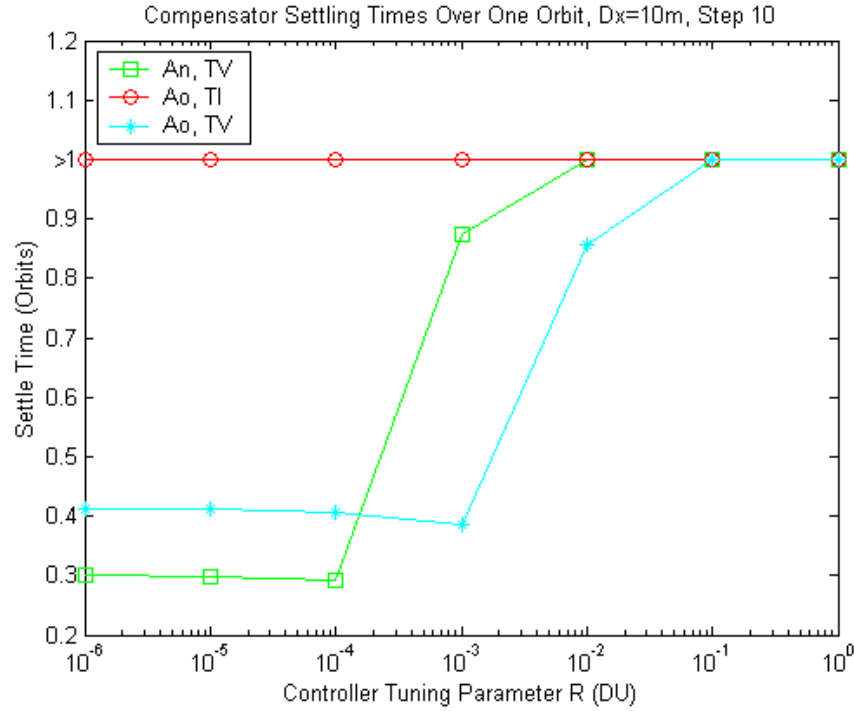
Figure 58. Compensator Settling Time, Dx=10m, Step 10, Tuning R's

Since this scenario incapacitated the time-invariant model, it compounded evidence of the robustness of both the AnTV and AoTV models. Even with its hands tied for 9/10 of the time, AoTV handled the scenario with only 6% more control than the standard resulting in only 4% better settling time. The AnTV model showed marked control usage improvement over the standard step size, and it actually improved its RMS error by over 31% over the standard. It was good to see the time-varying models handle this as well as they did, and the time-invariant model was not really expected to perform well in this type of environment because if its inherent inflexibility. Future study is recommended to look at the step size limits for each of these models. For AoTI it is recommended to evaluate step sizes between 5 times and 10 times the original step size. For both AnTV and AoTV, evaluations of increased step size above the 10 times increase are recommended.

The RMS error curves in Figure 57 show that for the steady state when there is no initial perturbation, both AoTV and AnTV struggle with the increased time step, but AnTV seems to handle it much better.

Table 12. Increased Step Size Scenario Comparisons, Dx=10m for R=1E-4

	Total Control (1 orbit)		Settling Time		RMS error (Dx=0m)	
	(m/sec)	% over Dx10	% orbit	% over Dx10	(meters)	% over Dx10
AnTV	0.0387	-17.8 %	30.31	-37.0 % *	0.0231	-31.5 %
AoTI	0.0381 *	30.8 % *	> 100 *	88.5 % *	0.0057	385 %
AoTV	0.0310	6.4 %	40.57	-3.6 %	0.0552	3430 %

* Diverging system

5.6 Initial Perturbation Dx = 10 meters, DGPS Noise

Earlier scenarios assumed truth model measurement noise consistent with absolute GPS position readings. Since the object of formation flying is to have more than one satellite flying in formation with a number of other cooperating satellites, the use of DGPS should be a viable option. According to Bordner's thesis, the DGPS signals produce accuracies on the order of centimeters [4]. For this scenario, the measurement noise in the truth model was changed from standard deviation of R_x = 4 meters to R_x = 0.04 meters and the standard deviations for R_y and R_z were similarly reduced two orders of magnitude from 2 meters to 0.02 meters. Now, the reader should be made aware that this is not a "true" DGPS scenario. This scenario utilizes advertised capabilities of DGPS to create a lower noise environment. To fully evaluate an actual DGPS scenario, Bordner's thesis provides a good description of how to evaluate this more complex problem which requires multiple cooperating satellites [4].

Figure 59. Compensator Control, DGPS Noise, Tuning R's

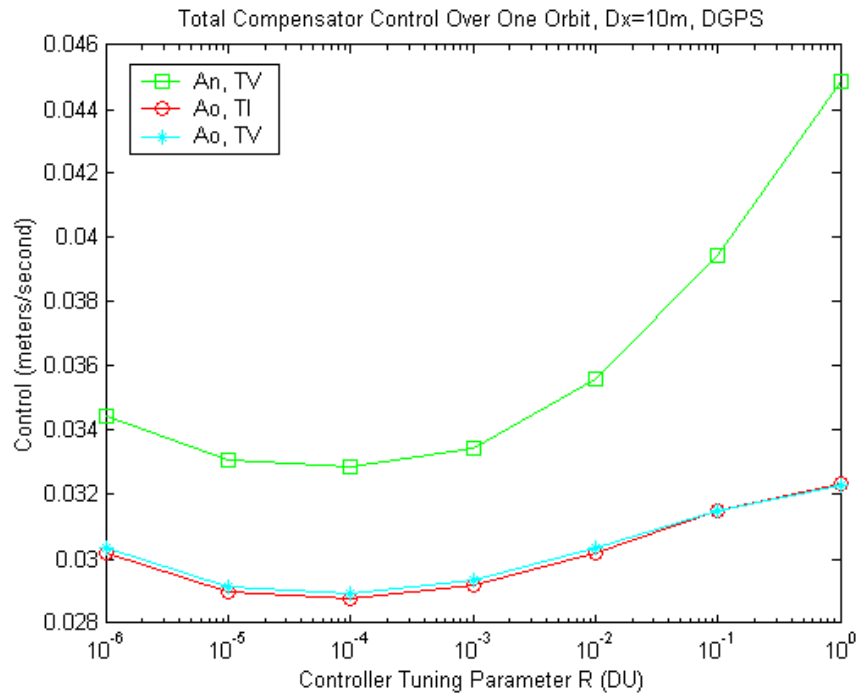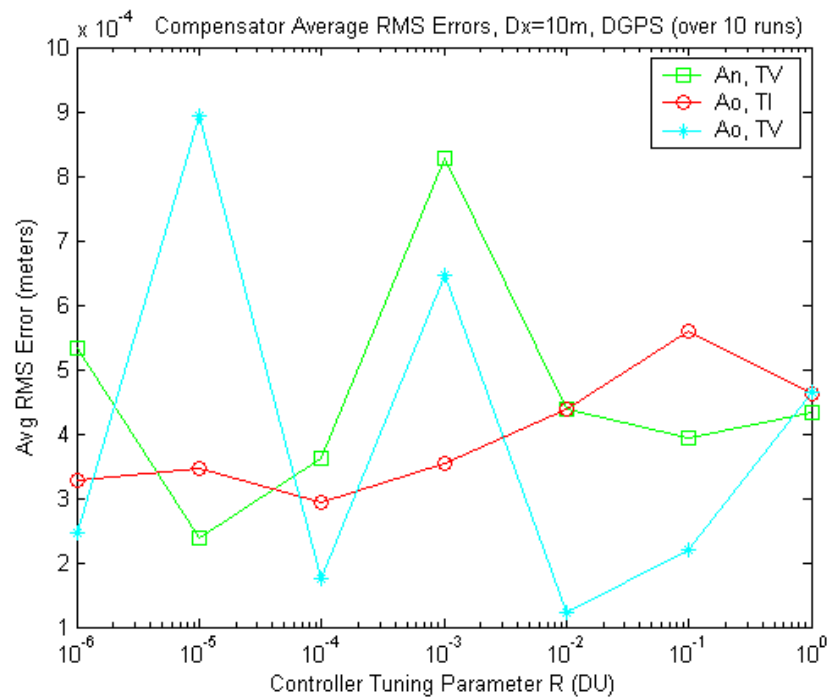

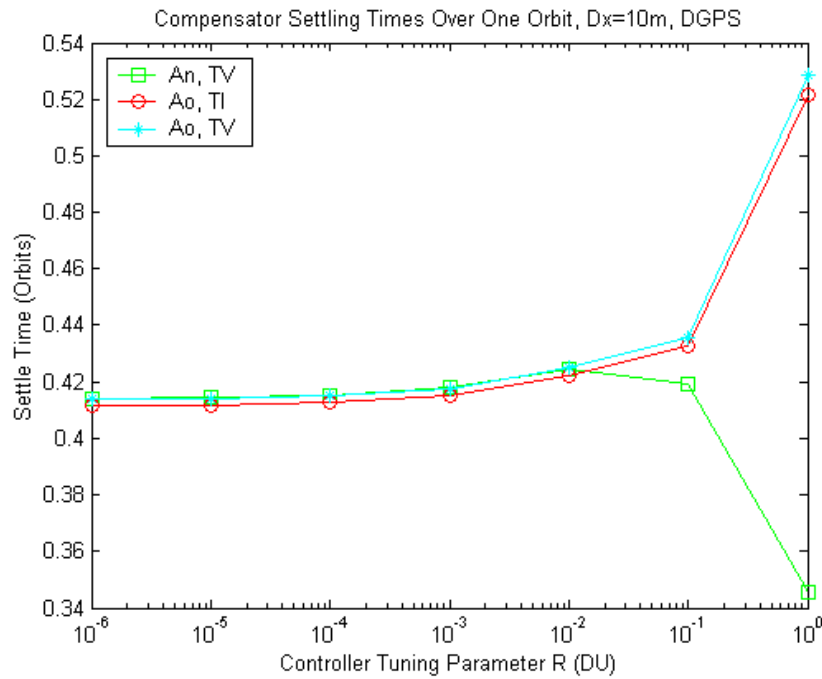Figure 60. Compensator RMS Error, DGPS Noise, Tuning R's

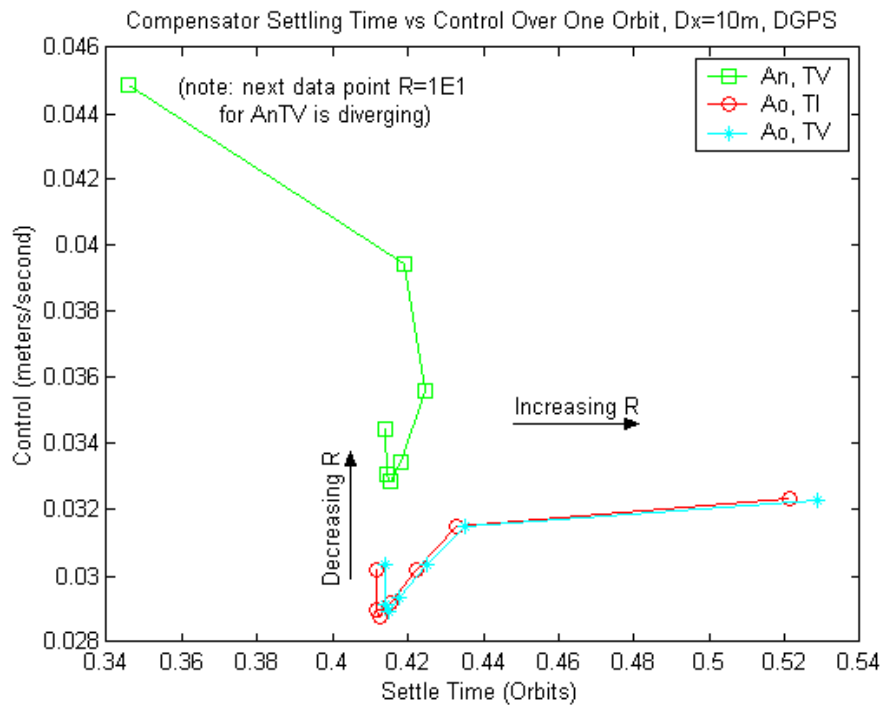Figure 61. Compensator Settling Time, DGPS Noise, Tuning R's

Figure 62. Compensator Settling Time vs Control, DGPS Noise, Tuning R's

This scenario produced results consistent with expectations. Note that RMS error results (Figure 60) were later statistically validated over 100 Monte Carlo runs. Reduced measurement noise for the system reduced both the control and RMS error for all models. But the nodal frame model showed the most improvement, 30% better control and 98% better RMS error as compared to our standard noise model. Both orbital frame models both showed modest improvement with AoTV again having the best RMS error. It is not surprising that AnTV, with its previously-shown strong correlation to noise, substantially reduced its RMS error. As mentioned at the beginning of this section, all these results are for a simple reduced-noise scenario. In order to plan for operational use of DGPS, a full-up DGPS scenario using methods described in Bordner's thesis would be needed [4].

Table 13. DGPS Noise Scenario Comparisons, Dx=10m for R=1E-4

	Total Control (1 orbit)		Settling Time		RMS error (Dx=0m)	
	(m/sec)	% over Dx10	% orbit	% over Dx10	(meters)	% over Dx10
AnTV	0.0329	-30.2 %	41.53	-13.7 %	3.6E-4	-97.9 %
AoTI	0.0288	-1.2 %	41.26	0.6 %	2.9E-4	-75.3 %
AoTV	0.0289	-0.8 %	41.50	0.2 %	1.7E-4	-88.2 %

5.7 Initial Perturbation Dx = 10 meters, Increased Noise

Earlier scenarios assumed truth model measurement noise consistent with absolute GPS position readings. Given a scenario where GPS position data was not available, the position data would need to be estimated using other methods. This scenario (not necessarily the worst case scenario) would increase the standard deviation for the measurement noise by two orders of magnitude. Similar to other scenarios covered in previous sections, this scenario would hopefully never be needed for the actual satellite missions, but it was intended as a test of the fidelity of the models.
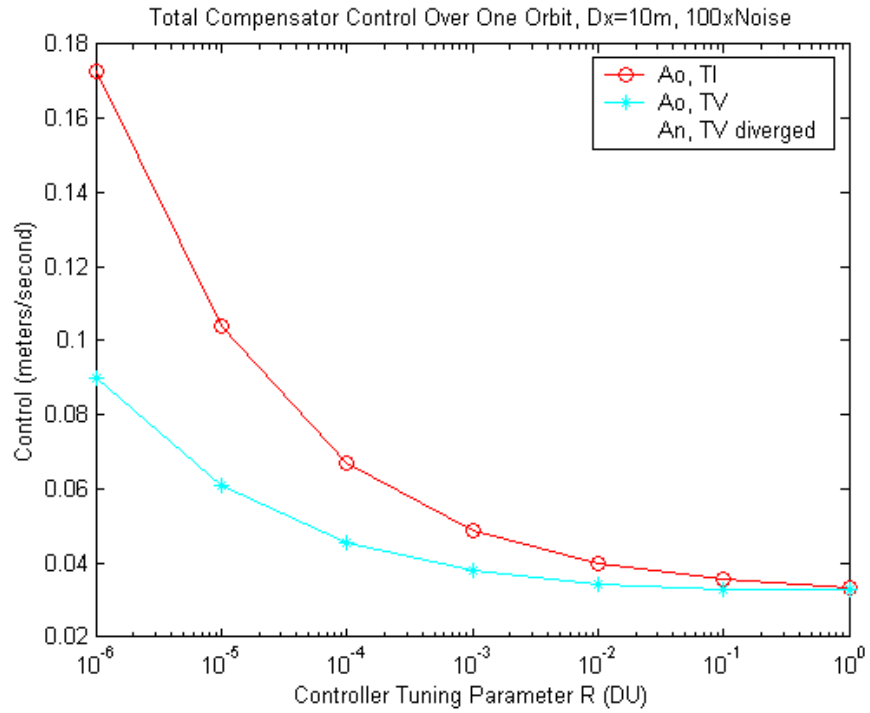
Figure 63. Compensator Control, Dx=10m, 100xNoise, Tuning R's
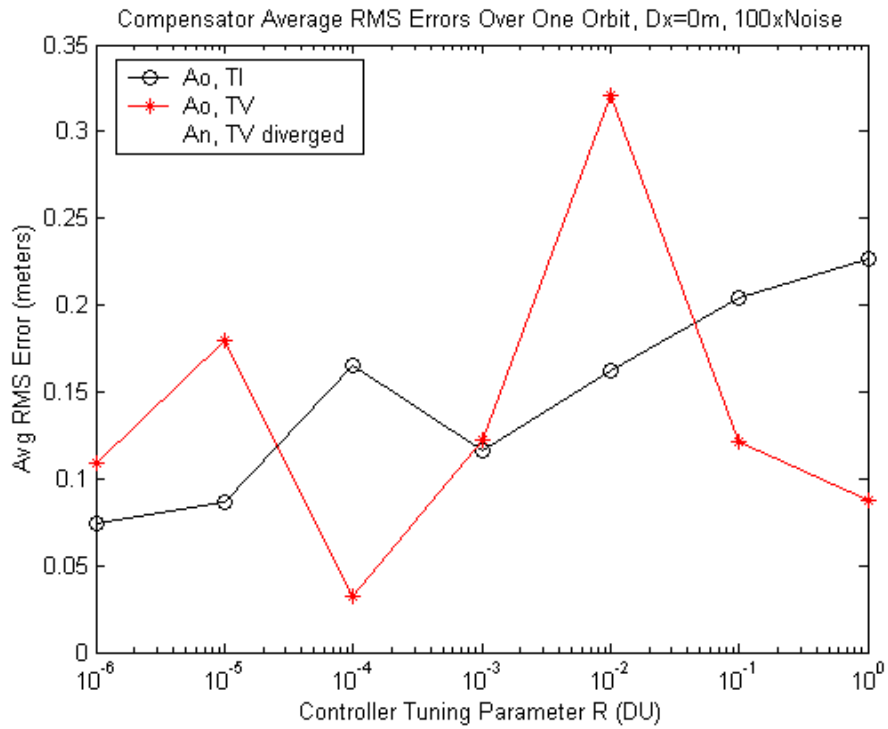

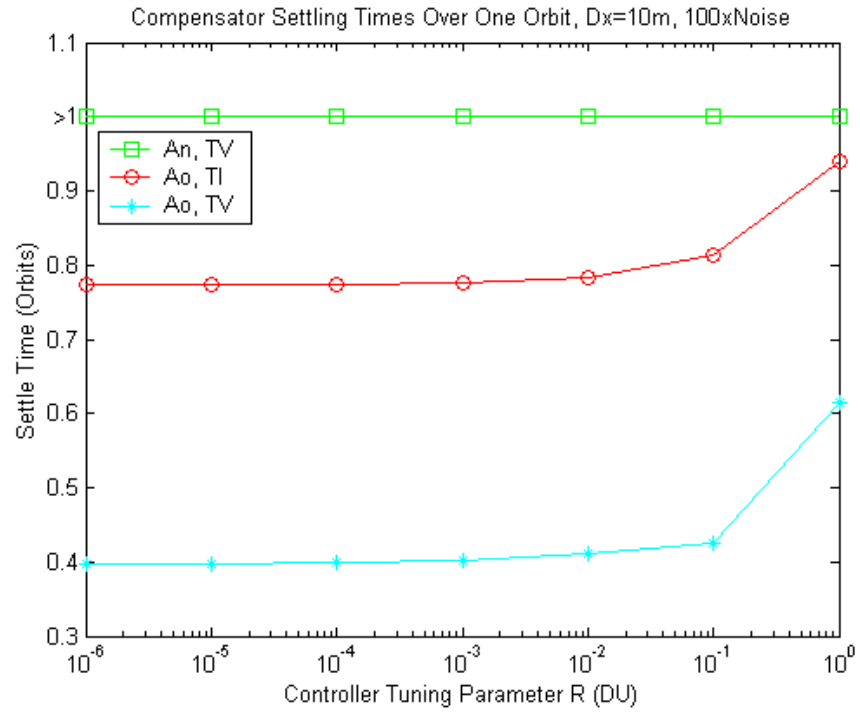Figure 64. Compensator RMS Error, Dx=10m, 100xNoise, Tuning R's

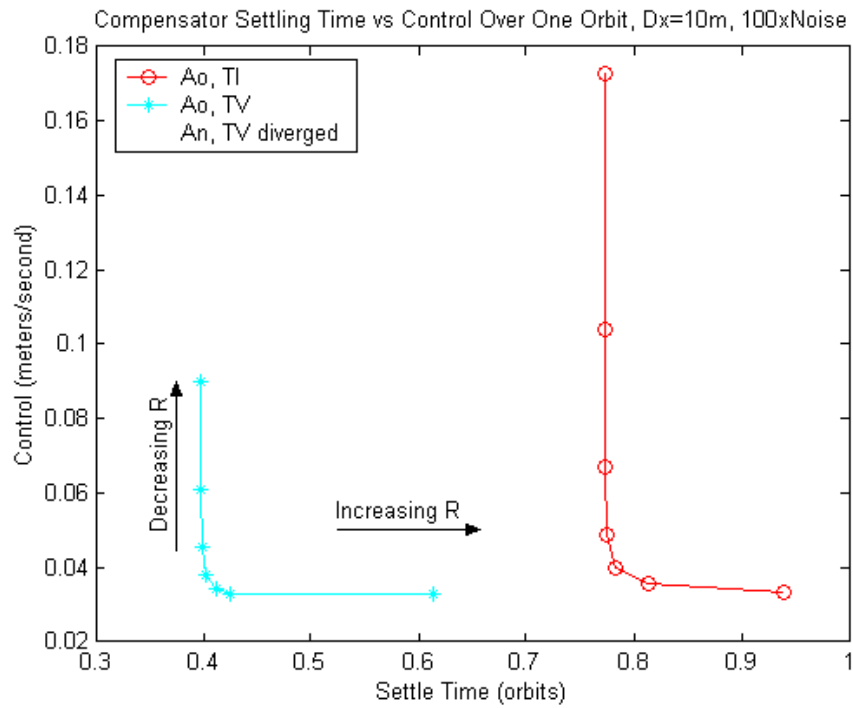Figure 65. Compensator Settling Time, Dx=10m, 100xNoise, Tuning R's

Figure 66. Compensator Settling Time vs. Control, Dx=10m, 100xNoise, Tuning R's

Although this scenario killed the nodal model, both the time-varying and time-invariant models in the orbital frame produced acceptable results with increased control and settling time as compared to the standard (see Table 14 below). This is nice to see that AoTI, with its inherent inadaptability, was able to handle this worse case scenario. AoTI's RMS error was not bad with only 4900% more error than the standard scenario, showing that, given an unperturbed system, the time-invariant model still worked well.

This scenario was disappointing for the AnTV model, because it had performed fairly well over a wide range of scenarios, but it could not adapt to the increased noise, and even the zero perturbation run diverged. These past two scenarios showed a strong correlation between measurement noise and nodal-frame model performance. While a satellite system would not necessarily need to operate over such a wide range of measurement noise magnitudes, this performance of the nodal frame model definitely ruled it out for satellites with navigation systems that produce data much worse than absolute GPS position data. On the other hand, this was good news for the AoTV because, throughout all scenarios tested, AoTV proved its fidelity and robustness in the face of many challenges. This final test for AoTV produced a better settling time than the standard and the smallest increase in RMS error compared with the other two models due to the one hundred-fold increase of noise.

Table 14. Increased Noise Scenario Comparisons, Dx=10m for R=1E-4

	Total Control (1 orbit)		Settling Time		RMS error (Dx=0m)	
	(m/sec)	% over Dx10	% orbit	% over Dx10	(meters)	% over Dx10
AnTV	2.2403 *	4653 % *	77.3 *	107.9 % *	3.4412*	19528 % *
AoTI	0.0669	129.6 %	39.9	88.5 %	0.1650	4900 %
AoTV	0.0455	56.2 %	44.6	-3.6 %	0.0324	2080 %

* Diverging system

VI. Conclusions and Recommendations

Several conclusions can be made from the data produced by this thesis. The earliest lesson learned in this thesis was: do not try to solve the periodic Riccati equation using units of the earth's radius expecting to get centimeter-level accuracy. Numeric difficulties arise from trying to invert matrices with such large (1E4) and small (1E-17) elements. Integrations and matrix inversions become questionable as to their validity. A possible unit conversion could possibly cure this ill. The limits of numerical precision for computers ranges in 1E-16 order of magnitude, so a conversion to bigger units may avoid crossing the minimum numerical precision boundary.

From the more fruitful SDRE analysis, data shows how an idealized system like the full state feedback regulator may not always predict how a system will act in a more realistic noisy environment. Even though it was not expected to perform well, the AnTI model looked perfectly adequate for the regulator. It actually produced the best RMS error compared with the other models at R=1E-4. However, once you took away its perfect state knowledge and only gave it noisy measurements, it provided inadequate control and diverged. This model diverged for all output feedback compensator scenarios including the scenario with measurement noise reduced by two orders of magnitude. Even in a low noise environment, the AnTI model diverged. These results confirm the limits of the separation principle as mentioned in Section 3.5. The robustness of the linear quadratic regulator is not guaranteed when combined with the Kalman filter to form the output feedback compensator. As mentioned in Chapters 4 and 5, this model was not expected to work well, but this is a lesson on how results from idealistic systems might lead you down the wrong path.

First noted for the full state feedback regulator, and later confirmed with most of the output feedback compensator scenarios, the AoTI and AoTV models produced very similar results for most of the scenarios. Many scenarios produced differences in both control usage and settling time of less than one percent difference between the two. This result could justify the use of linear time invariant (LTI) control whose validity was questioned in Section 3.3. Although the time-varying control produced superior results, the similarity in results combined with the computational capability required for that method may drive designers to favor the less demanding LTI method. But the failure scenarios must also be considered. The AoTI model diverged in the face of reduced step size. This failure shows the inherent inflexibility of the LTI method in compensating for big changes over large intervals. If mission requirements require control at a time step exceeding one second, this method would not be the model of choice.

The nodal frame time-periodic model AnTV showed that it was also robust. AnTV only diverged in the last scenario, but it consistently produced inferior results as compared with AoTV. The discrepancy was not always large, but AoTV consistently produced settling times and control 4-7% better for nominal scenarios. Another factor to consider is the correlation between AnTV's performance and the amount of measurement noise. In the regulator scenario where there was no measurement noise, AnTV actually produced similar RMS error to AoTV. For the DGPS scenario where noise was reduced by a factor of 100, AnTV was only 5% worse in RMS error than AoTV. Once you added more realistic noise, AnTV suffered. The one hundred-fold increase in noise totally incapacitated the AnTV model.

The correlation between the periodic nature of the nodal frame A matrix components and the response of the models to measurement noise was speculated in Section 5.1.5. Basically as the A matrix components propagated from their initial values, the measurement noise dominated the system causing the control to vary more (compare

Figure 6 from Section 2.3.1 with Figure 35 from Section 5.1.2). As time approached 20-40% of the orbit, where most of the A matrix elements periodically increased their values, the dynamics started to dominate and the system was controlled with less variability. But nearing the 50% mark of the orbit, most of the non-zero A matrix components again approached zero. These smaller dynamics components allowed the noise again to dominate giving us the noisy control.

Correlation between noise and the periodic nature of the dynamics was also seen for the orbital frame time-varying model, but it was to a much lesser degree for most scenarios. For the scenario where the measurement noise was increased by two orders of magnitude, a similar but more pronounced trend occurred for AoTV (see Figure 103 in Appendix B). Again the noise dominates the system at the initial time, 50% orbit, and final time of the orbit. Although many of the A matrix components are nearly constant, some components have the same periodic nature (just a much smaller magnitude) as we saw in the nodal frame. As these components go to zero, the noise dominates. Once they periodically increase enough (near 10% or 65% of the orbit), the dynamics overshadows the noise, and the variable control is noticeably reduced. Comparing Figure 103 with Figure 105, you can really see the difference between time-varying and time-invariant control in this more noisy environment. For AoTV the reduced noise areas of the orbit allowed the model to control in a more productive, less noisy way. This improvement gave AoTV 50% less control over the orbit than its time-invariant counterpart AoTI.

The AoTV model showed that time periodic control in the orbital frame produced not only the best results for most scenarios, but it was the only one never to diverge. AoTV produced sub-centimeter level accuracy for most scenarios using less than 3 cm/sec of control over an orbit. If the scenario was carried out longer than one orbit, to cover a whole day, the control results were still less than 3.5 cm/sec of control. If this scenario would be typical for every day of the year, the annual control usage would be

12.77 m/sec. This should translate to become an acceptable fuel budget for our microsats. These results are more impressive when you note that the noise level of the system was 30-50 times worse than our results. In other words, we gave the system noisy imperfect data, and it improved that data by 3000-5000%.

AoTV's higher fidelity would be a good selling point for the satellite formation flying mission, because the mission requires inherent flexibility. Consistent results through various scenarios would make this model the primary contender for future study. Before this model could be considered flight-worthy, though, much more tuning and Monte Carlo simulation runs would need to be run to statistically validate its capabilities. Further tuning would need to look at the position state cross-correlations witnessed by comparing the results of Dx, Dy, and Dz deflections. Diagonal and off-diagonal weightings for the filter and controller tuning matrices would have to be considered, tested, and validated. Further tests should also try other orbits with different altitudes, eccentricities, and inclinations.

This thesis focused on a single leader satellite and the control techniques in order to keep the satellite set in the desired periodic orbit. For a more populous satellite cluster, the same techniques would be repeated with new initial conditions. The initial position of the additional satellite would be chosen to provide the desired cluster configuration. As the satellite propagates through its orbit, the additional satellite is controlled to follow its own prescribed orbit relative to the leader. Cooperative techniques would need to be added to ensure the relative spacing and positioning between cluster members remains adequate for the desired mission at all times during propagation through the full orbit.

Appendix A. Linear Time Periodic Method (LTP) Troubleshooting

As mentioned in Section 3.4, the goal of the Linear Time Periodic (LTP) method was to solve the time periodic Riccati differential equation. Bittanti proposed the method followed in this thesis with many checks allowing validation of the results [3].

A.1 Symplectic Checks

Following the method detailed in Section 3.4, checks on the symplectic nature of certain steps were used to help validate or invalidate the results. The periodic Riccati equation we were trying to solve is Equation 36. The Hamiltonian for that Riccati equation is given by Equation 37 (for convenience to the reader, repeated here below)

$$H(t) = \begin{bmatrix} A(t)^T & -B(t)\cdot V1\cdot B(t)^T \\ -C(t)^T \cdot V2^{-1}\cdot C(t) & -A(t) \end{bmatrix} \tag{37}$$

consisting of matrices relating to the state-space relations in Equation 31. The first check was a symplectic check (Equation 38) of the Hamiltonian. Following the periodic nature of its elements, the Hamiltonian was also time periodic, so the check was done for all Hamiltonians over the entire orbit. All Hamiltonian checks were successful, producing zero residuals.

The next symplectic check was not successful. The Hamiltonian transition matrix $\Phi_H(t,t_o)$ (Equation 41) should follow the symplectic relationship in Equation 40. This is a critical step that leads directly to the periodic Riccati equation solution (Equation 42), so with its results invalidated, a new approach would have to be taken to solve our problem. But many possible trouble areas were tested first to see where our calculations broke down.

A.2 Integration Methods

Since the Hamiltonian was validated, it made sense to look into the integration method used to calculate $\Phi_H(t,t_o)$, which was the integration of

$$\dot{\Phi}_H(t,t_o) = H \cdot \Phi_H(t,t_o) \qquad (51)$$

As mentioned in Section 2.2.1, the system used the haming integration subroutine, an ordinary differential equations integrator using a fourth order predictor-corrector algorithm. Haming collects the last four values for the state vector and extrapolates them to predict the next value. It then corrects the extrapolated prediction to find a new value for the state vector. Alternative double precision canned integration methods in fortran's IMSL library include both a Runge-Kutta-Verner sixth-order integration routine and a Burlish-Stoer integration routine. Both of these routines refused to handle the integration of the Hamiltonian matrix, claiming the system was "too stiff". Haming proved to be the only integrator robust enough to even take on the integration.

Another method to compute $\Phi_H(t,t_o)$, using Peano-Baker series expansion [6], was the last attempt

$$\Phi_H(t,t_o) = I + \int_{t_o}^{t} H d\sigma_1 + \int_{t_o}^{t} H \cdot \int_{t_o}^{\sigma_1} H d\sigma_2 d\sigma_1 + \cdots \qquad (52)$$

Again, even for the third order expansion, the computed $\Phi_H(t,t_o)$ still failed the symplectic test in Equation 40.

Of course, the big question is why did these methods not work? The fortran routines provide a good hint by telling us the system is "too stiff". Trying to integrate a 12 x 12 dimensioned matrix with elements on the order of 1E4 and 1E-17 is a difficult task especially considering the limits of numerical precision for computers ranges around 1E-16 order of magnitude. Some elements of the Hamiltonian are already pushing the lower limits of accuracy, so the inaccurate results we received should not be too big of a surprise.

Appendix B. Selected Data Runs for Output Feedback Compensator

B.1 Filter Tuning N1 and N2

After tuning the R controller tuning values for the output feedback compensator, the next step was to tune the N2 filter tuning values. Similar to the tuning process for the controller's R tuning values, the object is to minimize both control and RMS error. Also, as before, this is a process of trade-offs. Control cost increased as settling time improved with lower orders of magnitude for N2. Steady state RMS error prefers a higher N2 value, but these higher N2's drive the system divergent when a perturbation is added. Further tuning of the N1 values (similar to the Q tuning) was not as big a factor, due to the overbearing nature of measurement noise over dynamics noise for our system. While N1 tuning values were also quickly looked at, results were similar to the N2 results, so the end result left us with our original tuning values N2=N1=1E0.
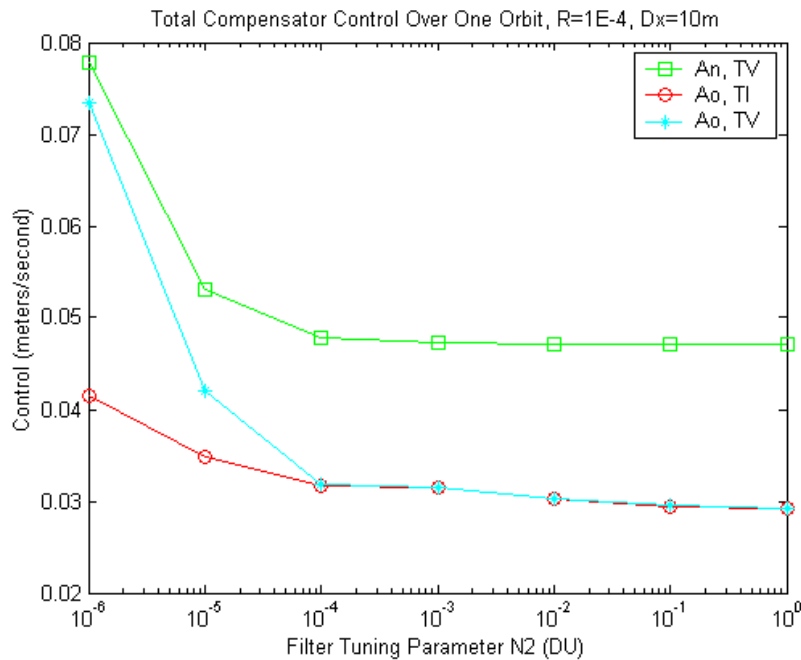

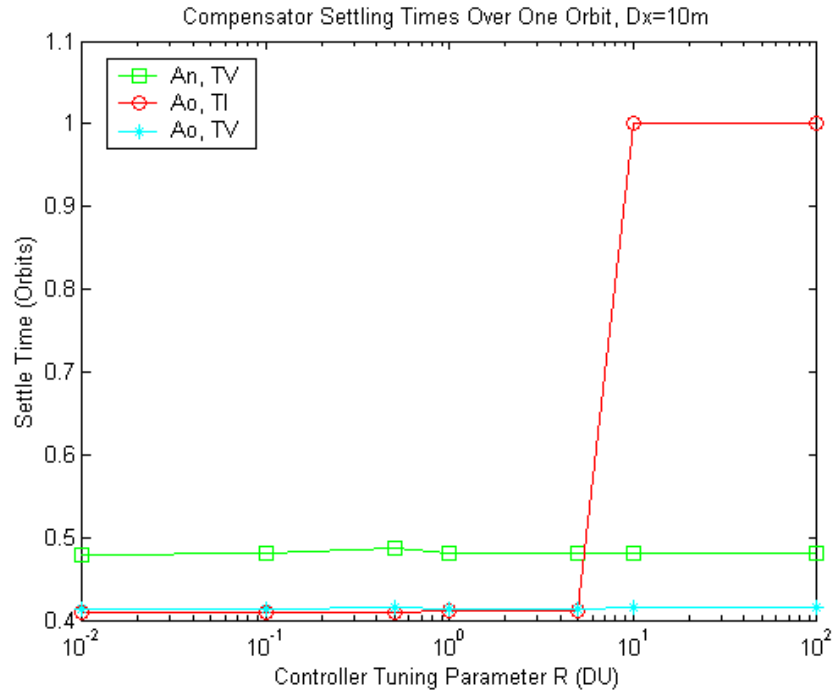Figure 67. Compensator Control, Dx=10m, Tuning N2's

Figure 68. Compensator Settling Times, Dx=10m, Tuning N2's
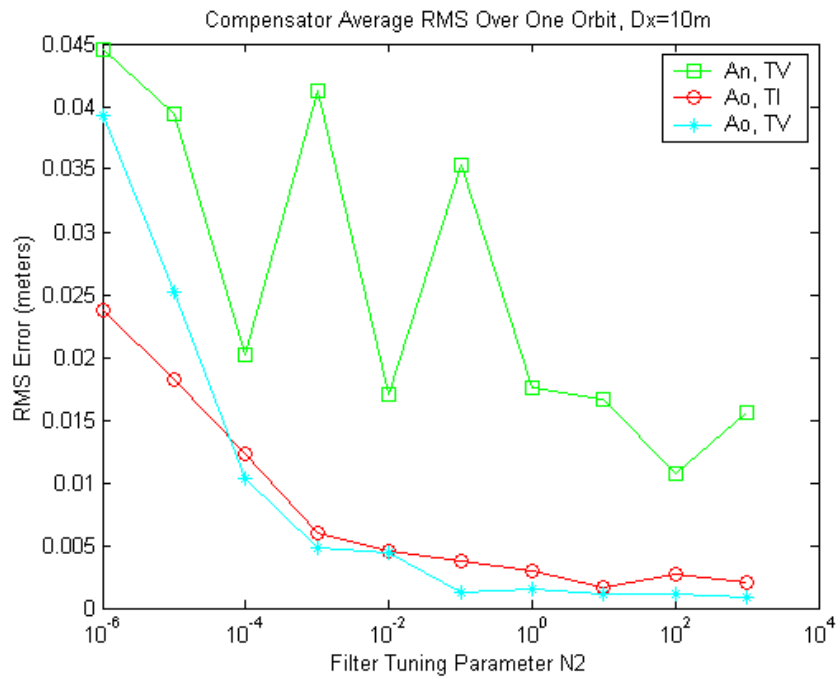

Figure 69. Compensator RMS Error, Dx=10m, Tuning N2's

Although the trends are not as easy to distinguish, each model has its own filter tuning value N2 which minimizes its control or settling time. For each orbital frame model, there was a tuning value N2=1E-2 which improved settling time over the best for our initial tuning N2=1E0. But this value was different for the nodal frame model with AnTV favoring N2=1E0. For an example of AoTI at N2=1E-2, a 0.2% smaller settling time will cost 4% more control. While control could possibly be improved with higher N2 values, there were barriers of higher N2's where the system would diverge when the filter stopped believing noisy measurement data and only believed the dynamics model.

The steady state RMS error was different than the other scenarios because it has no initial perturbation. With no perturbation, it preferred a higher N2 value basically telling the filter to ignore the measurements and only believe the dynamics model. This is a situation astrodynamicists warn about for Kalman filters [26]. For unperturbed orbital models where the dynamics are well known, Kalman filters have a tendancy to "go to sleep," reducing the weighting on the measurements to zero. This situation is acceptable in an unperturbed environment, but if the system encounters a perturbation such as the scenarios in this thesis, the system needs to use both dynamics model data and noisy measurement data. Since the initial tuning value of N2=1E0 produced an acceptable compromise between RMS error and control, it was used as the standard for comparisons in the sections that follow. The equation for calculating RMS error is given below:

$$RMSerror = \sqrt{\frac{(\hat{x} - x_{desired})^2 + (\hat{y} - y_{desired})^2 + (\hat{z} - z_{desired})^2}{3}} \tag{52}$$

Table 15. Compensator Total Control Over One Orbit, Dx=10m, Tuning N2's

(m/s)	N=1E-6	N =1E-5	N =1E-4	N =1E-3	N =1E-2	N =1E-1	N =1	N=1E1
AnTV	0.0777	0.0530	0.0478	0.0472	0.0472	0.0471	0.0471	0.0471
AoTI	0.0416	0.0348	0.0317	0.0314	0.0303	0.0295	0.0291	0.289*
AoTV	0.0734	0.0419	0.0318	0.0315	0.0303	0.0295	0.0291	0.0290

    * Diverging system

Table 16. Compensator Settling Time Over One Orbit, Dx=10m, Tuning N2's

% orbit	N=1E-6	N =1E-5	N =1E-4	N =1E-3	N =1E-2	N =1E-1	N =1	N=1E1
AnTV	46.09	45.34	46.17	47.27	47.86	48.05	41.47	48.13
AoTI	41.50	41.53	41.62	41.06	40.94	40.98	41.03	>100*
AoTV	43.06	42.55	41.79	41.33	41.27	41.34	41.40	41.47

    * Diverging system

Table 17. Compensator Average RMS Error Over One Orbit, Dx=0m, Tuning N2's

Error (m)	N=1E-6	N =1E-4	N =1E-2	N =1E-1	N =1E0	N =1E1	N =1E2
AnTV	0.0446	0.0202	0.0170	0.0353	0.0175	0.0167	0.0108
AoTI	0.0237	0.0123	0.0045	0.0038	0.0030	0.0016	0.0028
AoTV	0.0393	0.0103	0.0044	0.0012	0.0015	0.0011	0.0011

B.2 Initial Perturbation Dy = 10 m

The first scenario was for a 10 meters perturbation in the y in-track direction.

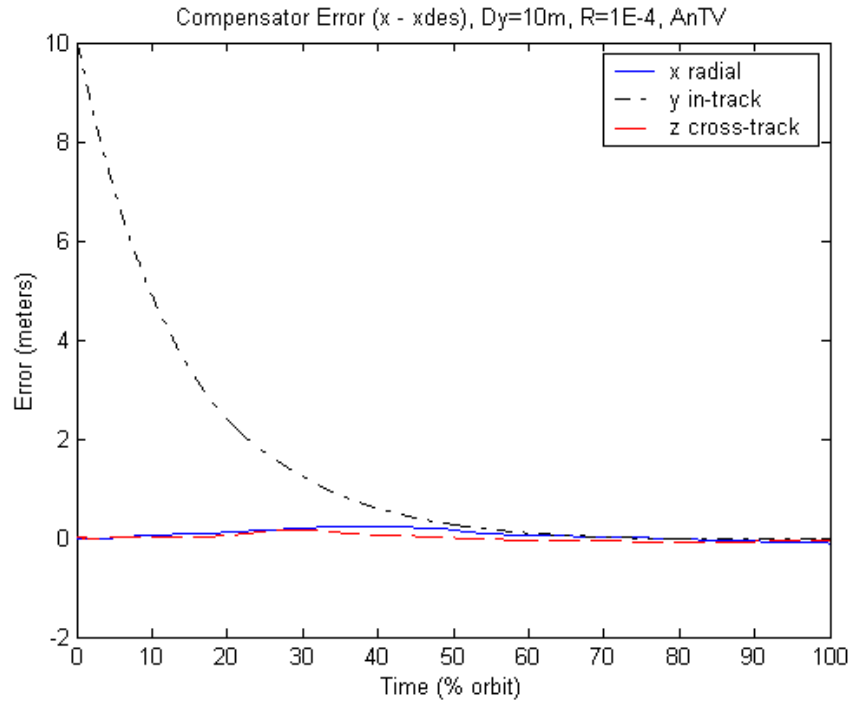### B.2.1 Time-invariant Anodal (AnTV).

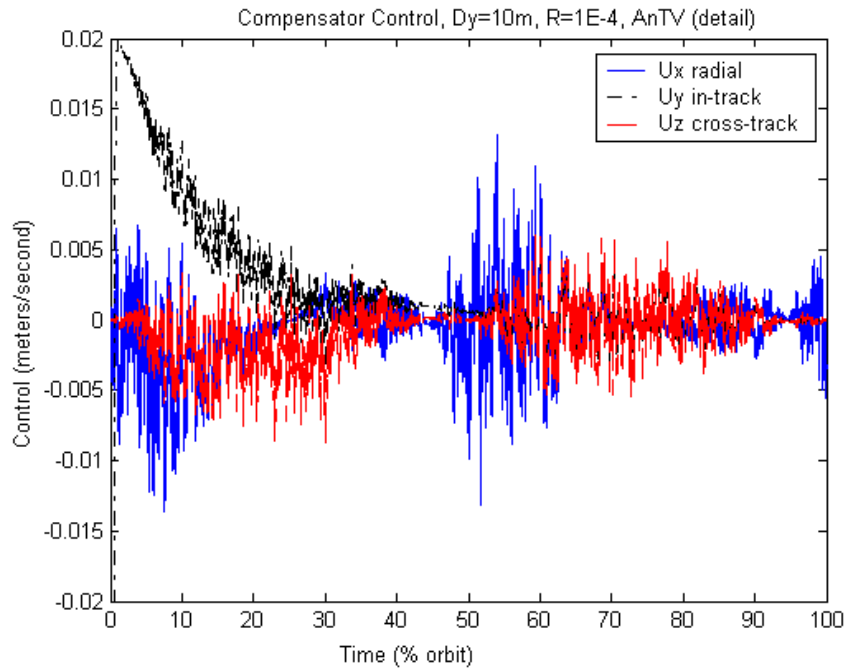Figure 70. Compensator Error for R=1E-4, Dy=10m, AnTV

Figure 71. Compensator Control for R=1E-4, Dy=10m, AnTV
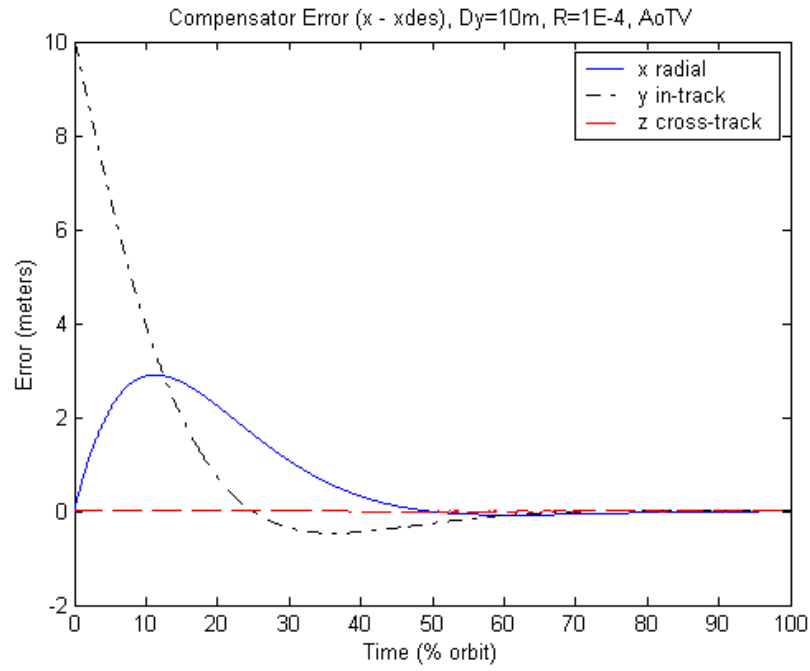
B.2.2 Time-varying Aorbital (AoTV).
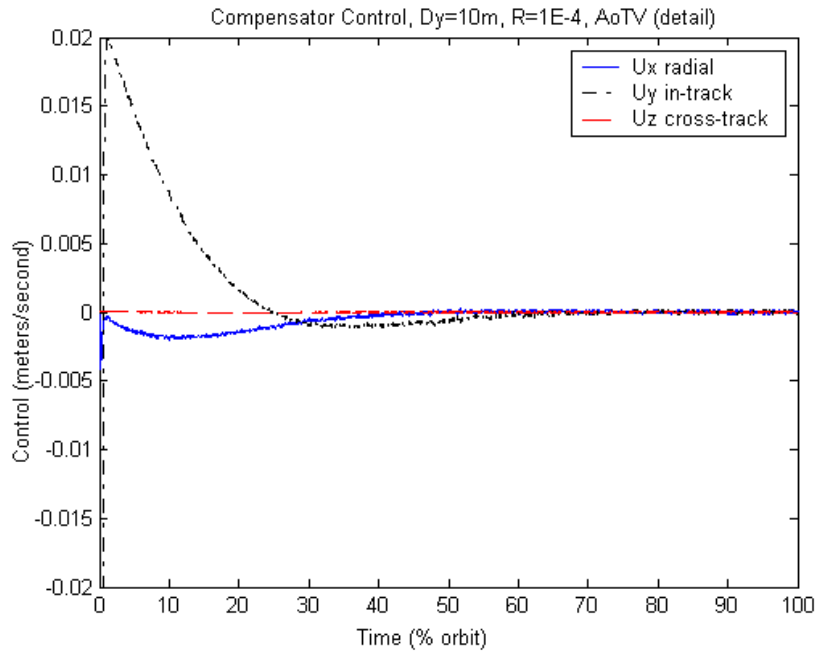

Figure 72. Compensator Error for R=1E-4, Dy=10m, AoTV

Figure 73. Compensator Error for R=1E-4, Dy=10m, AoTV
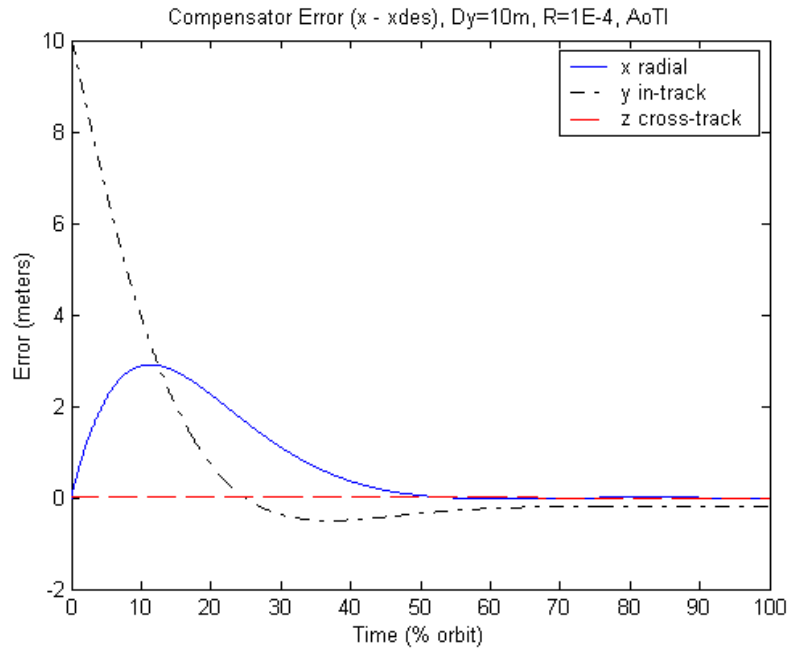
B.2.3 Time-invariant Aorbital (AoTI).
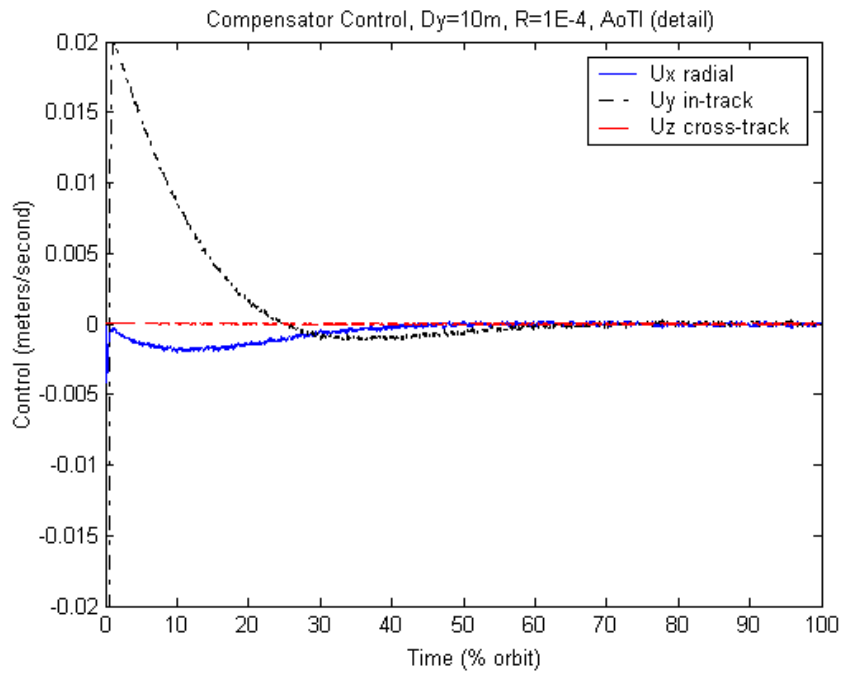

Figure 74. Compensator Error for R=1E-4, Dy=10m, AoTI

Figure 75. Compensator Control for R=1E-4, Dy=10m, AoTI

B.2.4 Model Comparisons.

Table 18. Compensator Total Control Over One Orbit, Dy=10m, Tuning R's

control (m/sec)	R=1E-6	R=1E-5	R=1E-4	R=1E-3	R=1E-2	R=1E-1	R=1E0
AnTV	0.0976	0.0680	0.0520	0.0429	0.0357	0.0295	0.0255
AoTI	0.0345	0.0322	0.0304	0.0279	0.0238	0.0184	0.0154
AoTV	0.0344	0.0321	0.0304	0.0279	0.0238	0.0182	0.0153

Table 19. Compensator Settling Times, Dy=10m, Tuning R's

(% orbit)	R=1E-6	R=1E-5	R=1E-4	R=1E-3	R=1E-2	R=1E-1	R=1E0
AnTV	43.74	43.77	43.85	44.09	44.62	44.46	61.74
AoTI	43.15	43.19	43.31	43.67	44.66	46.64	52.88
AoTV	41.09	41.12	41.21	41.48	42.18	43.62	51.53

B.3 Initial Perturbation Dz = 10 m

The next scenario was for a 10 meter perturbation in the z cross-track direction.
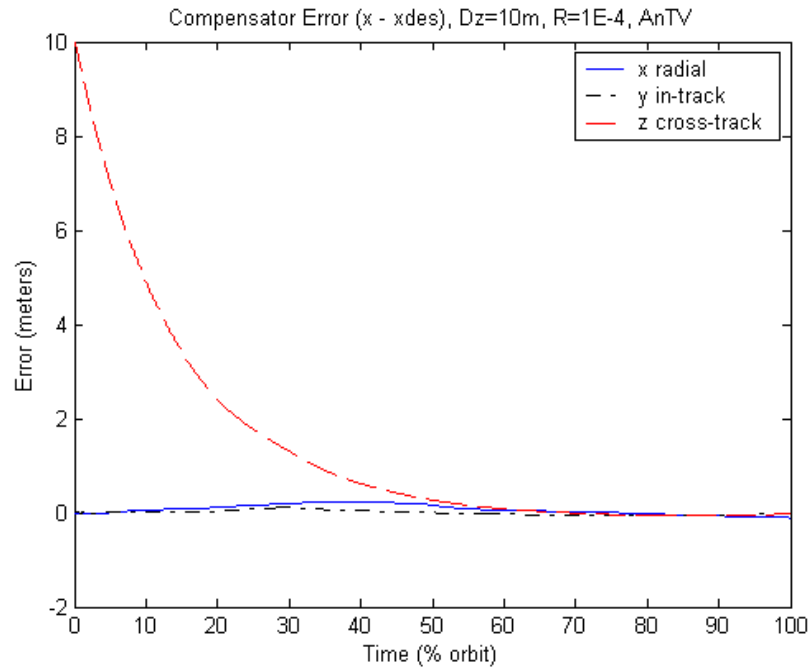
B.3.1 Time-varying Anodal (AnTV).

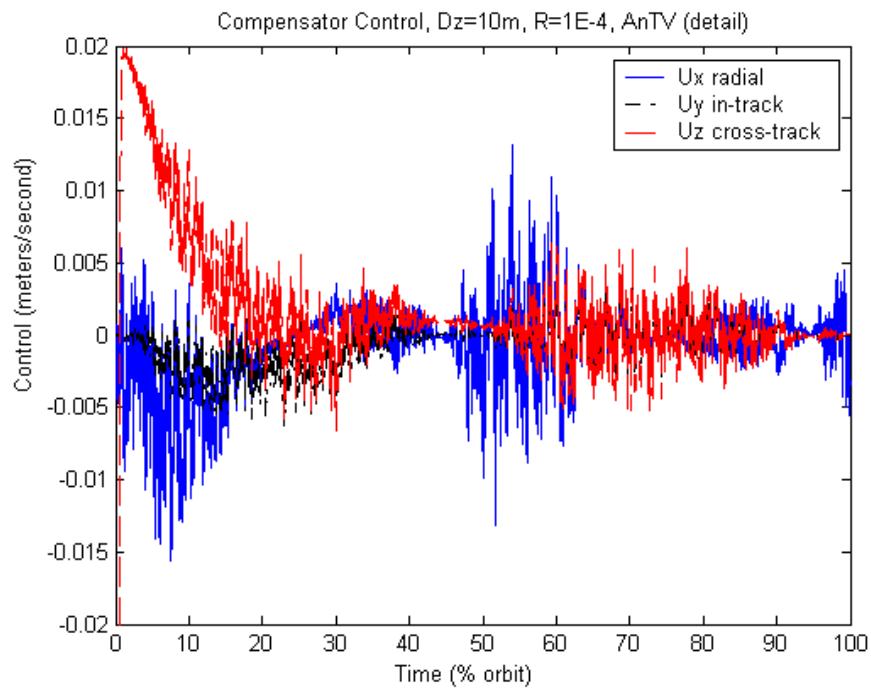Figure 76. Compensator Error for R=1E-4, Dz=10m, AnTV

Figure 77. Compensator Control for R=1E-4, Dz=10m, AnTV
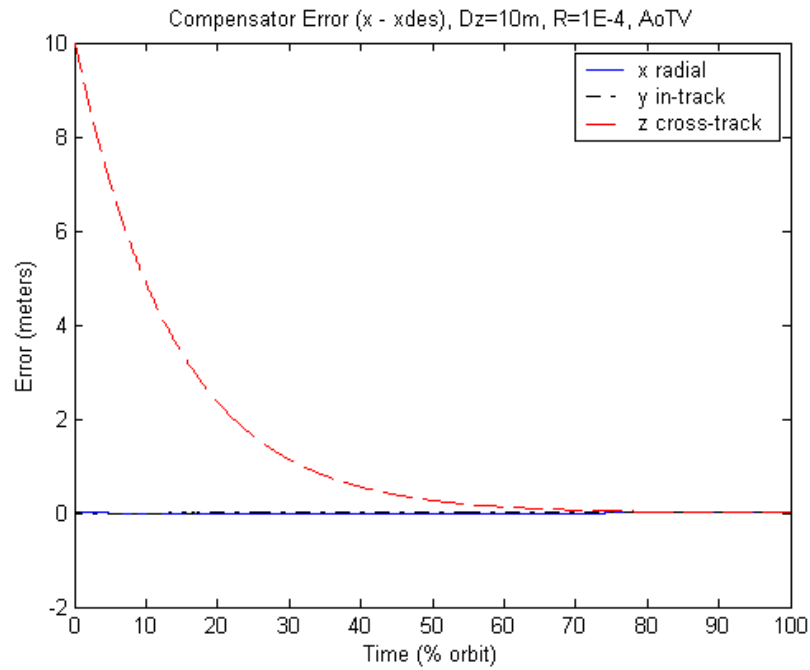
93

B.3.2 Time-varying Anodal (AoTV)

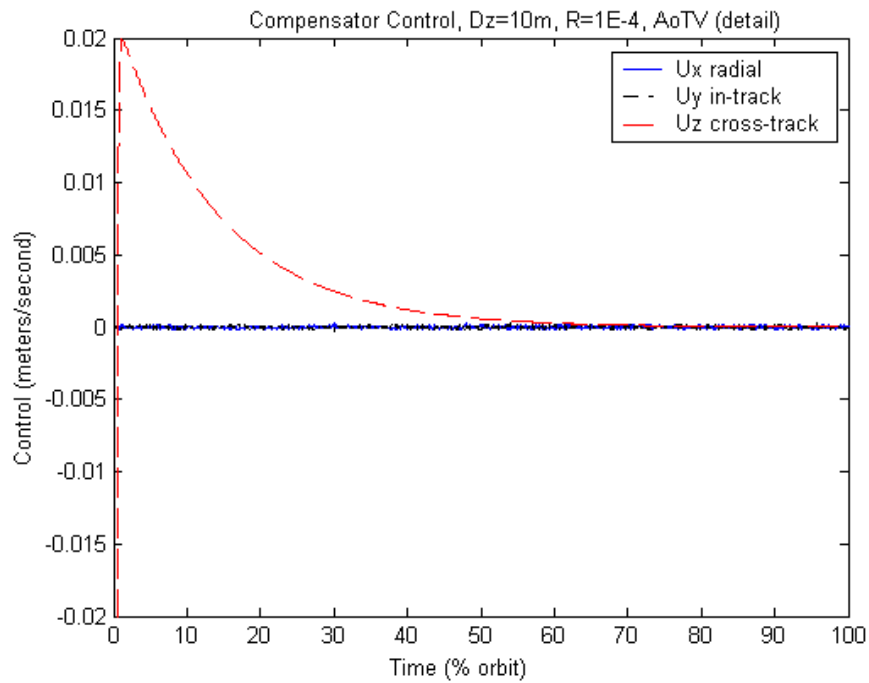

Figure 78. Compensator Error for R=1E-4, Dz=10m, AoTV

Figure 79. Compensator Control for R=1E-4, Dz=10m, AoTV
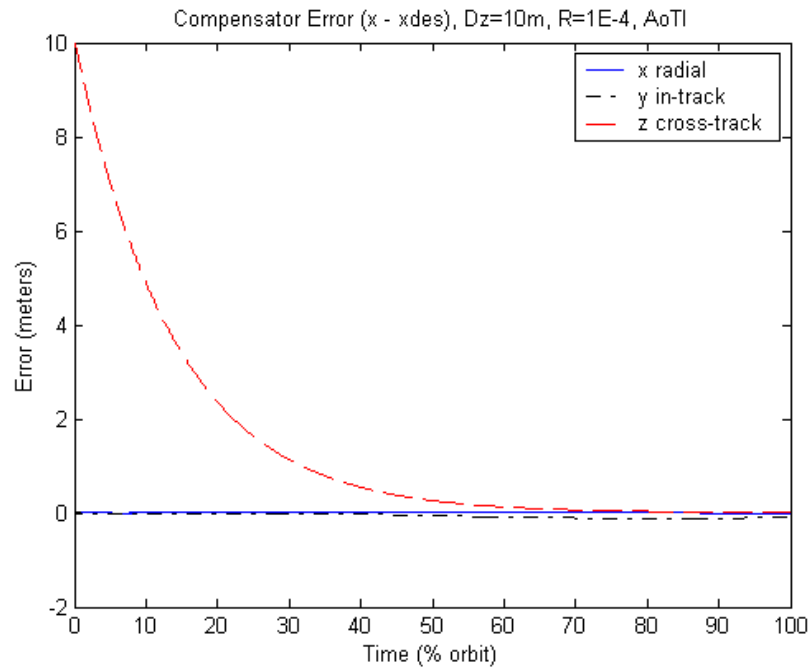
B.3.3 Time-invariant Anodal (AoTI).

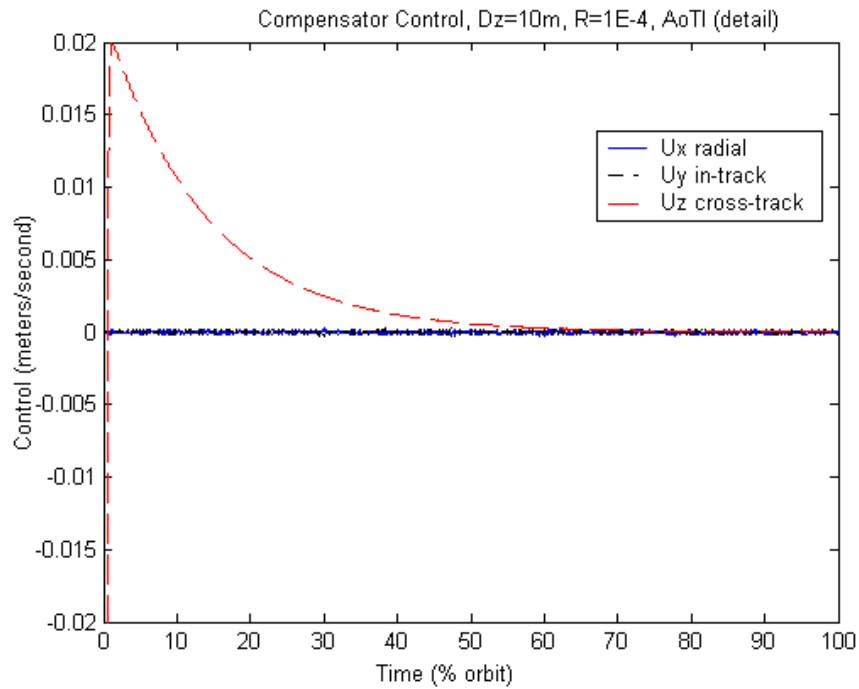Figure 80. Compensator Error for R=1E-4, Dz=10m, AoTI

Figure 81. Compensator Control for R=1E-4, Dz=10m, AoTI

B.3.4 Model Comparisons.

Table 20. Compensator Total Control Over One Orbit, Dz=10m, Tuning R's

control (m/sec)	R=1E-6	R=1E-5	R=1E-4	R=1E-3	R=1E-2	R=1E-1	R=1E0
AnTV	0.0952	0.0658	0.0504	0.0416	0.0340	0.0274	0.0245
AoTI	0.0385	0.0355	0.0333	0.0305	0.0259	0.0196	0.0145
AoTV	0.0382	0.0353	0.0332	0.0304	0.0258	0.0195	0.0144

Table 21. Compensator Settling Times, Dz=10m, Tuning R's

(% orbit)	R=1E-6	R=1E-5	R=1E-4	R=1E-3	R=1E-2	R=1E-1	R=1E0
AnTV	43.74	43.77	43.85	44.09	44.62	44.46	61.74
AoTI	41.29	41.39	41.48	41.73	42.18	40.55	63.28
AoTV	41.36	41.39	41.48	41.73	42.18	40.55	63.28

B.4 Initial Perturbation Dx = 100 m

The next scenario was for a perturbation of 100 meters in the x radial direction.
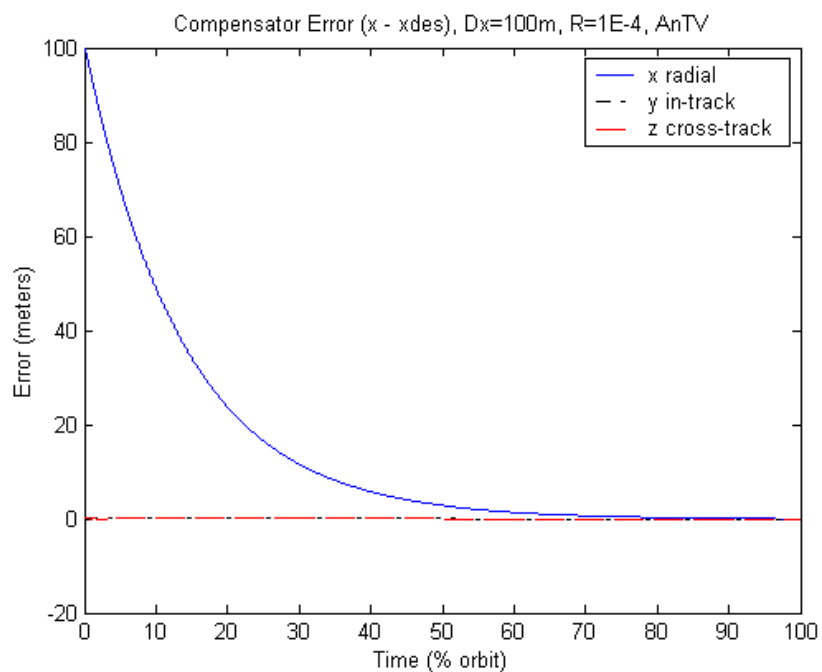
B.4.1 Time-varying Anodal (AnTV).

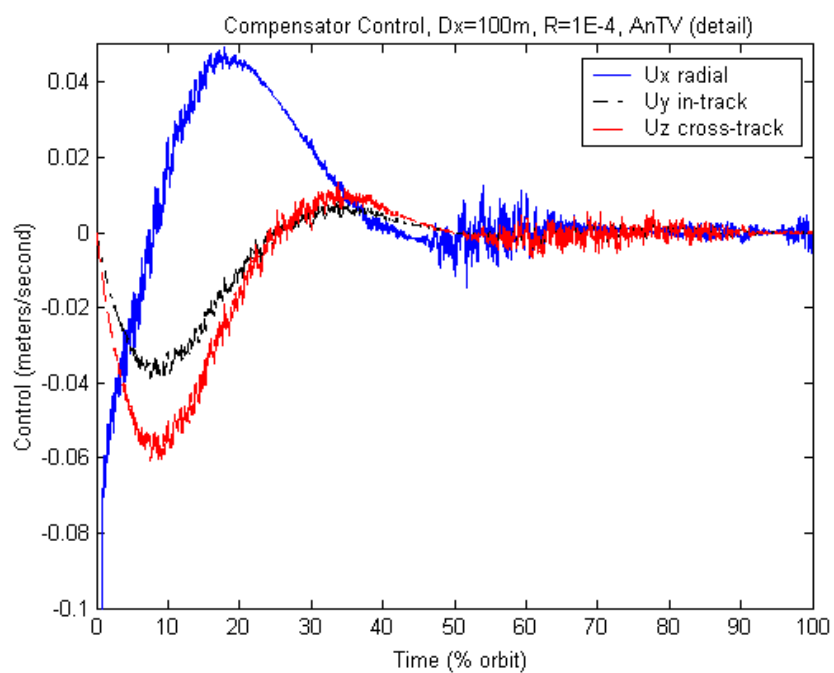Figure 82. Compensator Error for R=1E-4, Dx=100m, AnTV

Figure 83. Compensator Control for R=1E-4, Dx=100m, AnTV
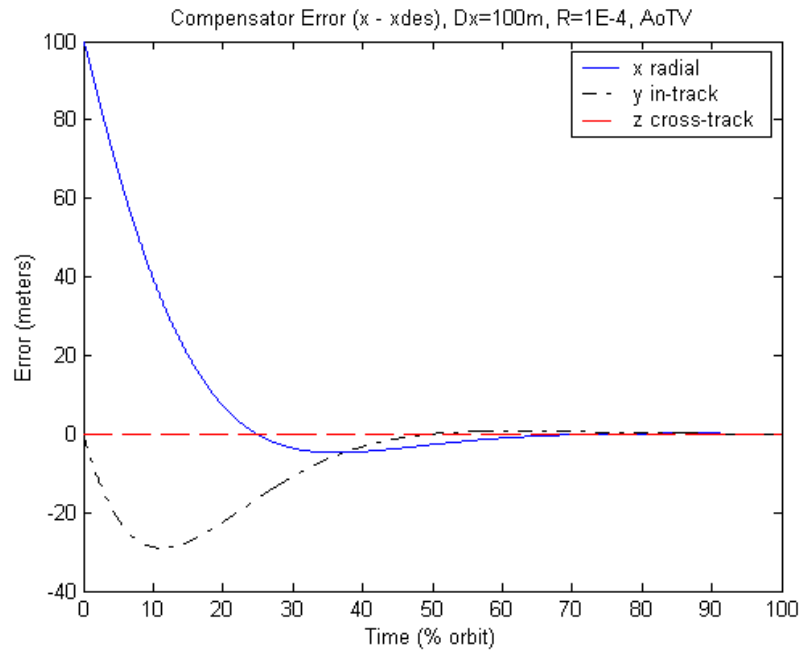
B.4.2 Time-varying Anodal (AoTV).
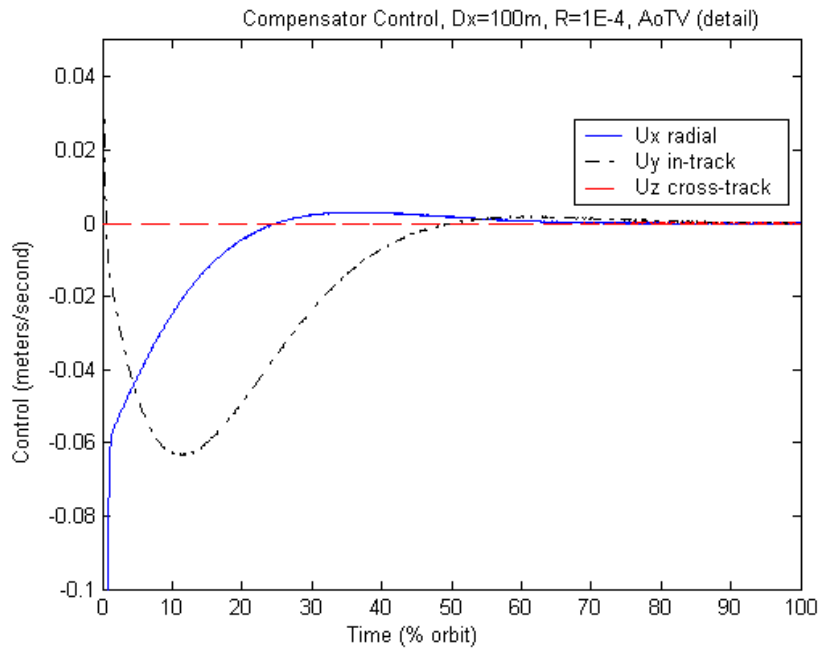

Figure 84. Compensator Error for R=1E-4, Dx=100m, AoTV

Figure 85. Compensator Control for R=1E-4, Dx=100m, AoTV
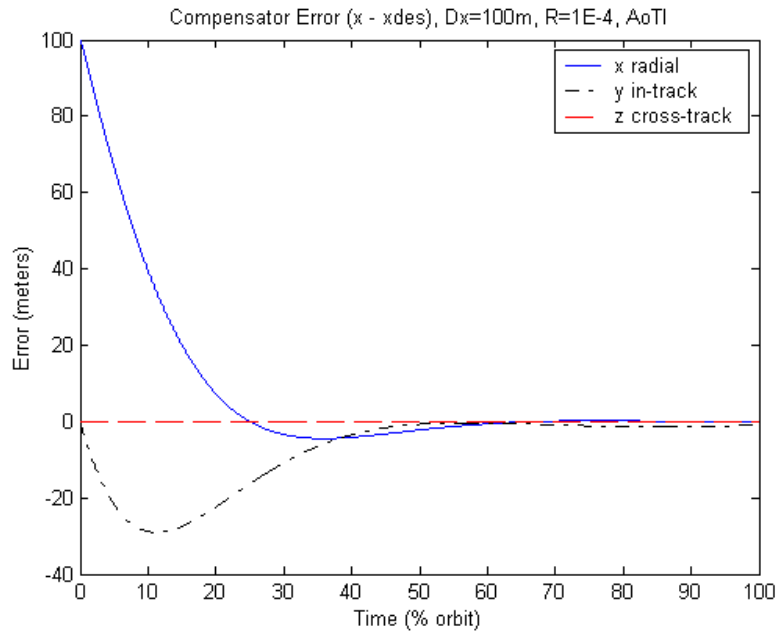
B.4.3 Time-invariant Anodal (AoTI).

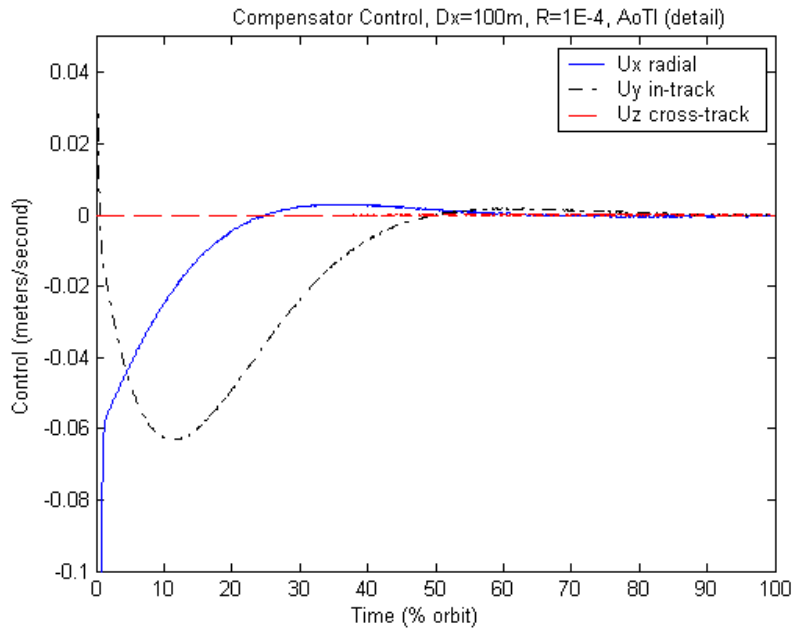Figure 86. Compensator Error for R=1E-4, Dx=100m, AoTI

Figure 87. Compensator Control for R=1E-4, Dx=100m, AoTI

B.4.4 Model Comparisons.

Table 22. Compensator Total Control Over One Orbit, Dx=100m, Tuning R's

control (m/sec)	R=1E-6	R=1E-5	R=1E-4	R=1E-3	R=1E-2	R=1E-1	R=1E0
AnTV	0.3781	0.3473	0.3363	0.3375	0.3568	0.3944	0.4497
AoTI	0.3033	0.2908	0.2890	0.2933	0.3035	0.3147	0.3230
AoTV	0.3035	0.2910	0.2892	0.2935	0.3036	0.3148	0.3229

Table 23. Compensator Settling Times, Dx=100m, Tuning R's

(% orbit)	R=1E-6	R=1E-5	R=1E-4	R=1E-3	R=1E-2	R=1E-1	R=1E0
AnTV	42.00	42.03	42.12	42.39	43.04	42.46	34.76
AoTI	41.04	41.06	41.15	41.41	42.08	43.15	52.32
AoTV	41.36	41.39	41.48	41.76	42.47	43.52	52.88

B.5 Initial Perturbation Dx = 10 m, Increased Step Size

The next scenario tested was for an order of magnitude increase in step size with the original initial perturbation of 10 meters in the x radial direction. The step size was increased from 0.2338 seconds to 2.338 seconds.

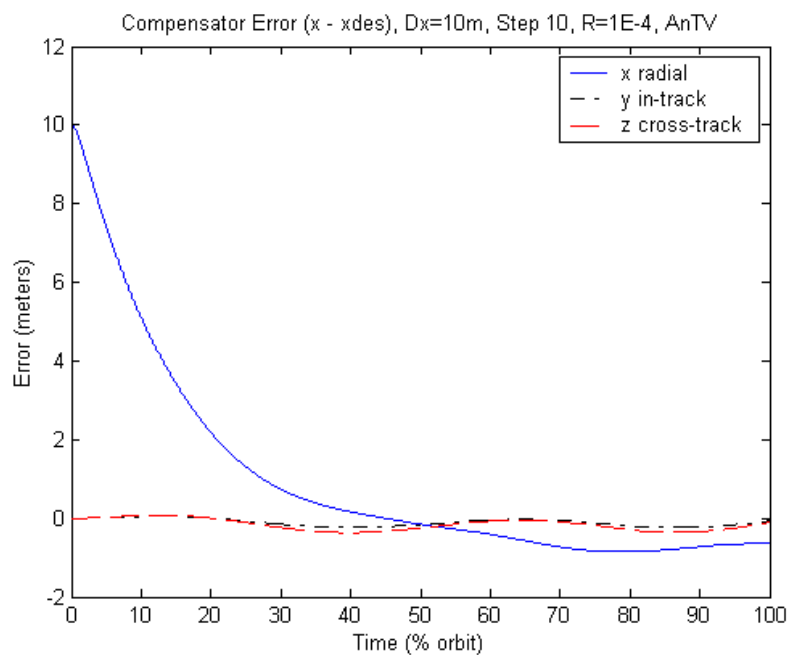### B.5.1 Time-varying Anodal (AnTV).

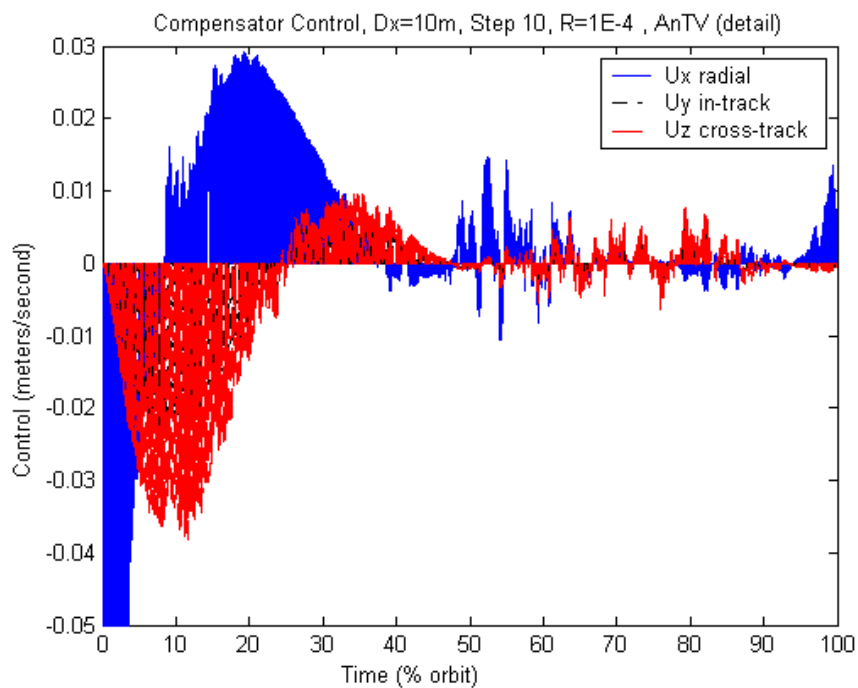Figure 88. Compensator Error for R=1E-4, Dx=10m, Step 10, AnTV

Figure 89. Compensator Control for R=1E-4, Dx=10m, Step 10, AnTV

B.5.2 Time-varying Anodal (AoTV).

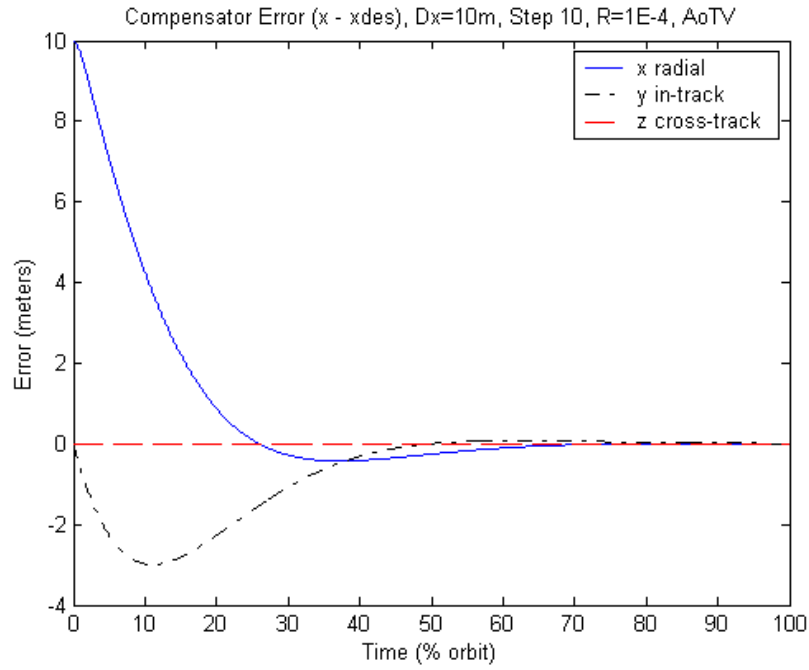
Figure 90. Compensator Error for R=1E-4, Dx=10m, Step 10, AoTV
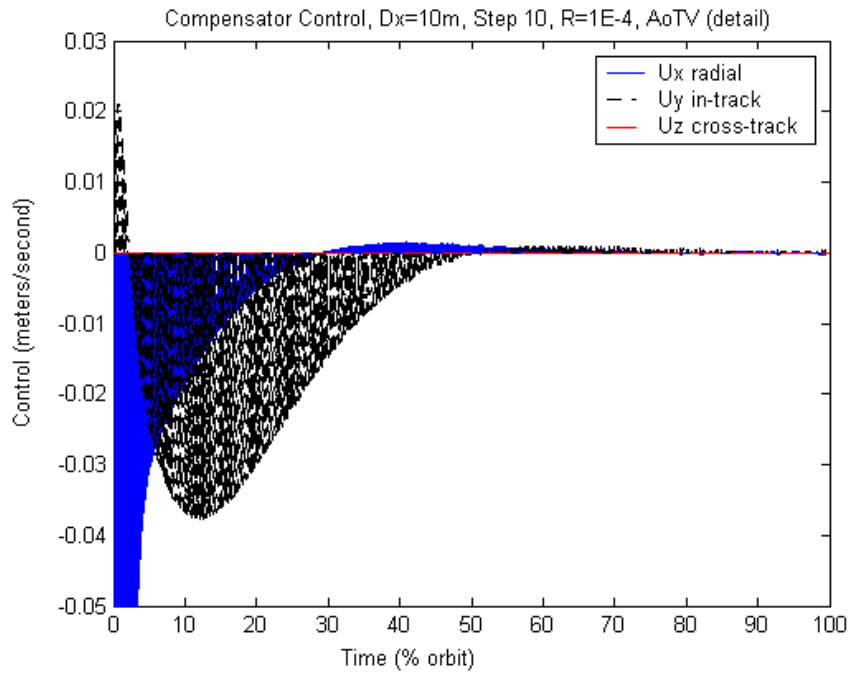

Figure 91. Compensator Control for R=1E-4, Dx=10m, Step 10, AoTV
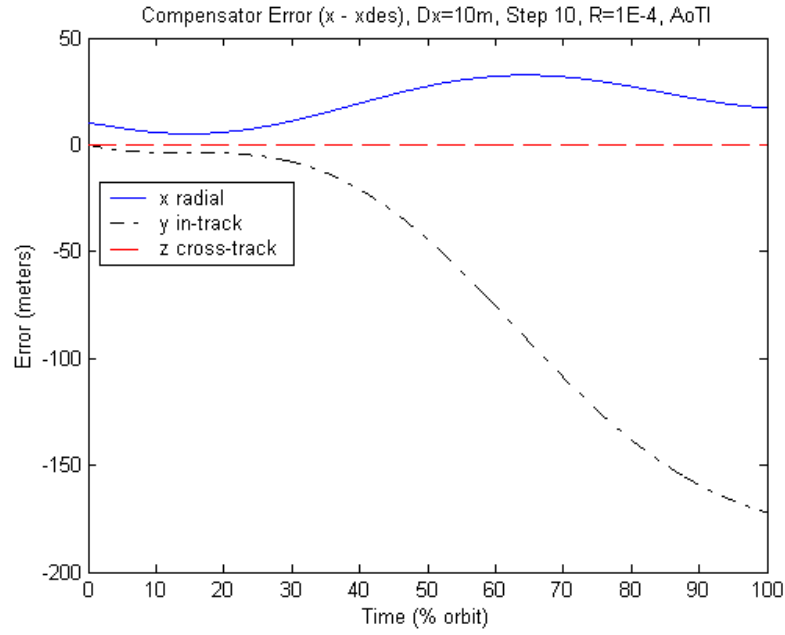
B.5.3 Time-invariant Anodal (AoTI).

Figure 92. Compensator Error for R=1E-4, Dx=10m, Step 10, AoTI
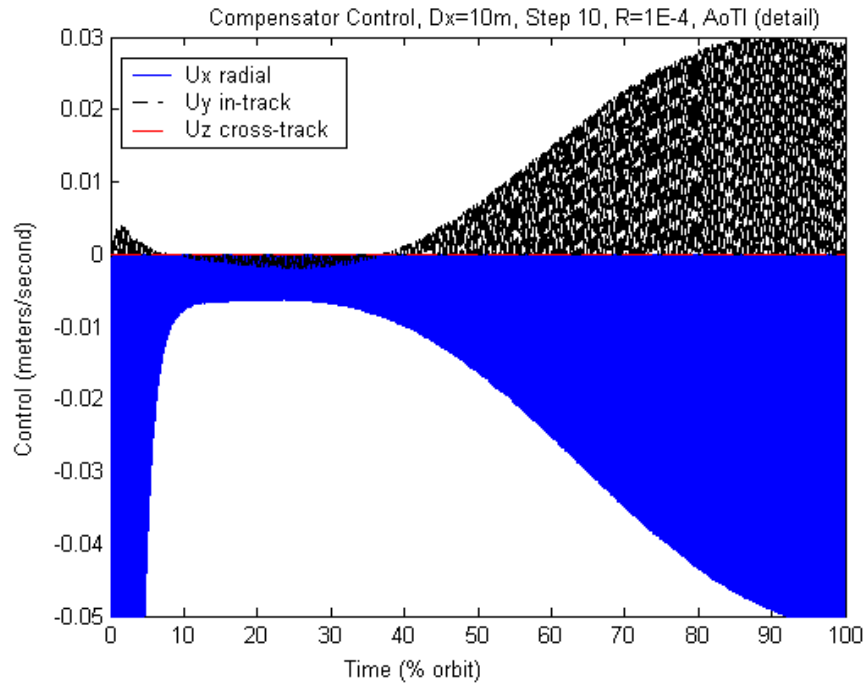

Figure 93. Compensator Control for R=1E-4, Dx=10m, Step 10, AoTI

B.5.4 Model Comparisons.

Table 24. Compensator Total Control Over One Orbit, Dx=10m, Step 10

control (m/sec)	R=1E-6	R=1E-5	R=1E-4	R=1E-3	R=1E-2	R=1E-1	R=1E0
AnTV	0.0476	0.0405	0.0387	0.0421	0.0738	0.210 *	0.173 *
AoTI	0.040 *	0.039 *	0.038 *	0.037 *	0.033 *	0.028 *	0.020 *
AoTV	0.0326	0.0304	0.0310	0.0354	0.0612	0.135 *	0.075 *

* Diverging system

Table 25. Compensator Settling Times, Dx=10m, Step 10

(% orbit)	R=1E-6	R=1E-5	R=1E-4	R=1E-3	R=1E-2	R=1E-1	R=1E0
AnTV	30.05	29.84	29.16	87.47	>100	>100 *	>100 *
AoTI	>100 *	>100 *	>100 *	>100 *	>100 *	>100 *	>100 *
AoTV	41.34	41.18	40.57	38.44	85.74	>100 *	>100 *

* Diverging system

Table 26. Compensator Average RMS Error, Dx=0m, Step 10

(meters)	R=1E-6	R=1E-5	R=1E-4	R=1E-3	R=1E-2	R=1E-1	R=1E0
AnTV	0.0263	0.0263	0.0263	0.0263	0.0263	0.0263	0.0263
AoTI	0.0057	0.0054	0.0057	0.0058	0.0058	0.0060	0.0063
AoTV	0.0975	0.0808	0.0552	0.1098	0.0014	0.00810	0.0008

B.6 Initial Perturbation Dx = 10 m, DGPS noise

The next scenario tested was for the original initial perturbation of 10 meters in the x radial direction, but now the truth model measurement noise was decreased in standard deviation by two orders of magnitude. This was meant to simulate the benefit of using DGPS position data instead of absolute GPS data.

B.6.1 Time-varying Anodal (AnTV).
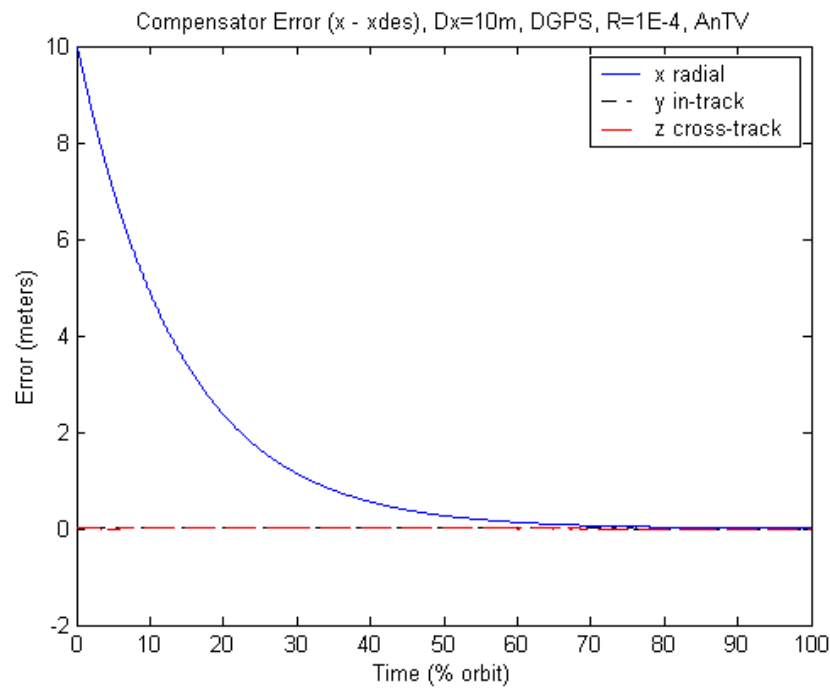

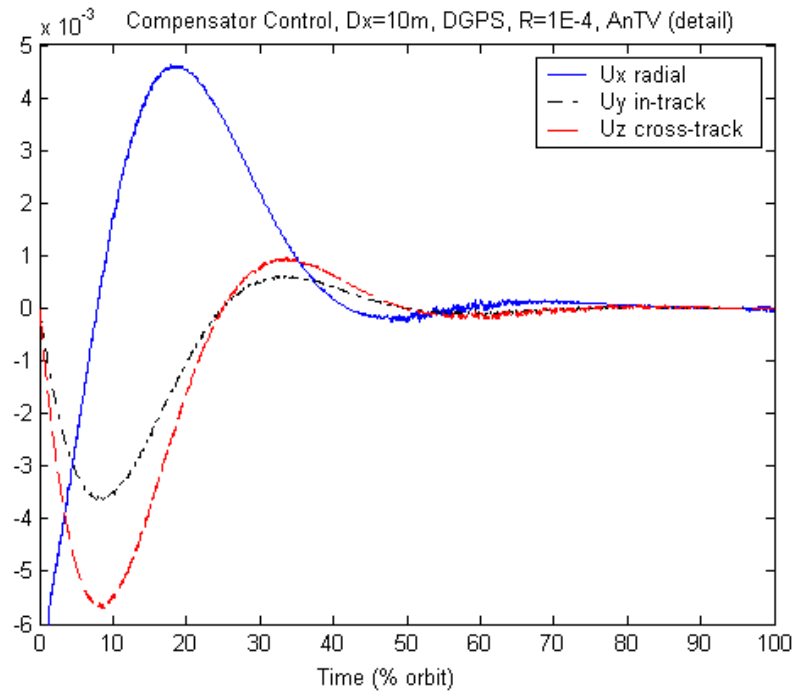Figure 94. Compensator Error for R=1E-4, Dx=10m, DGPS noise, AnTV

Figure 95. Compensator Control for R=1E-4, Dx=10m, DGPS noise, AnTV

B.6.2 Time-varying Anodal (AoTV).

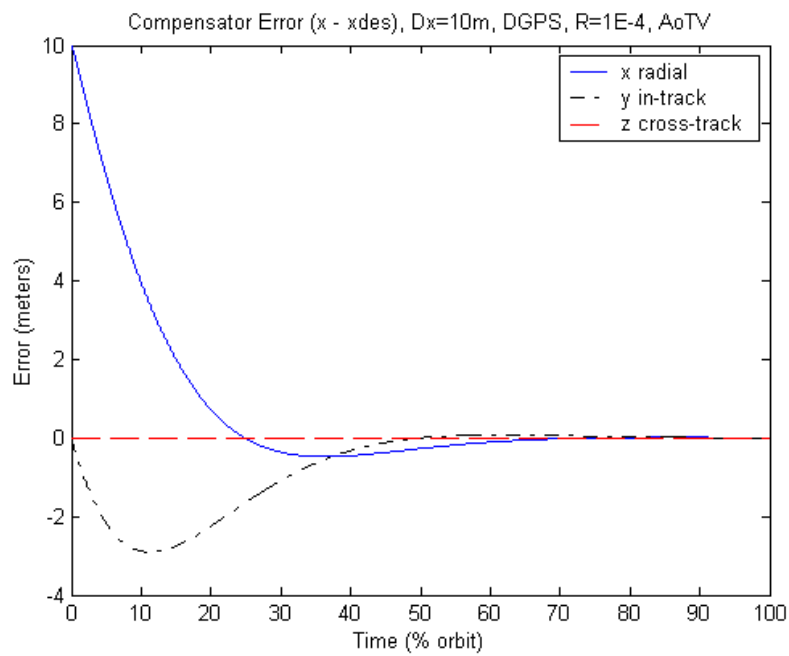
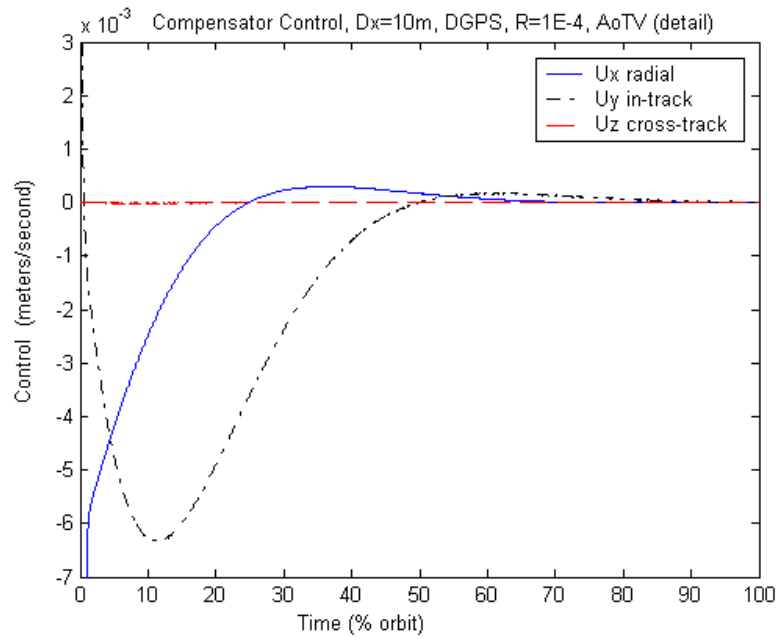Figure 96. Compensator Error for R=1E-4, Dx=10m, DGPS noise, AoTV

Figure 97. Compensator Control for R=1E-4, Dx=10m, DGPS noise, AoTV

B.6.3 Time-invariant Anodal (AoTI).

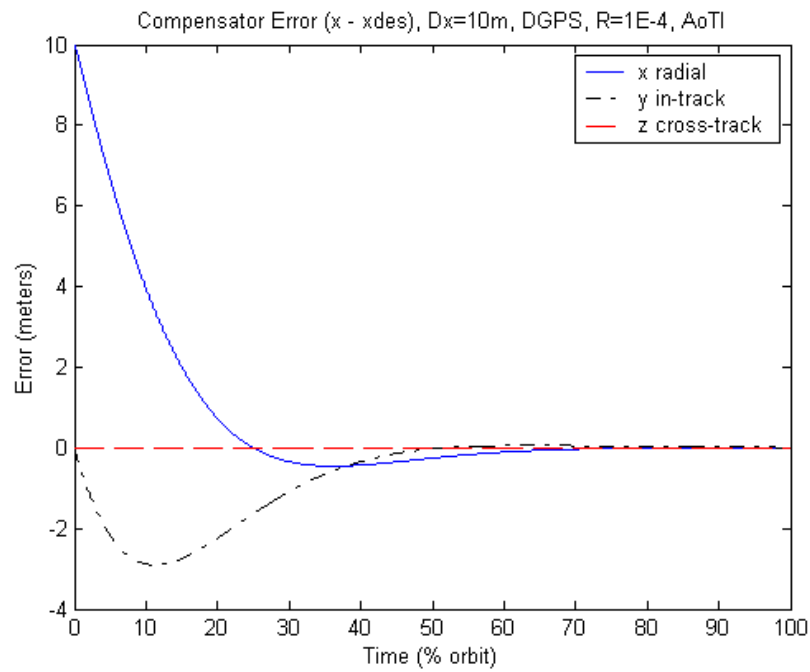

Figure 98. Compensator Error for R=1E-4, Dx=10m, DGPS noise, AoTI
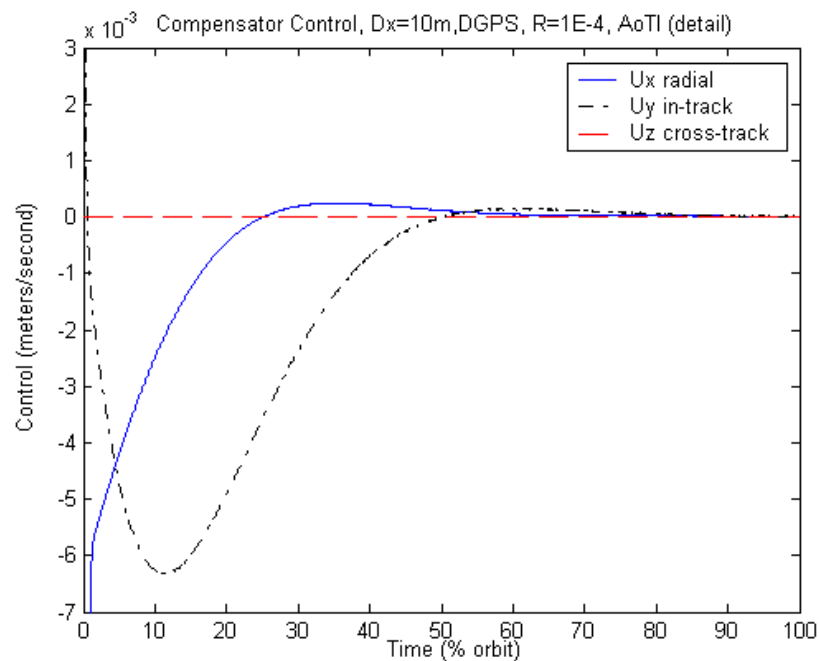
Figure 99. Compensator Control for R=1E-4, Dx=10m, DGPS noise, AoTI

B.6.4 Model Comparisons.

Table 27. Compensator Total Control Over One Orbit, Dx=10m, DGPS noise

Control-m/sec	R=1E-6	R=1E-5	R=1E-4	R=1E-3	R=1E-2	R=1E-1	R=1E0
AnTV	0.0344	0.0331	0.0329	0.0335	0.0356	0.0394	0.0449
AoTI	0.0302	0.0290	0.0288	0.0292	0.0302	0.0315	0.0323
AoTV	0.0304	0.0291	0.0289	0.0293	0.0304	0.0315	0.0323

Table 28. Compensator Settling Times, Dx=10m, DGPS noise

% orbit	R=1E-6	R=1E-5	R=1E-4	R=1E-3	R=1E-2	R=1E-1	R=1E0
AnTV	41.41	41.44	41.53	41.80	42.44	41.91	34.58
AoTI	41.14	41.40	41.26	41.52	42.21	43.30	52.15
AoTV	41.38	41.40	41.50	41.77	42.48	43.54	52.87

108

Table 29. Compensator Average RMS Error, Dx=0m, DGPS noise

(meters)	R=1E-6	R=1E-5	R=1E-4	R=1E-3	R=1E-2	R=1E-1	R=1E0
AnTV	5.3E-4	2.4E-4	3.6E-4	8.3E-4	4.3E-4	3.9E-4	4.3E-4
AoTI	3.3E-4	3.5E-4	2.9E-4	3.5E-4	4.4E-4	5.6E-4	4.6E-4
AoTV	2.5E-4	8.9E-4	1.8E-4	6.5E-4	1.2E-4	2.2E-4	4.7E-4

B.7 Initial Perturbation Dx = 10 m, 100 x noise

The last scenario tested was for the original initial perturbation of 10 meters in the x radial direction, but now the truth model measurement noise was increased in standard deviation by two orders of magnitude. This was meant to simulate the detriment of losing the ability to collect absolute GPS data.

B.7.1 Time-varying Anodal (AnTV).

Figure 100. Compensator Error for R=1E-4, Dx=10m, 100 x noise, AnTV

Figure 101. Compensator Control for R=1E-4, Dx=10m, 100 x noise, AnTV

110

B.7.2 Time-varying Anodal (AoTV).

Figure 102. Compensator Error for R=1E-4, Dx=10m, 100 x noise, AoTV

Figure 103. Compensator Control for R=1E-4, Dx=10m, 100 x noise, AoTV

B.7.3 Time-invariant Anodal (AoTI).

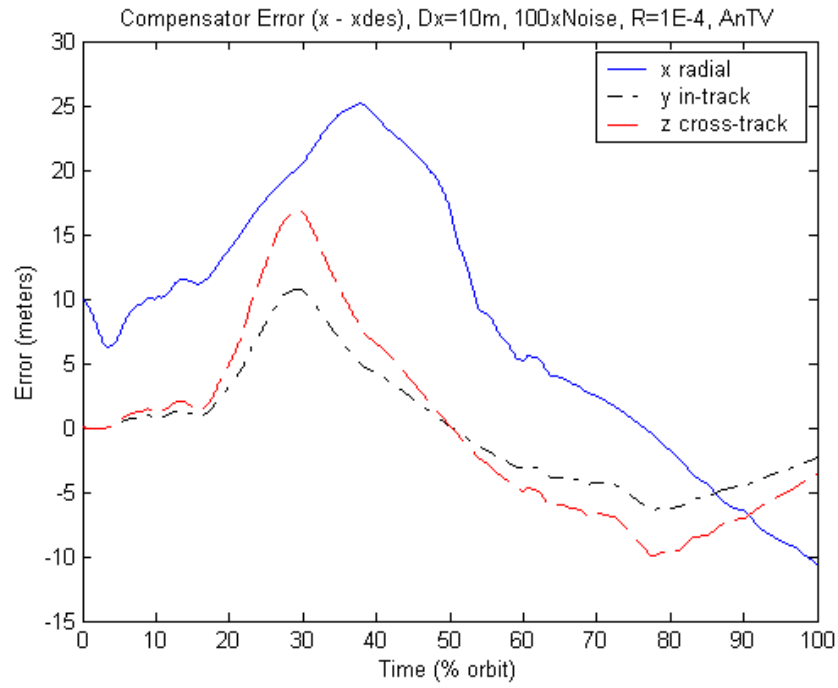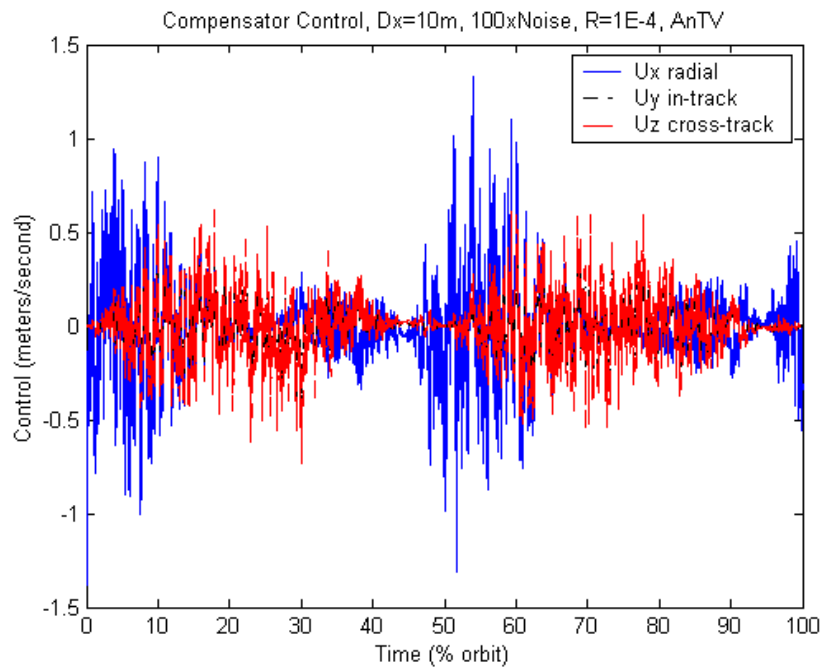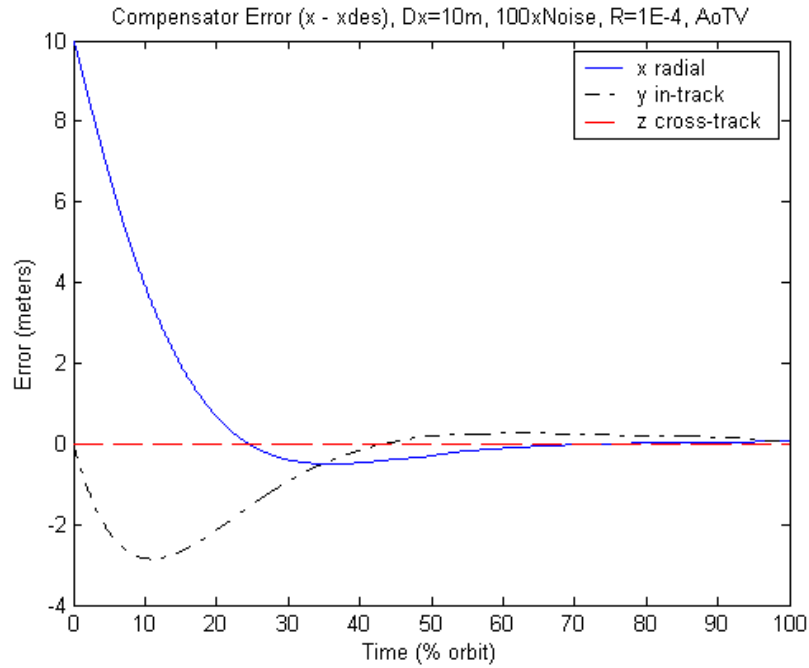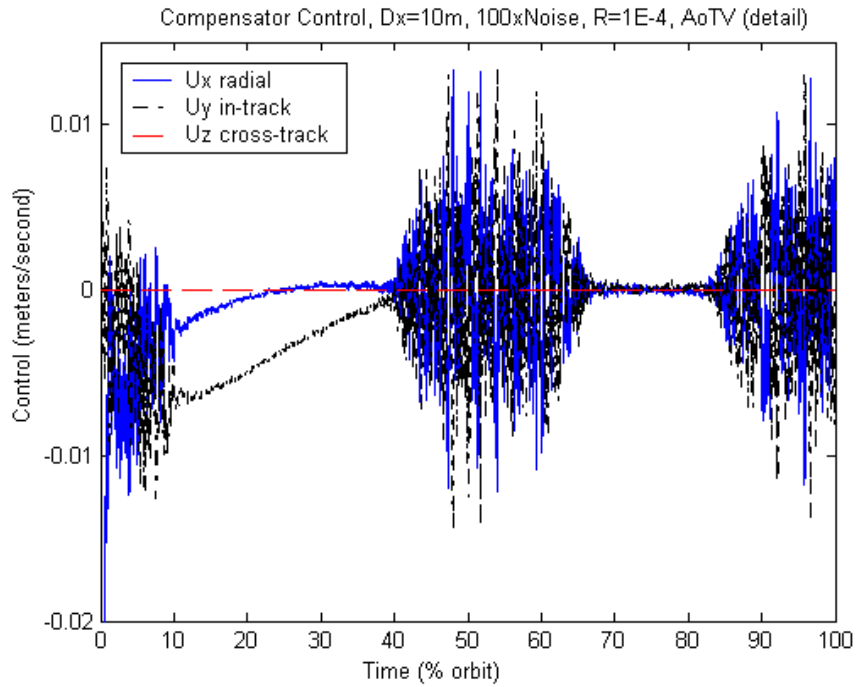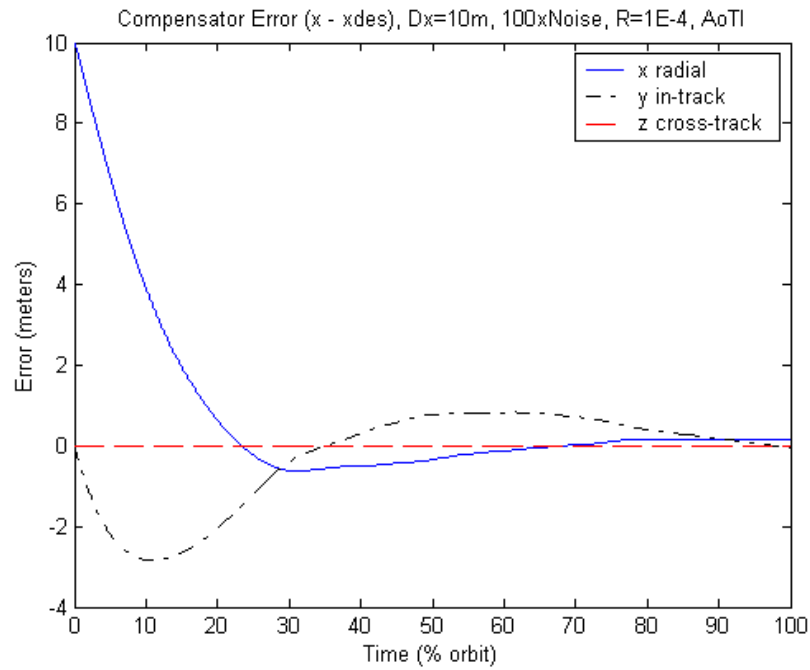Figure 104. Compensator Error for R=1E-4, Dx=10m, 100 x noise, AoTI
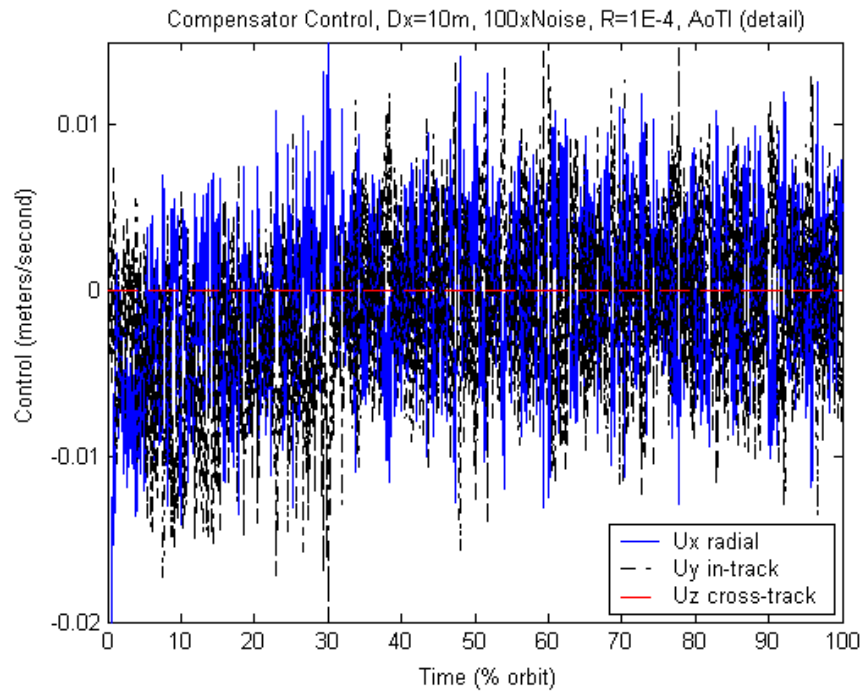

Figure 105. Compensator Control for R=1E-4, Dx=10m, 100 x noise, AoTI

B.7.4 Model Comparisons.

Table 30. Compensator Total Control Over One Orbit, Dx=10m, 100 x Noise

control (m/sec)	R=1E-6	R=1E-5	R=1E-4	R=1E-3	R=1E-2	R=1E-1	R=1E0
AnTV	6.983 *	3.936 *	2.240 *	1.306 *	0.793 *	0.530 *	0.426 *
AoTI	0.1728	0.1038	0.0669	0.0488	0.0399	0.0356	0.0334
AoTV	0.0901	0.0607	0.0455	0.0379	0.0340	0.0331	0.0327

    * Diverging system

Table 31. Compensator Settling Times, Dx=10m, 100 x Noise

(% orbit)	R=1E-6	R=1E-5	R=1E-4	R=1E-3	R=1E-2	R=1E-1	R=1E0
AnTV	>100 *	>100 *	>100 *	>100 *	>100 *	>100 *	>100 *
AoTI	77.26	77.28	77.34	77.56	78.34	81.34	93.96
AoTV	39.74	39.78	39.90	40.28	41.22	42.56	61.44

    * Diverging system

Table 32. Compensator Average RMS Error, Dx=0m, 100 x Noise

(% orbit)	R=1E-6	R=1E-5	R=1E-4	R=1E-3	R=1E-2	R=1E-1	R=1E0
AnTV	1.5859 *	4.2933 *	3.4412 *	4.7513 *	2.5248 *	3.8470 *	2.1767 *
AoTI	0.0737	0.0864	0.1650	0.1162	0.1623	0.2044	0.2268
AoTV	0.1088	0.1798	0.0324	0.1225	0.3212	0.1213	0.0870

    * Diverging system

Bibliography

1. Air Force Research Lab. "TechSat 21 Factsheet and Overview." http://www.vs.afrl.af.mil/Factsheets/techsat21.html, December 2001.

2. Bate, Roger R., Donald D. Mueller, and Jerry E. White. *Fundamentals of Astrodynamics*. New York: Dover Publications, 1971.

3. Bittanti, Sergio, Alan J. Laub, and Jan C. Willems. *The Riccati Equation*. Berlin: Springer-Verlag, 1991.

4. Bordner, Ralph E. *Estimation of Relative Satellite Formation Element Positions In Near Circular Orbits*. MS Thesis, AFIT/GA/ENY/01M-01, School of Engineering, Air Force Institute of Technology (AETC), Wright-Patterson AFB OH, March 2001.

5. Bordner, Ralph E., and William E. Wiesel. "Trajectory Estimation for Satellite Clusters." In preparation for future submission.

6. Brockett, Roger W. *Finite Dimensional Linear Systems*. New York: John Wiley and Sons, Inc.

7. Bryson, Arthur E. *Dynamic Optimization*. Menlo Park, CA: Addison Wesley Longman, Inc., 1999.

8. Cantafio, Leopold J. *Space-Based Radar Handbook*. Norwood, MA: Artech House, Inc., 1989.

9. Davis, Jeffrey S. *Navigation of Satellite Clusters*. MS Thesis, AFIT/GSO/ENY/00M-01, School of Engineering, Air Force Institute of Technology (AETC), Wright-Patterson AFB OH, March 2000.

10. European Space Agency. "Cluster II Homepage." http://sci.esa.int/cluster, December 2001.

11. Irvin, David J. *A Study of Linear Vs. Nonlinear Control Techniques for the Reconfiguration of Satellite Formations*. MS Thesis, AFIT/GA/ENY/01M-02, School of Engineering, Air Force Institute of Technology (AETC), Wright-Patterson AFB OH, March 2001.

12. Hughes, Mel and Scott Norris. "An Overview of the Technology Satellite of the 21st Century (TechSat 21) Program." July 2001.

13. Jacques, David R. Class Handouts from Modern Controls Class SENG 765. Graduate School of Engineering, Air Force Institute of Technology (AETC), Wright-Patterson AFB OH, September 2001.

14. Johnston, Stephen C. *Autonomous Navigation of a Satellite Cluster*. MS Thesis, AFIT/GA/ENY/90D-9, School of Engineering, Air Force Institute of Technology (AETC), Wright-Patterson AFB OH, December 1990 (AD-A1103970).

15. Kwakernaak, Huibert and Raphael Sivan. *Linear Optimal Control Systems*. New York: Wiley-Interscience, 1972.

16. Larson, Wiley J. and James Wertz. *Space Mission Analysis and Design*. Torrence, California: Microcosm, Inc. and Kluwer Academic Publishers, 1992.

17. Maciejowski, Jan M. *Multivariable Feedback Design*. Wokingham, England: Addison-Wesley, 1989.

18. Martin, Maurice. "TechSat 21 and Revolutionizing Space Missions Using Microsatellites." American Institute of Aeronautics and Astronautics, 2001.

19. Middendorf, J. T. *Navigation of a Satellite Cluster with Realistic Dynamics*. MS Thesis, AFIT/GA/ENY/91D-5, School of Engineering, Air Force Institute of Technology (AETC), Wright-Patterson AFB OH, December 1991.

20. National Aeronautics and Space Administration. "Starlight Homepage." http://starlight.jpl.nasa.gov, August 2001.

21. Sedwick, R. J. and others. "Mitigation of Differential Perturbations in Clusters of Formation Flying Satellites." *Advances in Astro Sciences,* 102:323-342(1999).

22. Stengel, Robert F. *Stochastic Optimal Control, Theory and Applications*. New York: John Wiley and Sons, 1986.

23. U.S. Air Force News Release. "Birds Inspire Formation-flying Satellites." July 2000.

24. Ward, Michael L. *Estimated Satellite Cluster Elements in Near Circular Orbit*. MS Thesis, AFIT/GA/AA/88D-13, School of Engineering, Air Force Institute of Technology (AETC), Wright-Patterson AFB OH, December 1988 (AD-A1103970).

25. Wiesel, William E. *Spaceflight Dynamics*. Boston: McGraw-Hill, 1989.

26. Wiesel, William E. Class Handouts from Modern Methods of Orbit Determination Class, MECH 636. Graduate School of Engineering, Air Force Institute of Technology (AETC), Wright-Patterson AFB OH, March 1998.

27. Wiesel, William E. "Perturbations of Relative Satellite Motion about an Oblate Planet." Submitted to *Journal of Guidance and Control*, June 2000.

28. Wiesel, William E. "Relative Satellite Motion about an Oblate Planet." Submitted to *Journal of Guidance and Control*, January 2000.

29. Zhou, Kemin and John C. Doyle. *Essentials of Robust Control*. Upper Saddle River, New Jersey: Prentice Hall, 1998.

Vita

Captain Erin Y. Carraher was born in Vermillion, South Dakota. He attended Coral Springs High School in Florida, graduating in June 1988. After high school, Captain Carraher attended the Georgia Institute of Technology in the fall of 1988. He graduated with high honors and earned a Bachelor's degree in Aerospace Engineering. He received his commission to second lieutenant in September of 1992.

Shortly thereafter, Captain Carraher received his first assignment as an Operations Support Engineer and then Satellite Systems Integration Engineer at Falcon AFB, Colorado. In January 1995 Captain Carraher was assigned to the 2nd Space Launch Squadron, Vandenberg AFB, California as Chief of Small Launch Vehicle Operations and Booster Flight Commander. He was promoted to the rank of captain in December 1997. In June 1998, Captain Carraher arrived at Yokota Air Base, Japan. He joined the 315th Intelligence Squadron Operations Directorate where he has served as Chief of Open Source Exploitation, Chief of Foreign Materiel Exploitation, and Operations Officer. Captain Carraher graduated from Squadron Officer's School at Maxwell AFB, Alabama in August 2000. He was subsequently assigned to study Astronautical Engineering at the Air Force Institute of Technology at Wright Patterson AFB, Ohio. Upon graduation, he will be assigned to the Space Warfare Center at Schriever AFB, Colorado.

1. REPORT DATE (DD-MM-YYYY) 26-03-2002	2. REPORT TYPE **Master's Thesis**	3. DATES COVERED (From – To) Aug 2000 – Mar 2002

4. TITLE AND SUBTITLE	5a. CONTRACT NUMBER
PERIODIC METHODS FOR CONTROLLING A SATELLITE IN FORMATION	5b. GRANT NUMBER
	5c. PROGRAM ELEMENT NUMBER
6. AUTHOR(S) Carraher, Erin, Y., Captain, USAF	5d. PROJECT NUMBER
	5e. TASK NUMBER
	5f. WORK UNIT NUMBER

7. PERFORMING ORGANIZATION NAMES(S) AND ADDRESS(S) Air Force Institute of Technology Graduate School of Engineering and Management (AFIT/EN) 2950 P Street, Building 640 WPAFB OH 45433-7765	8. PERFORMING ORGANIZATION REPORT NUMBER AFIT/GA/ENY/02-1
9. SPONSORING/MONITORING AGENCY NAME(S) AND ADDRESS(ES) AFRL/VACA Attn: Dr. Andrew Sparks 2130 8th Street WPAFB OH 45433	10. SPONSOR/MONITOR'S ACRONYM(S)
	11. SPONSOR/MONITOR'S REPORT NUMBER(S)

12. DISTRIBUTION/AVAILABILITY STATEMENT

APPROVED FOR PUBLIC RELEASE; DISTRIBUTION UNLIMITED.

13. SUPPLEMENTARY NOTES

14. ABSTRACT

Precise position determination and control is necessary to accomplish proposed satellite formation flying missions of ground movement target indication and synthetic aperture radar. This thesis combines the estimation and control techniques of past AFIT theses with various time-varying and time-invariant LQG control methods. Linear time-invariant control is ideal for on-board satellite estimation and control applications, freeing-up the satellite's limited computational capacity. Using a dynamics frame transformation from the nodal frame to an orbital frame, a higher fidelity, time-periodic model produced nearly identical results for either time-varying or time-invariant control for many scenarios. Scenarios included initial perturbations in the radial, in-track, and cross-track directions as well as increased magnitude perturbations; step size increase from 0.2 seconds to 2 seconds; and increased and reduced measurement noise level scenarios versus the standard absolute GPS receiver noise level. Results obtained indicate the ability to control within the error range of the measurements (centimeter-level and better) using realistic noise and dynamics perturbations

15. SUBJECT TERMS
Satellite Clusters, Estimation, LQR, Time Periodic, LTI, Satellite Formation Flying

16. SECURITY CLASSIFICATION OF:			17. LIMITATION OF ABSTRACT	18. NUMBER OF PAGES	19a. NAME OF RESPONSIBLE PERSON David R. Jacques, Lt Col, USAF (ENY)
a. REPORT	b. ABSTRACT	c. THIS PAGE	UU	133	19b. TELEPHONE NUMBER (Include area code) (937) 255-6565, ext 4723; e-mail: David.Jacques@afit.edu
U	U	U			

Standard Form 298 (Rev. 8-98)
Prescribed by ANSI Std. Z39-18